

## 5 RESEARCH ACTIVITIES

### 5.1 NUCLEAR PHYSICS

S. Muralithar, N. Madhavan and P. Sugathan

The experiments done earlier by users, resulted in thirteen publications in international journals 2020 – 2021, from gamma array facilities. In these publications the studies focussed on the following phenomena: antimagnetic rotational motion, multiphonon longitudinal wobbling, evolution of collectivity and shape transition, complex nuclear excitations, metastable states from multinucleon excitations, spectroscopic study above isomer, lifetime measurements, gamma-vibration, incomplete fusion dynamics, and structure of positive parity states. The typical nuclear structure and reaction studies undertaken and reported in this section are : How quadrupole moment changes with spin - by Himachal Pradesh University group; Coulomb excitation study of  $^{118}\text{Sn}$  and shell model calculations of excitation energy with spin in  $^{84,86,88}\text{Sr}$  nuclei using BIGSTICK code by a scholar of IUAC; what are target deformation effects on fusion and incomplete fusion and angular distribution of evaporation residues populated through complete and incomplete fusion by Central University, Jharkhand; Chirality in  $^{128}\text{La}$  using lifetime measurements by IITB group; GEANT4 simulations for crosstalk estimation for CPDA by GNDU group; Forward recoil range distribution measurement for the system  $^{14}\text{N} + ^{169}\text{Tm}$  by a scholar of IUAC and study of octupole deformation in neutron deficient nuclei ( $A < 120$ ) through lifetime measurements by Delhi University group.

HIRA recoil mass spectrometer facility was used in six experimental runs for the measurements of Evaporation Residue (ER) cross sections and/or transfer reaction and quasi-elastic back-scattering cross sections in order to extract fusion barrier distributions and/or to understand the effect of positive Q-value transfer channels, neutron shell closure in target, target deformation, entrance channel effect, etc. on the sub-barrier fusion reaction process. Transfer reactions were studied either using the coincidence method or by detecting only the target-like recoil products, in the singles mode involving asymmetric reactions, at  $0^\circ$  due to the excellent primary beam rejection of HIRA. All these studies were part of thesis work of research scholars from various universities in the country. Research work carried out by four research scholars using HIRA or HYRA facility in the previous year(s) were published and also culminated in their obtaining doctorate degrees. The role of positive Q-value transfer channels (up to six nucleon transfer) was distinctively evident in the sub-barrier fusion cross section enhancement in  $^{35}\text{Cl} + ^{130}\text{Te}$  compared with that in  $^{37}\text{Cl} + ^{130}\text{Te}$  system which has all negative Q-value neutron transfer channels. Simulation studies were carried out for the extraction of transmission efficiency of RMS, such as HIRA, in the detection of target-like transfer products which was published.

User experiments on mass gated neutron multiplicities, fission fragment mass distribution and quasi-elastic studies were performed using time of flight (TOF) setup in NAND and GPSC facilities. Neutrons were detected by liquid scintillator array in coincidence with fission fragments detected in a pair of multi-wire proportional counters (MWPC). For measurement of quasi-elastic process at near barrier energies, multi-detector setup consisting of TOF and particle identification detectors were setup and used in kinematic coincidence condition. Characteristics and performance results of the NAND detectors has been published in a recent paper highlighting the features and performance of all major sub-components and a comparison of array for high precision measurements in heavy and super heavy mass regions. Results from one of the recent experiment at LINAC beam energies performed in NAND facility showed the significance of the entrance channel formation time influencing the measured neutron multiplicities. Analysis of other measurements investigating the nature of dissipation, shell effects and deformation on neutron multiplicities from fission of heavy and super heavy nuclei are in early stage and preliminary results are reported in this report. Detailed investigation of NAND detector performance for higher energy neutrons emitted in pre-equilibrium emission reactions have also been investigated by optimizing the operating parameters of the detectors and electronics for large dynamic range covering up to 25 MeV neutrons.

### 5.1.1 Measurement of quasi-elastic excitation function for $^{16}\text{O}+^{142}\text{Ce}$ using a Recoil Mass Spectrometer

Rohan Biswas<sup>1</sup>, S. Nath<sup>1</sup>, J. Gehlot<sup>1</sup>, Gonika<sup>1</sup>, Chandra Kumar<sup>1</sup>, A. Parihari<sup>1</sup>, N. Madhavan<sup>1</sup>, Phurba Sherpa<sup>2</sup> and Shoaib Noor<sup>3</sup>

<sup>1</sup>Nuclear Physics Group, Inter-University Accelerator Centre, Aruna Asaf Ali Marg, New Delhi 110067, India

<sup>2</sup>Department of Physics and Astrophysics, Delhi University, Delhi 110007, India

<sup>3</sup>School of Physics and Materials Science, Thapar Institute of Engineering and Technology, Patiala 147004, India

A Recoil Mass Spectrometer (RMS), like the Heavy Ion Reaction Analyzer (HIRA) [1], is primarily used for measuring fusion excitation functions of heavy ion-induced reactions. The barrier distribution, extracted from the excitation function, reveals the structure of the interacting nuclei that influences fusion dynamics. The barrier distribution can also be extracted from the excitation function of quasi-elastic scattering [2], measured in the backward angles in the laboratory frame of reference. An attempt was made to measure the quasi-elastic excitation function in a novel application of the RMS. A pulsed beam of  $^{16}\text{O}$  ions, with a pulse separation of  $4\mu\text{s}$ , accelerated through the 15UD Pelletron accelerator at IUAC was bombarded on  $^{142}\text{Ce}$  target. The isotopically enriched target foils (of thickness  $120\mu\text{g}/\text{cm}^2$ ), sandwiched between two layers of graphite films used as the backing (of thickness  $20\mu\text{g}/\text{cm}^2$ ) and capping (of thickness  $5\mu\text{g}/\text{cm}^2$ ) were fabricated at the Target Development Laboratory of IUAC [3]. Beam energy was varied between 52 and 76 MeV. Two solid state silicon detectors (SSSD) were kept at an angle of  $150^\circ$  on either side of the beam direction in the horizontal plane and used for beam monitoring during the experiment and for normalisation while calculating the cross-sections. Another SSSD was placed at an angle of  $150^\circ$  with respect to the beam direction to record scattered projectile-like ions. A thin foil of natC was placed 10 cm downstream from the target to reset charge states of the reaction products to equilibrium distribution. The HIRA was operated at  $0^\circ$  with an opening aperture of 5 msr. Both Evaporation Residues (ERs) and Target-like Recoils (TRs) were detected by a Multi-Wire Proportional Counter (MWPC) of dimensions 150 mm in x-direction and 50 mm in y-direction (z-axis being the direction of beam), placed at the focal plane of the HIRA. The cathode signal from the MWPC gave the energy loss ( $\Delta E$ ) information. Two Time-to-Amplitude Converters (TACs) were setup between the anode signal of MWPC (start) and the radio frequency pulse (stop) to measure time of flight of both ERs and TRs through the RMS.

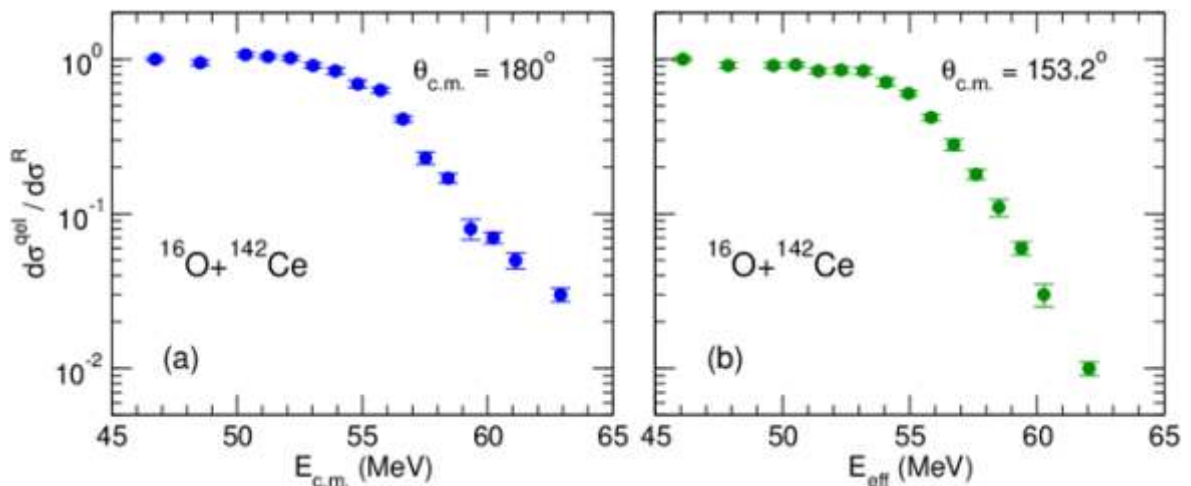


Fig. 5.1.1.1: Quasi-elastic excitation function for  $^{16}\text{O}+^{142}\text{Ce}$  extracted from measurement of (a) target-like ions at  $0^\circ$  and (b) projectile-like ions at  $150^\circ$ .

Quasi-elastic scattering includes elastic, inelastic and transfer channels. For every back-scattered projectile-like ion resulting from quasi-elastic scattering, a corresponding target-like ion recoils in the forward angle in the laboratory frame of reference. Counts of target-like events from the focal plane detector were used to extract the absolute differential quasi-elastic scattering cross-section following the method described in Ref. [4,5]. Fig. 5.1.1.1(a) shows the ratio of differential quasi-elastic cross-section to differential Rutherford scattering cross-section at  $\theta_{\text{c.m.}} = 180^\circ$  as a function of energy available in the centre of mass (c.m.) frame of reference. Fig. 5.1.1.1(b) shows the ratio of differential quasi-elastic cross-section to differential Rutherford scattering cross-section at  $\theta_{\text{c.m.}} = 153.2^\circ$  as a function of the effective energy,  $E_{\text{eff}} \left( = \frac{2E_{\text{c.m.}}}{1 + \csc^2 \frac{\theta_{\text{c.m.}}}{2}} \right)$ . Here, the quasi

elastic events in the energy spectrum were identified according to their energies determined by two-body kinematics. The cross-sections were calculated following the method described in Ref. [6].

Analysis of data for fusion excitation function and coupled-channels calculation are underway.

## REFERENCES:

- [1] A. K. Sinha, N. Madhavan, J. J. Das, P. Sugathan *et al.*, Nucl. Instrum. Methods A **339**, 543 (1994).
- [2] H. Timmers, J. R. Leigh, M. Dasgupta, D. J. Hinde *et al.*, Nucl. Phys. A **584**, 190 (1995).
- [3] Rohan Biswas, Abhilash S.R., Himanshi Gupta, G.R. Umapathy *et al.*, Vacuum **188**, 110159 (2021).
- [4] Rohan Biswas, Sunil Kalkal and S. Nath, Eur. Phys. J. A **57**, 9 (2021).
- [5] Rohan Biswas and S. Nath, Eur. Phys. J. A **56**, 1 (2020).
- [6] Saumyajit Biswas, A. Chakraborty, A. Jhingan, D. Arora *et al.*, Phys. Rev. C **102**, 014613 (2020).

## 5.1.2 Spectroscopy of $^{183}\text{Ir}$

A. Sharma<sup>1</sup>, Shashi. K. Dhiman<sup>1</sup>, Pankaj Kumar<sup>1</sup>, S. Muralithar<sup>2</sup>, R. P. Singh<sup>2</sup>, Yashraj<sup>2</sup>, K. Katre<sup>2</sup>, R. K. Gurjar<sup>2</sup>, Kusum Rani<sup>2</sup>, R. Kumar<sup>2</sup>, S. S. Tiwary<sup>3</sup>, Neelam<sup>4</sup>, Anuj<sup>4</sup>, S. Kumar<sup>4</sup>, Saket Suman<sup>5</sup>, S. K. Tandel<sup>6</sup>, R. Raut<sup>6</sup>, Sutanu Bhattacharya<sup>7</sup>, Umakant Lamani<sup>8</sup> and Subodh<sup>9</sup>

<sup>1</sup>Department of Physics, Himachal Pradesh University, Shimla 171005, India

<sup>2</sup>Inter-University Accelerator Centre, Aruna Asaf Ali Marg, New Delhi 110067, India

<sup>3</sup>Department of Physics, Institute of Science, Banaras Hindu University, Varanasi 221005, India

<sup>4</sup>Department of Physics and Astrophysics, University of Delhi, Delhi 110007, India

<sup>5</sup>UM-DAE Centre for Excellence in Basic Sciences, Mumbai 400098, India

<sup>6</sup>UGC-DAE Consortium for Scientific Research, Kolkata Centre, Kolkata 700098, India

<sup>7</sup>Department of Pure and Applied Physics, Guru Ghasidas Viswavidyalaya, Koni, Bilaspur 495009, India

<sup>8</sup>Department of Physics, Indian Institute of Technology Bombay, Powai, Mumbai 400076, India

<sup>9</sup>Department of Physics, Panjab University, Chandigarh 160014, India

Gamma spectroscopic studies of rapidly rotating atomic nuclei have revealed useful information on excited states in nuclei. Nuclear states with large deformations, which are thought to be generated due to the shape-driving high- $j$  orbitals from higher lying shells, are known as "intruder" states. Hence, high- $j$  intruder orbitals play a key role in the evolution of different shapes at higher angular momentum. The iridium isotopes lie in the region of transition between deformed and spherical nuclei. Nuclei in this region are soft with respect to the gamma deformation and hence several structural phenomena associated with triaxial shapes are observed [1]. The structure of odd- $A$  Ir isotopes can be interpreted in terms of an odd proton coupled with the even-even Os core [2]. The deformation of the rotational bands in Ir nuclei gets enhanced after back-bending [3]. Apart from the observation of deformed rotational bands, several high- $K$  multi-quasiparticle states with different shapes are also observed in these nuclei [1]. Experimental information on excited states in  $^{183}\text{Ir}$  is very scanty and demand further investigations [4, 5]. This report provides a summary of our recent experimental study on  $^{183}\text{Ir}$  which was carried out to study the structure of the high spin states through lifetime measurement.

An experiment was performed to populate the excited states of  $^{183}\text{Ir}$  via  $^{169}\text{Tm}(^{18}\text{O}, 4n)$  fusion evaporation reaction at beam energy 94 MeV, delivered by the 15UD Pelletron at IUAC. Thickness of  $^{169}\text{Tm}$  target was 6.5 mg/cm<sup>2</sup>. The de-excited gamma rays were detected by the Indian National Gamma Array (INGA) [6] consisting of sixteen Compton suppressed Clover detectors and 2 low-energy photon spectrometer (LEPS) detectors. The Clover detectors were mounted at 5 different angles with respect to the beam axis, viz, three at 32°, one at 57°, six at 90°, two at 123° and four at 148°. The data were collected using the CAMAC based analogue data acquisition system CANDLE [7]. A number of symmetric and asymmetric matrices were constructed by sorting of gain-matched list-mode data. Offline analysis of data was carried out by using INGASORT [8] and RADWARE [9] computer codes. A total of about  $3 \times 10^7$  events were recorded. The strongly populated  $\pi h_{9/2}$  band

was observed up to  $\sim 6.1$  MeV. Total projection spectrum and Doppler-shifted spectrum for some yrast band transitions are shown in Fig. 5.1.2.1 and 5.1.2.2, respectively. Further analysis of data is in progress

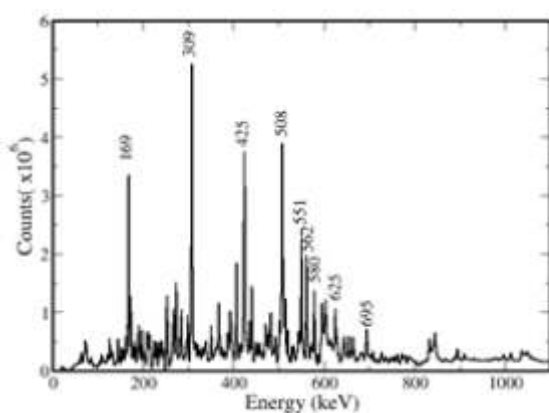


Fig. 5.1.2.1:  $\gamma$ - $\gamma$  coincidence spectrum from the reaction  $^{169}\text{Tm}(^{18}\text{O}, 4n)$ .

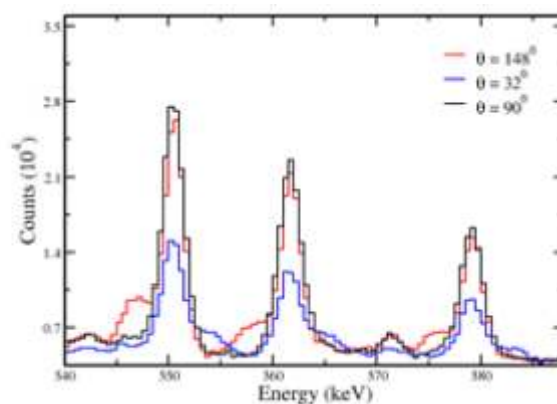


Fig. 5.1.2.2: Doppler-shifted  $\gamma$ -spectrum observed in different angles for the yrast band transitions of  $^{183}\text{Ir}$ .

#### REFERENCES:

- [1] V. Modamio *et al.*, Phys. Rev. C **81**, 054304 (2010).
- [2] R. Kaczarowski *et al.*, Phys. Rev. C **41**, 2069 (1990).
- [3] S. Andre *et al.*, Phys. Rev. Lett. **38**, 327 (1977).
- [4] V. P. Janzen *et al.*, Phys. Rev. Lett. **61**, 2073 (1988).
- [5] A. J. Kreiner *et al.*, Phys. Rev. C **42**, 878 (1990).
- [6] S. Muralithar *et al.*, Nucl. Instr. Meth. A **622**, 281 (2010).
- [7] Ajith Kumar B. P. *et al.*, Proc. DAE-BRNS Symp. Nucl. Phys. B **44**, 390 (2001).
- [8] R. K. Bhowmik *et al.*, Proc. DAE-BRNS Symp. Nucl. Phys. B **44**, 422 (2001).
- [9] D. C. Radford *et al.*, Nucl. Instr. Meth. A **361**, 267 (1995).

### 5.1.3 Shell model calculations of $^{84,86,88}\text{Sr}$ nuclei using BIGSTICK code

I. Ahmed<sup>1</sup>, S. Dutt<sup>2</sup>, C. Qi<sup>3</sup> and R. Kumar<sup>1</sup>

<sup>1</sup>Nuclear Physics Group, Inter-University Accelerator Centre, New Delhi 110067, India

<sup>2</sup>Department of Physics, Aligarh Muslim University, Aligarh 202002, India

<sup>3</sup>KTH, Royal Institute of Technology, Stockholm, SE 10691, Sweden

In the nuclear chart, other than deformed rotors and spherical vibrators, transitional region plays an important role, and has become a very useful paradigm to explain the structure of the nuclei evolving from one of the limiting cases to another as a function of the neutron/proton number. In particular, the transitional Sr isotopes are quite interesting and are mapped by sudden shape transitions within the isotopic chain.

A possible subshell closure at  $Z=38$ , invokes a special interest in Sr-isotopes. Single-particle picture is generally expected as  $N$  approaches 50 and an increase in collective effects is expected while moving away from  $N=50$ . The relatively smaller  $B(E2; 2_1^+ \rightarrow 0_1^+)$  values in Sr-isotopes near  $N=50$  also suggest such kind of a picture. The region around  $Z\sim 40$  and  $N\sim 45$  is a transitional region lying between the spherical and deformed shapes. Likewise,  $^{88}\text{Sr}$  is said to be a doubly magic nucleus having  $Z=38$ , proton subshell closure and  $N=50$ , a closed neutron shell, with a spherical ground state band. Rapid transition to a deformed structure in ground state, has been predicted for neutron-deficient Sr-isotopes  $^{76,78}\text{Sr}$ .  $^{84}\text{Sr}$  is expected to display both collective and quasi-particle excitations being just four neutron-holes away from  $^{88}\text{Sr}$  [1].

In the present study, the shell structures of  $^{84-88}\text{Sr}$  isotopes were studied by performing the large-scale shell model (LSSM) calculations using the BIGSTICK [2] code. A single particle model space defined by  $0f_{5/2}$ ,  $1p_{3/2}$ ,  $1p_{1/2}$  and  $0g_{9/2}$  orbitals was chosen for the calculations considering  $^{58}\text{Ni}$  as the core. The calculations were performed using the Hamiltonian matrix elements with the recent effective interaction of Honma *et al.* [3], consisting of 133 two-body matrix elements, along with the 4 single-particle states.

The code uses the Lanczos algorithm [4] to reduce the Hamiltonian matrix to a truncated tri-diagonal matrix, whose eigen values approximate the extremal eigen values of the full matrix. The code also provides an option

of scaling and auto scaling with respect to some known nuclei to generate the excitation energy spectrum. The standard procedure of diagonalization called Lanczos with default convergence was used for all the three nuclei. The criterion for energy convergence was such that, energy should be minimised to less than 0.0010 MeV.

These calculations were performed at the FUJITSU workstation of IUAC which consists of an Intel Xeon processor with a RAM of 64GB and a clock speed ~2.40 GHz. This machine has 10 cores with 02 threads each (i.e. effective cores = 20) along with a general storage of 1TB.

The calculated results for excitation energy are shown in the following Table and are compared with the previous experimental results [5]. As is clear from the table, there is a reasonable agreement between the two columns of excitation energies for  $^{84,86,88}\text{Sr}$  isotopes. Calculations for electromagnetic transitions are yet to be performed using the density matrices generated by this code.

**Table 5.1.3: Low-lying energy spectrum for  $^{84,86,88}\text{Sr}$ -isotopes.**

Nuclei	$J^\pi$	Ex. (exp.) (MeV)	Ex. (this work/SM) (MeV)
$^{84}\text{Sr}$	$2_1^+$	0.793	0.849
	$2_2^+$	1.454	1.840
	$4_1^+$	1.768	1.924
$^{86}\text{Sr}$	$2_1^+$	1.077	1.177
	$2_2^+$	1.854	2.000
	$4_1^+$	2.230	2.464
$^{88}\text{Sr}$	$2_1^+$	1.836	1.830

#### REFERENCES:

- [1] A. Dewald, U. Kaup, W. Gast, A. Gelberg, H.-W. Schuh, K. O. Zell and P. von Brentano, Phys. Rev. C **25**, 226 (1982).
- [2] C. W. Johnson, W. E. Ormand, K. S. McElvain and H. Shan, UCRL number LLNL-SM-739926, arXiv:1801.08432.
- [3] M. Honma, T. Otsuka, T. Mizusaki and M. Hjorth-Jensen, Phys. Rev. C **80**, 064323 (2009).
- [4] R. R. Whitehead, A. Watt, B. J. Cole and I. Morrison, Advances in Nuclear Physics **9**, 123 (1977).
- [5] www.nndc.bnl.gov

### 5.1.4 Study of target deformation effect on fusion dynamics with Universal Fusion Function

Pankaj K. Giri<sup>1</sup>, D. Singh<sup>1</sup>, Amritraj Mahato<sup>1</sup>, Sneha B. Linda<sup>1</sup>, Harish Kumar<sup>2</sup>, Suhail A. Tali<sup>2</sup>, Siddharth Parasari<sup>2</sup>, Asif Ali<sup>2</sup>, M. Afzal Ansari<sup>2</sup>, Rakesh Dubey<sup>3</sup>, R. Kumar<sup>3</sup>, S. Muralithar<sup>3</sup> and R. P. Singh<sup>3</sup>

<sup>1</sup>Department of Physics, Central University of Jharkhand, Ranchi 835222, India

<sup>2</sup>Department of Physics, Aligarh Muslim University, Aligarh 202002, India

<sup>3</sup>Nuclear Physics Group, Inter-University Accelerator Centre, New Delhi 110067, India

The effects of entrance channel parameters on incomplete fusion (ICF) dynamics for systems involving tightly bound projectiles was studied using the universal fusion function (UFF) in Ref. [1]. The experimental fusion functions (EFFs) for the present system i.e.  $^{16}\text{O}+^{148}\text{Nd}$  [2] along with other systems, namely  $^{13}\text{C}+^{159}\text{Tb}$  [3],  $^{13}\text{C}+^{175}\text{Lu}$  [4],  $^{12}\text{C}+^{175}\text{Lu}$  [4],  $^{12}\text{C}+^{159}\text{Tb}$  [5],  $^{16}\text{O}+^{124}\text{Sn}$  [6] and  $^{16}\text{O}+^{181}\text{Ta}$  [7] have been plotted as a function of  $\chi \left( = \frac{E_{c.m.} - V_B}{\hbar\omega} \right)$  (here the symbols have their usual meanings) and are displayed in Fig. 5.1.4.1. The EFFs were determined using total complete-fusion cross sections ( $\sum \sigma_{\text{CF}}$ ) for the systems mentioned above. The solid lines in these figures represent the UFF, which was calculated using the prescription in Ref. [1].

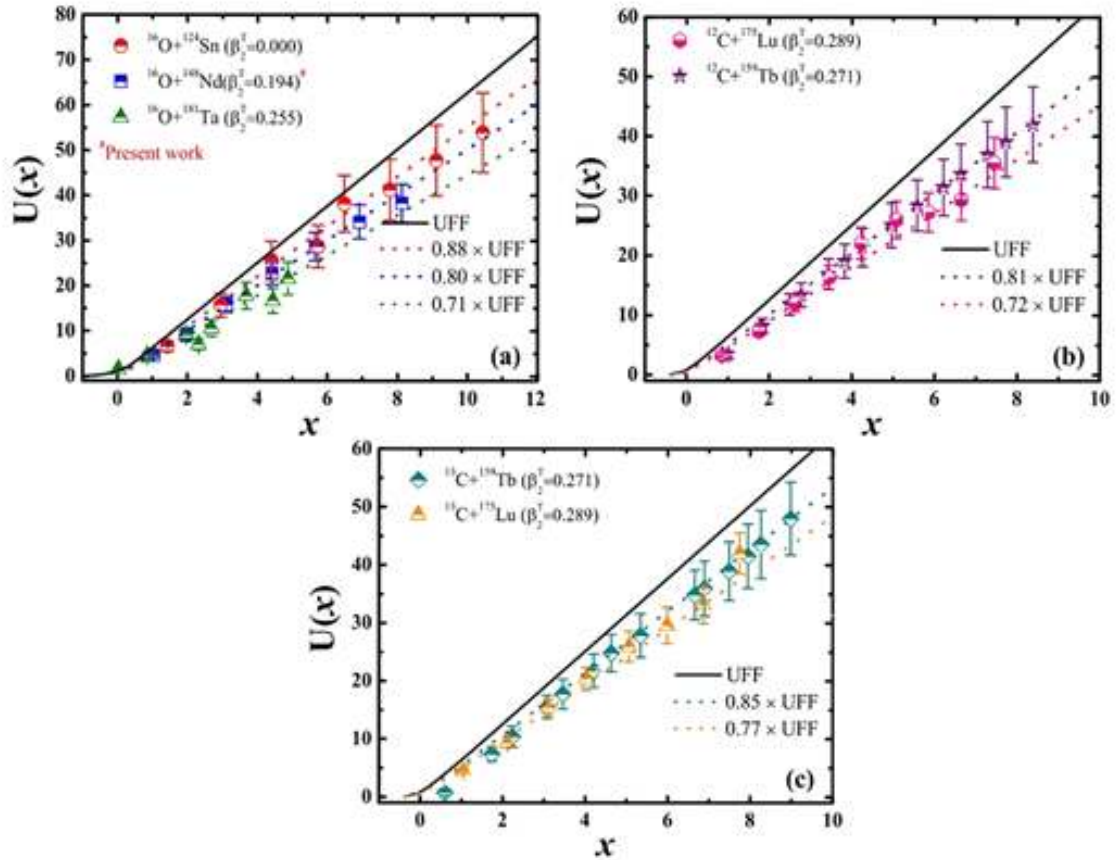


Fig 5.1.4.1: The experimental fusion functions (EFFs) along with the universal fusion function (UFF) for  $^{16}\text{O}+^{148}\text{Nd}$  and some other systems from literature [3–7]. The solid line represents the UFF and dotted lines represent best fits to EFFs for different systems.

The couplings of inelastic excitations and transfer channels are not so effective at energies above the Coulomb barrier. Therefore, any deviation in the EFFs from the UFF is attributed to the breakup of the projectile. It can be seen clearly from the figure that the EFFs for all the systems are well suppressed. As can be noticed from these figures, the EFFs for the systems having same projectiles ( $^{16}\text{O}$ ,  $^{13,12}\text{C}$ ), but different values of deformation parameters for targets are suppressed by different factors. The suppression factor for the system  $^{16}\text{O}+^{124}\text{Sn}$  ( $\beta_2^T = 0.000$ ) is 0.88, while for the systems  $^{16}\text{O} + ^{148}\text{Nd}$  ( $\beta_2^T = 0.194$ ) and  $^{16}\text{O} + ^{181}\text{Ta}$  ( $\beta_2^T = 0.255$ ) the suppression factors are 0.80 and 0.71, respectively. This means that the contribution of ICF increases with the deformation of the target. However, the ICF fraction,  $F_{\text{ICF}}$  (%) for the system  $^{16}\text{O} + ^{181}\text{Ta}$  is slightly away from the linearly increasing trend. This may be because of missing cross sections of some ER channels, which could not be measured due to limitations of the stacked foil activation technique. Hence, the suppression factor for this system is also smaller, i.e., 0.71, which would be expected to go up if all possible  $\alpha$ -emitting channels could be measured. On the other hand, the suppression factors for the system  $^{12}\text{C}+^{159}\text{Tb}$  ( $\beta_2^T = 0.271$ ) and  $^{12}\text{C}+^{175}\text{Lu}$  ( $\beta_2^T = 0.289$ ) are found to be 0.81 and 0.72, respectively, which are displayed in panel (b). As can be seen in panel (c), the suppression factors for the systems  $^{13}\text{C}+^{159}\text{Tb}$  ( $\beta_2^T = 0.271$ ) and  $^{13}\text{C} + ^{175}\text{Lu}$  ( $\beta_2^T = 0.289$ ) are 0.85 and 0.75, respectively. These results show that the CF suppression factor decreases with increasing deformation of the target nuclei for a given projectile.

#### REFERENCES:

- [1] L. F. Canto, P. R. S. Gomes, J. Lubian, L. C. Chamon and E. Crema, *J. Phys. G: Nucl. Part. Phys.* **36**, 015109 (2009).
- [2] P. K. Giri, D. Singh, A. Mahato, S. B. Linda *et al.*, *Phys. Rev. C* **100**, 024621 (2019).
- [3] A. Yadav, V. R. Sharma, P. P. Singh, D. P. Singh *et al.*, *Phys. Rev. C* **85**, 034614 (2012).
- [4] H. Kumar, S. A. Tali, M. A. Ansari, D. Singh *et al.*, *Nucl. Phys. A* **960**, 53 (2017).
- [5] A. Yadav, V. R. Sharma, P. P. Singh, R. Kumar *et al.*, *Phys. Rev. C* **86**, 014603 (2012).
- [6] D. Singh, S. B. Linda, P. K. Giri, A. Mahato *et al.*, *Phys. Rev. C* **97**, 064610 (2018).
- [7] D. P. Singh, Unnati, P. P. Singh, A. Yadav *et al.*, *Phys. Rev. C* **80**, 014601 (2009).

### 5.1.5 Fragmentation dynamics and neutron multiplicity measurements for super-heavy nuclei

Shruti<sup>1</sup>, H. Arora<sup>1</sup>, N. Saneesh<sup>2</sup>, D. Arora<sup>2</sup>, Kajol Chakraborty<sup>3</sup>, A. Kaur<sup>1</sup>, Amit<sup>1</sup>, Subodh<sup>1</sup>, Chetan<sup>1</sup>, Raghav<sup>1</sup>, K. S. Golda<sup>2</sup>, A. Jhingan<sup>2</sup>, Mohit Kumar<sup>2</sup>, Hardev Singh<sup>4</sup>, H. J. Wollersheim<sup>5</sup>, J. Gerl<sup>5</sup>, S. Mandal<sup>3</sup>, P. Sugathan<sup>2</sup> and B. R. Behera<sup>1</sup>

<sup>1</sup>Department of Physics, Panjab University, Chandigarh 160014, India

<sup>2</sup>Inter-University Accelerator Centre, Aruna Asif Ali Marg, New Delhi 110067, India

<sup>3</sup>Department of Physics and Astrophysics, University of Delhi, Delhi 110007, India

<sup>4</sup>Department of Physics, Kurukshetra University, Kurukshetra 136119, India

<sup>5</sup>GSI, Darmstadt, Germany

Heavy ion induced nuclear reactions for the synthesis of super-heavy elements (SHE) involve numerous complex processes and have extensively been studied for many decades through experimental and theoretical approaches. It is well established that there is a significant contribution from quasi-fission (QF) along with fusion-fission (FF) in fusion between two heavy nuclei [1]. A number of experimental probes such as mass distribution, mass-energy and mass-angle correlations and neutron multiplicity have been adopted to disentangle these processes. Neutron multiplicity measurement was proved to be the most suitable probe in the heavy or super-heavy mass region as it helped in determining the timescales of QF and FF [2]. Current study is based on the study of fission dynamics of a super-heavy system  $^{280}\text{Cn}$  ( $Z=112$ ) using a deformed  $^{232}\text{Th}$  target. Pulsed beam of  $^{48}\text{Ti}$  was bombarded on a  $250\ \mu\text{g}/\text{cm}^2$  thick  $^{232}\text{Th}$  target. Two multi-wire proportional counters (MWPCs) with active area of  $10\times 20\ \text{cm}^2$  ( $\theta_{\text{fold}} = \pm 66^\circ$ ) were used for the detection of fission fragments. Neutrons were detected using the National Array of Neutron Detectors (NAND) facility consisting of 100 organic liquid scintillators (BC501A). Data were acquired using the upgraded indigenous VME controller ROSE and the MARS (Multi-parameter Acquisition with Root-based Storage) software [4].

Pulse shape discrimination (PSD) based on zero-cross over technique and time of flight (TOF) method were used for the discrimination of neutrons and gamma rays. TOF spectra were calibrated using a precise time calibrator and the prompt  $\gamma$  peak as the time reference. To distinguish the neutrons and  $\gamma$  events, a two-dimensional gate (as shown by the closed-loop in Fig. 5.1.5.1) was applied on the calibrated neutron TOF spectra. Further it was gated with fission events in order to obtain neutrons corresponding to fission. The calibrated and gated neutron TOF was then converted to neutron energy. The neutron detector efficiency corrections were performed using the FLUKA code [3]. Double differential neutron energy spectra for the neutron detector placed at  $54^\circ$  and  $72^\circ$  with respect to the beam direction are shown in Fig. 5.1.5.2. Moving-source fitting method was used for the extraction of pre- and post-scission components of neutron multiplicities ( $\nu_{\text{pre}}$  and  $\nu_{\text{post}}$ ). Further fission-fragment mass gates will be applied over 100 neutron detectors to obtain the mass-gated neutron multiplicity.

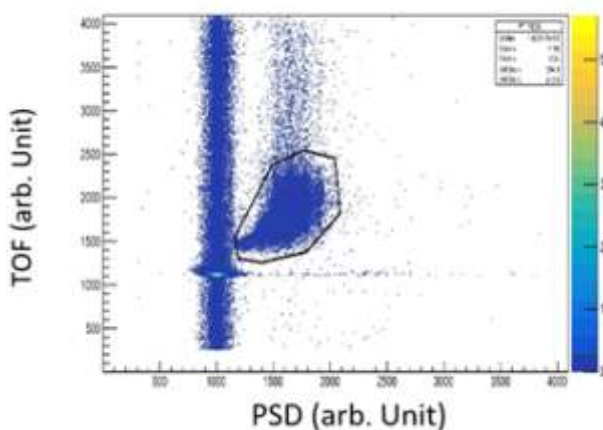


Fig 5.1.5.1: PSD-TOF spectrum for the neutron detector at  $54^\circ$  with respect to the beam direction.

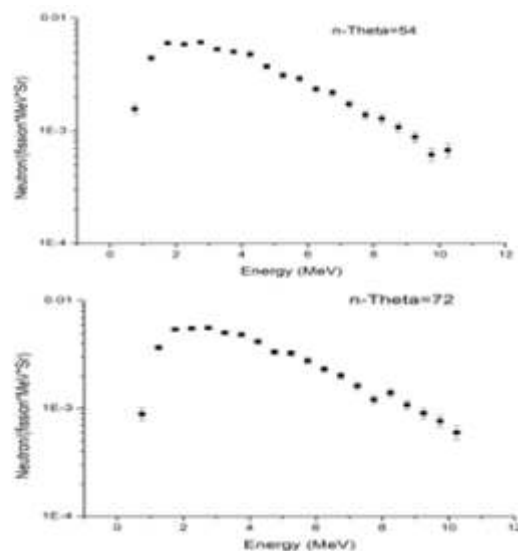


Fig 5.1.5.2: Double-differential neutron energy spectra obtained from two neutron detectors.

#### REFERENCES:

- [1] D. J. Hinde *et al.*, Phys. Rev. C **45**, 1229 (1992).
- [2] Y. Aritomo *et al.*, Nuc. Phys. A **759**, 342 (2005).
- [3] FLUKA, A multi particle transport code, CERN.
- [4] <http://www.iuac.res.in/NIAS/MARS/>

### 5.1.6 Mass dependent neutron multiplicity studies in the $^{30}\text{Si}+^{232}\text{Th}$ reaction

Prashant N. Patil<sup>1</sup>, N. M. Badiger<sup>1</sup>, M. M. Hosamani<sup>1</sup>, A. Vinayak<sup>1</sup>, S. K. Duggi<sup>2</sup>, Neeraj Kumar<sup>3</sup>, N. K. Rai<sup>4</sup>, D. Arora<sup>5</sup>, R. N. Sahoo<sup>6</sup>, A. Gandhi<sup>4</sup>, S. Dhuri<sup>9</sup>, C. V. Midhun<sup>7</sup>, K. Hajara<sup>7</sup>, F. S. Shana<sup>7</sup>, A. Kaur<sup>8</sup>, P. Sherpa<sup>3</sup>, Mohit Kumar<sup>5</sup>, N. Saneesh<sup>5</sup>, K. S. Golda<sup>5</sup>, A. Jhingan<sup>5</sup>, K. Ramachandran<sup>9</sup>, P. Sugathan<sup>5</sup> and B. K. Nayak<sup>9</sup>

<sup>1</sup>Department of Studies in Physics, Karnatak University, Dharwad 580003, India

<sup>2</sup>Department of Nuclear Physics, Andhra University, Visakhapatnam 530003, India

<sup>3</sup>Department of Physics and Astrophysics, University of Delhi, Delhi 110007, India

<sup>4</sup>Department of Physics, Banaras Hindu University, Varanasi 221005, India

<sup>5</sup>Inter-University Accelerator Centre, Aruna Asaf Ali Marg, New Delhi 110067, India

<sup>6</sup>Department of Physics, Indian Institute of Technology Ropar, Rupnagar 140001, India

<sup>7</sup>Department of Physics, University of Calicut, Calicut 673635, India

<sup>8</sup>Department of Physics, Panjab University, Chandigarh 160014, India

<sup>9</sup>Nuclear Physics Division, Bhabha Atomic Research Centre, Mumbai 400085, India

The fission fragment-mass-TKE distributions along with neutron multiplicities in the system  $^{50}\text{Ti}+^{208}\text{Pb}$  forming the compound nucleus (CN)  $^{258}\text{Rf}$  at  $E_{\text{lab}} = 294$  MeV have been studied [1]. Authors of this paper reported that the observed results are consistent with fusion-fission process with a possibly small contribution coming from quasi-fission events [1]. More recently, Thakur et al. have studied the mass-gated neutron multiplicity at  $E_{\text{lab}} = 273$  MeV in the system  $^{48}\text{Ti}+^{208}\text{Pb}$  forming the CN  $^{256}\text{Rf}$  and found non-negligible quasi-fission events [2]. In the present experiment, mass-gated neutron multiplicity measurements have been carried out for the more asymmetric system  $^{30}\text{Si}+^{232}\text{Th}$ , forming a similar CN  $^{262}\text{Rf}$  to understand the reaction mechanism of fusion-fission and quasi-fission in the near superheavy nucleus. The experiment has been carried out using the NAND facility [3] at IUAC in the  $E_{\text{lab}}$  range of 165 – 210 MeV. Pulsed beam of  $^{30}\text{Si}$ , with a pulse separation of 250 ns, has been bombarded on the  $^{232}\text{Th}$  target of thickness 1.1 mg/cm<sup>2</sup>. The target was kept at the centre of the scattering chamber with 4 mm thick walls and 100 cm diameter. The target ladder was tilted at an angle of 30° with respect to the beam axis in order to minimize the shadowing to position-sensitive multi-wire proportional counters (MWPC). One of the MWPC detectors kept at an angle of 40° with respect to beam direction is at a distance of 26 cm whereas the other MWPC detector, kept at an angle of 112°, is at a distance of 22 cm from the target. Both MWPCs have been operated with isobutene gas of 3.5 mbar gas pressure. Two silicon surface barrier detectors (SSBD), kept at  $\pm 12.5^\circ$  with respect to the beam direction, are used to monitor the beam flux. Time of flight (TOF) of the fission fragments with reference to the onset of the beam pulse are obtained from fast timing signals of MWPC detectors, from which it is possible to isolate the fission events from projectile-like and target-like events. Two dimensional TOF spectra, thus obtained from MWPCs, is shown in Fig. 5.1.6.1. Forty nine organic liquid scintillators (5" diameter, 5" thick, cylindrical in shape), situated at a distance of 175 cm from the target, are used to record the neutrons in coincidence with the binary fission events detected using the two large area (20 cm  $\times$  10 cm) MWPCs [4]. The beam dump is placed at 4 m downstream from the target and beam line is well-shielded with layers of lead bricks and borated paraffin to block scattered neutrons from reaching the neutron detector. The neutrons were discriminated from  $\gamma$  rays by generating two-dimensional correlation plots of pulse shape discrimination (PSD) versus TOF, as shown in Fig. 5.1.6.2. The detectors signals are acquired by using a VME-based data acquisition system. The filtered RF (logical OR of the two fission fragments AND-gated with RF of the beam pulse) is used as the trigger for the data acquisition system for list mode collection of data with Multi-parameter Acquisition with Root-based Storage (MARS) software. The detailed analysis of the data is in progress.

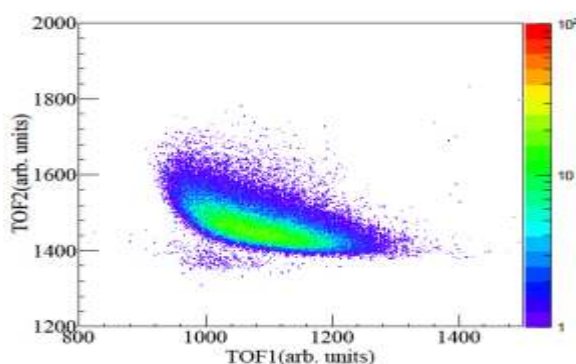


Fig 5.1.6.1: Time correlation spectra of complementary fission fragments detected in the two MWPCs at  $E_{\text{lab}} = 210$  MeV.

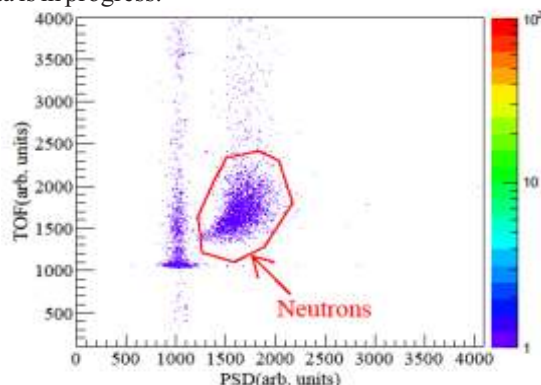


Fig. 5.1.6.2: TOF vs PSD plot used for separating the neutrons from  $\gamma$  rays. The neutron lobe is outlined using a red solid line.

#### REFERENCES:

- [1] S. Appannababu, M. Cinausero, T. Marchi, F. Gramegna *et al.*, Phys. Rev. C **94**, 044618 (2016).
- [2] M. Thakur, B. R. Behera, R. Mahajan, G. Kaur *et al.*, Phys. Rev. C **98**, 014606 (2018).
- [3] N. Saneesh, K. S. Golda, A. Jhingan, S. Venkataramanan *et al.*, Nucl. Instrum. Methods A **986**, 164754 (2021).
- [4] A. Jhingan, Pramana – J. Phys **85**, 483 (2015).

### 5.1.7 Nature of dissipation and shell effects in fusion-fission via neutron multiplicity measurements

M. Shareef<sup>1</sup>, E. Prasad<sup>1</sup>, A. Jhingan<sup>2</sup>, N. Saneesh<sup>2</sup>, K. S. Golda<sup>2</sup>, P. Sugathan<sup>2</sup> and Santunu Pal<sup>3</sup>

<sup>1</sup>Department of Physics, School of Physical Sciences, Central University of Kerala, Kasaragod 671316, India

<sup>2</sup>Inter-University Accelerator Centre, Aruna Asaf Ali Marg, New Delhi 110067, India

<sup>3</sup>CS-6/1, Golf Green, Kolkata 700095, India

Fundamental feature of the fission process is its dynamical nature due to the dissipative drag associated with the collective motion of nuclear matter. Dissipation in fission accounts for the coupling between collective nuclear motion with intrinsic degrees of freedom. The effect of nuclear dissipation is observed to be significant for heavy nuclei at high excitation energies and large angular momenta. Theoretical modelling of fission most often relies on statistical approach, which is recognized as a powerful tool to be used to interpret the experimental observables. There are two kinds of arguments about the nature of dissipation based on its temperature dependence. In an evaporation residue (ER) cross section measurement for the  $^{32}\text{S}+^{184}\text{W}$  reaction [1], it was found that the strength of nuclear dissipation required to reproduce the experimental ER excitation function substantially increases with the excitation energy of the compound nuclei (CN). In the neutron multiplicity measurements from the fission of  $^{212,214,216}\text{Rn}$  [2] and  $^{213,215,217}\text{Fr}$  [3] CN, it was noticed that the deduced strength of dissipation had strong temperature dependence and was reported to increase with increase in temperature of the CN. However, in an extensive theoretical investigation by Lestone and McCalla [4], it was pointed out that there was no evidence to suggest that the nuclear dissipation had a temperature dependence and such temperature-dependent dissipation strength, reported in the literature, could be the result of inadequate modelling of the fission process.

While considering the above-mentioned facts, isotopes of Ra could be an ideal candidate to explore the structural and dynamical effects in fission as it comes immediately after Rn and Fr in the Periodic Table. The experiment was performed using a pulsed beam of  $^{30}\text{Si}$  from the 15 UD Pelletron + Super Conducting Linear Accelerator facility of IUAC. Beam with a pulse separation of 250 ns was used in the experiment to bombard the targets of enriched  $^{182,184,186}\text{W}$  isotopes of thickness  $405\ \mu\text{g}/\text{cm}^2$ ,  $450\ \mu\text{g}/\text{cm}^2$  and  $331\ \mu\text{g}/\text{cm}^2$ , respectively, with carbon backing of  $25\ \mu\text{g}/\text{cm}^2$ . Among the populated  $^{212,214,216}\text{Ra}$  CN,  $^{214}\text{Ra}$  has a major neutron shell closure of  $N = 126$ . Two silicon surface barrier detectors were placed at  $\pm 12.5^\circ$  with respect to the beam direction, inside the scattering chamber, to detect the elastically scattered beam particles for beam flux monitoring. The complimentary fragments from fission or fission-like events were detected using a pair of identical position-sensitive multi-wire proportional counters (MWPCs). These MWPC's were mounted at  $\pm 69^\circ$  with respect to the beam direction on either side such that the detectors were capable of detecting the complimentary fission fragments. Both detectors had an active area of  $11 \times 16\ \text{cm}^2$  and were operated with isobutane gas at 3.5 mbar pressure.

In fusion-fission reactions in the heavy mass region, neutrons are emitted from the composite system from the touching configuration till the scission point, as well as from the two fission fragments. These emitted neutrons were detected in coincidence with the complimentary fission fragments using 50 organic liquid scintillator detectors (BC 501A) of the National Array of Neutron Detectors (NAND) facility. The pre-scission and post-scission neutron multiplicities and temperatures were obtained by the spectral deconvolution of the measured double differential neutron multiplicity spectra [5]. The measured  $v_{\text{pre}}$  excitation function for the three reactions were analysed within the framework of the statistical model, which incorporated shell correction in fission barrier and level densities, collective enhancement in level density (CELD) and dissipation in fission width. No indication for the effect of shell closure in dissipation was found in this work in the measured excitation energy range. The deduced strength of dissipation did not reveal any temperature dependence.

#### REFERENCES:

- [1] B. B. Back *et al.*, Phys. Rev. C **60**, 044602 (1999).
- [2] Varinderjit Singh *et al.*, Phys. Rev. C **87**, 064601 (2013).
- [3] Rohit Sandal *et al.*, Phys. Rev. C **87**, 014604 (2013).
- [4] J. P. Lestone and S. G. McCalla, Phys. Rev. C **79**, 044611 (2009).
- [5] M. Shareef *et al.*, Phys. Rev. C **99**, 024618 (2019).

### 5.1.8 The study of chiral nature in $^{128}\text{La}$ using lifetime measurements

Umakant Lamani<sup>1</sup>, Pragma Das<sup>1</sup>, Himanshu Kumar Singh<sup>1</sup>, A. Sharma<sup>2</sup>, S. Chakraborty<sup>3</sup>, K. Katre<sup>3</sup>, Yashraj<sup>3</sup>, S. Muralithar<sup>3</sup> and R. P. Singh<sup>3</sup>

<sup>1</sup>Department of Physics, Indian Institute of Technology Bombay, Powai, Mumbai 400076, India

<sup>2</sup>Department of Physics, Himachal Pradesh University, Shimla 171005, India

<sup>3</sup>Nuclear physics group, Inter-University Accelerator Centre, New Delhi 110067, India

The chiral symmetry involves the alignment of three angular momenta – corresponding to valence proton, neutron and the core - along the three principal axes of triaxial nuclei. Nuclei in the mass region 130 being  $\gamma$ -soft are good candidates for chirality. It has been argued [1, 2, 3] that the chiral geometry can only be achieved with a sizable amount of rotation, i.e. above a certain rotational frequency called the critical frequency ( $\omega_c$ ). Further more, the chiral geometry may disappear at high rotational frequency when the valence proton and neutron start aligning along the rotational axis. The theoretical works by Hamamoto [1] and Pasternak [2] have clearly laid out the selection rules for the electromagnetic properties for nuclei exhibiting chiral behaviour: (i) both chiral partner bands should have similar reduced transition probabilities (B(M1) and B(E2) values) for the intraband transitions and (ii) the B(M1) values should be low and high alternately for the intraband transitions within the band; such an alternating behaviour should be in opposite phase for the interband transitions between the two chiral partner bands. The nuclei  $^{126}\text{Cs}$  and  $^{128}\text{Cs}$  clearly demonstrate these rules [3, 4]. However,  $^{132}\text{La}$  and  $^{134}\text{Pr}$  fail to do so. In the recent works for  $^{124}\text{Cs}$  [5, 6], the staggering behavior of B(M1) values for the intraband transitions have been reported; but there were no experimental results for the interband transitions between the two chiral partner bands. Our focus was to experimentally obtain the B(M1) and B(E2) values for the intraband and interband transitions of the proposed chiral bands in  $^{128}\text{La}$  from the lifetime measurement using Doppler shift attenuation method (DSAM). We will then be able to check the selection rules [1, 2].

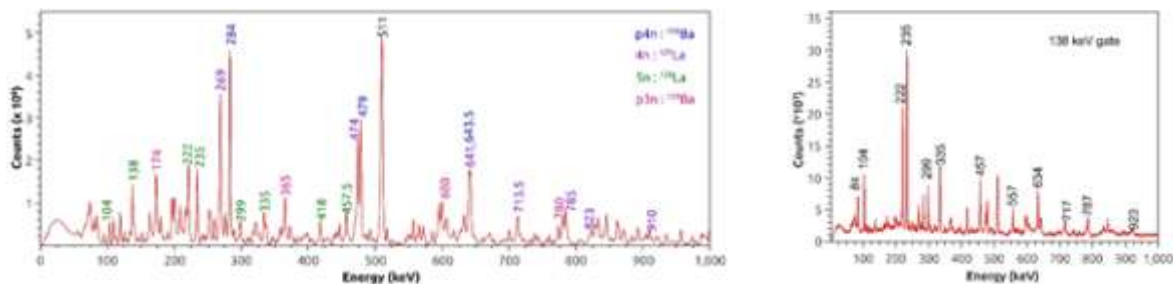


Fig 5.1.8.1: (Left) The total projected spectrum obtained from the  $^{19}\text{F}+^{114}\text{Cd}$  reaction at  $E_{\text{lab}} = 94$  MeV and (Right) 138 keV gated spectrum.

An experiment was performed to populate the high spin states of  $^{128}\text{La}$  in October 2020 at IUAC. The  $^{19}\text{F}$  beam, delivered by the Pelletron, was bombarded on to 4.85 mg/cm<sup>2</sup> thick, isotopically enriched  $^{114}\text{Cd}$  target. Our nucleus of interest,  $^{128}\text{La}$  was formed by 5n evaporation channel. The excitation function plot was made with respect to  $E_{\text{lab}}$  and finally the experiment was carried out at  $E_{\text{lab}} = 94$  MeV. This energy was chosen, in order to populate higher angular momentum states along with maintaining good production cross-section of the residues. The two-fold  $\gamma$ - $\gamma$  coincidence data were collected using the Indian National GammaArray (INGA) consisting of 14 Compton-suppressed Clover detectors. The Clover detectors were placed at 32° (three detectors), 57° (two detectors), 90° (four detectors), 123° (one detector) and 148° (four detectors) with respect to the beam direction. The data were sorted using the computer program CANDLE. The energy calibration (0.5 keV per channel) of the list mode data was carried out using a radioactive source of  $^{152}\text{Eu}$  and further, online calibration was also performed. The total projected spectrum obtained in this work is shown in the left panel of Fig. 5.1.8.1. The offline data were sorted into symmetric and three (all vs. forward (32°), all vs. 90° and all vs. backward (148°)) angle dependent asymmetric  $E_{\gamma}$ - $E_{\gamma}$  matrices. The partial level scheme of  $^{128}\text{La}$  from the present work is consistent with the previously established level scheme [7] and is adopted in this work. We could see the transition up to 19<sup>+</sup> spin state in the yrast band but the partner band has not been observed in these data. The gate set on the yrast band (138 keV) is shown in the right panel of Fig. 5.1.8.1. In the yrast band, we were able to see the lineshapes of a few transitions (299 and 335 keV) corresponding to low spin states. The lineshapes of both the transitions have some contamination, so careful analysis has to be performed to extract the lifetimes.

#### REFERENCES:

- [1] I. Hamamoto, *Int. J. Mod. Phys. E* **20**, 373 (2011).
- [2] A. A. Pasternak, *Phys. At. Nuclei* **73**, 1351 (2010).
- [3] E. Grodner *et al.*, *Phys. Rev. Lett.* **97**, 172501 (2006).
- [4] E. Grodner *et al.*, *Phys. Lett. B* **703**, 46 (2011).
- [5] T. Marchlewskiet *et al.*, *Act. Phys. Pol. B* **46**, 689 (2015).
- [6] K. SelvaKumar *et al.*, *Phys. Rev. C* **92**, 064307 (2015).
- [7] K. Y. Ma *et al.*, *Phys. Rev. C* **85**, 037301 (2012).

### 5.1.9 GEANT4 simulations for crosstalk calculations

J. Kaur<sup>1</sup>, R. Kumar<sup>2</sup> and R. P. Singh<sup>2</sup>

<sup>1</sup>Department of Physics, Guru Nanak Dev University, Amritsar, Punjab 143005, India

<sup>2</sup>Nuclear Physics Group, Inter-University Accelerator Centre, New Delhi 110067, India

The proposed CPDA array of IUAC will comprise of CsI scintillators coupled to Si-PIN photodiodes S3590-08 and detect light charged particles such as protons and alphas.

**Objective of Simulations:** Event by event analysis using Monte Carlo Geant4 framework simulates the crosstalk of the particles (proton and alpha) between neighboring crystals. Simulations are performed using NPTool framework that takes the full advantage of both ROOT analysis framework and Geant4 simulation toolkit.

**The following conditions were considered for these calculations:**

1. CsI(Tl) crystals (daughter volumes) having dimension 20 mm × 20 mm with 3mm thickness assembled as quads on single PCB (mother volume).
2. Square shaped (60 mm × 60 mm) 18 PCBs were considered in Rhombicuboctahedron geometry.
3. 18 PCBs, with 4 crystals on each makes a total of 72 crystals which are incorporated in the present simulations.
4. The entire array to be housed inside a hollow quasi-spherical aluminum chamber of thickness ~3 mm.

**Source of charged particles:** Radioactive source modelled as general particle source (GPS) is placed at the center of the aluminum chamber with source to crystal distance ~6 cm. GPS is set to emit decaying particles isotropically by incorporating standard G4Radioactive decay model in Physicslist. To study the interaction of emitted (secondary) particles from the source, physics processes like electromagnetic and hadronic are included in PhysicsList class. Physics processes are set to occur only when the particles travel through the sensitive volume. In the present case only CsI crystals are declared as sensitive volume.

**Analysis:** The simulation output generates the event-by-event energy deposition in the sensitive volumes by secondary particles like proton, alpha, gamma photons and electrons. Particles can be in any region of the model (source), where they are emitted isotropically. Monte Carlo simulations are performed for monoenergetic photons and electrons from 5 keV to 10 MeV. The more detailed information like location of different particles in any region of the array, the exact physical process that occurs in different regions and the various secondary particles created during the interaction can be extracted from the output. The main processes, in which particles lose energy are excitation and ionization. The information is collected and analyzed event by event using Root libraries.

**Result:** Geant4 simulations were performed for the isotropic distribution for protons and alpha particles. The crosstalk analysis has been performed for proton and alpha particles emitted by the source. Fig. 5.1.9.1 shows the graph between event numbers and detectors hit by those events. It can be seen that, in the range of events 91 to 100 only event no. 96 hit the multiple crystals. Further analysis has been done to extract the energy deposition by the alpha particle (event no. 96) in individual crystal. Fig. 5.1.9.2 shows the number of steps taken by the particle in each crystal. The total energy deposited by the particle in a crystal is directly proportional to the number of steps of the particle in that crystal. From preliminary analysis of the data, it has been observed that there is no cross talk up to 20 MeV for protons and the rate of crosstalk is ~1% for alpha particles. Further analysis is in progress.

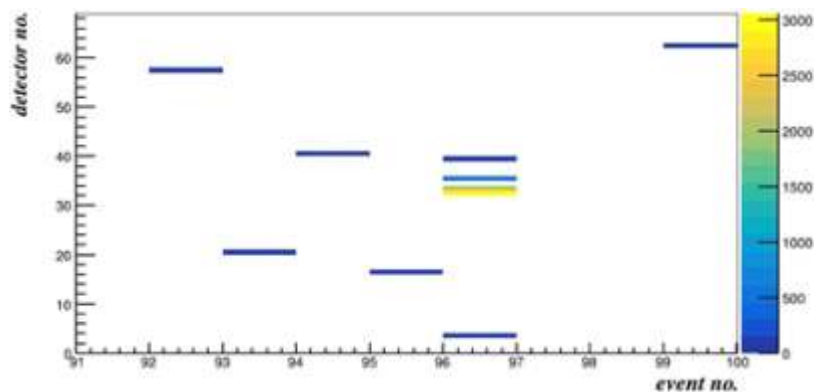


Fig 5.1.9.1: Detector hits corresponding to the event numbers in the simulation.

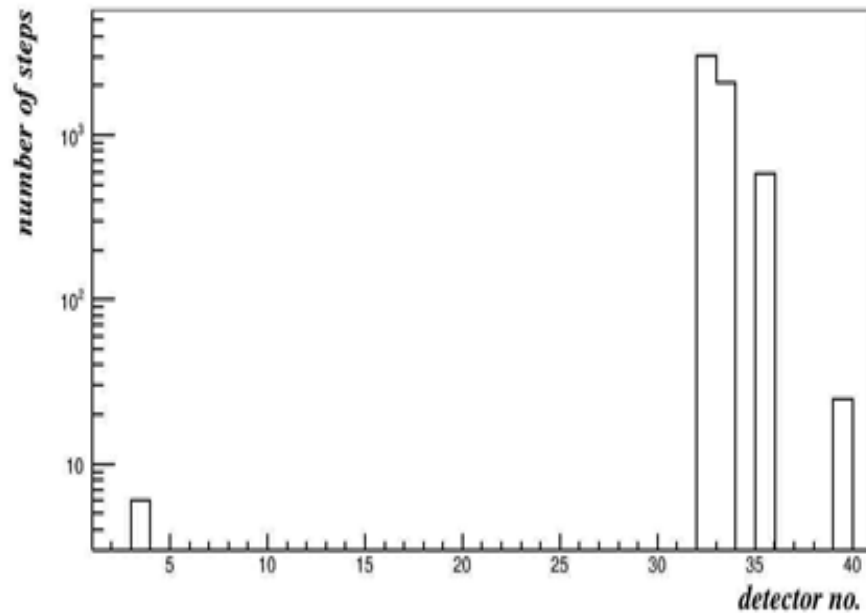


Fig 5.1.9.2: The number of steps traversed by the particle in each detector.

### 5.1.10 Forward recoil range distribution measurement for the system $^{14}\text{N} + ^{169}\text{Tm}$

S. Kumar<sup>1</sup>, Pankaj K. Giri<sup>2</sup> and R. Kumar<sup>1</sup>

<sup>1</sup>Nuclear Physics Group, Inter-University Accelerator Centre, New Delhi 110067, India

<sup>2</sup>Department of Physics, Central University of Jharkhand, Ranchi 835222, India

The forward recoil range distributions (FRRDs) of evaporation residues (ERs), produced in the reaction  $^{14}\text{N} + ^{169}\text{Tm}$ , were measured at IUAC. The target foils and Al-catcher foils were prepared at IUAC using the rolling and thermal evaporation vacuum deposition technique, respectively. The target foils were 0.5 mg/cm<sup>2</sup> thick and thickness of Al-catcher foils was chosen to be 20 – 50 μg/cm<sup>2</sup> so that recoiling ERs may get trapped in their respective thickness. Several ERs populated via complete fusion (CF) and/or incomplete fusion (ICF) were identified viz.  $^{179}\text{Os}(4n)$ ,  $^{179}\text{Re}(p3n)$ ,  $^{176}\text{W}(\alpha 3n)$ ,  $^{175}\text{W}(\alpha 4n)$ ,  $^{178}\text{Re}(p4n)$ ,  $^{177}\text{W}(\alpha 2n)$  and  $^{174}\text{W}(\alpha 5n)$ .

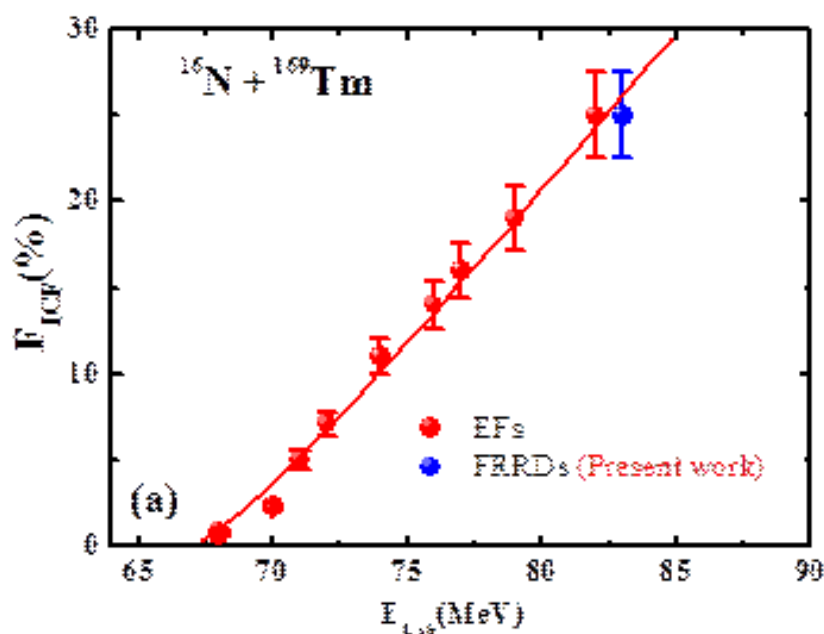


Fig 5.1.10.1: Incomplete fusion fraction ( $F_{ICF}$ ), extracted from EF and FRRD measurements, as a function of the projectile energy for the system  $^{14}\text{N} + ^{169}\text{Tm}$ .

FRRD measurement can give direct evidence of CF and ICF contribution for a particular system. Because of the requirement of a large number of catcher foils, the data reliability is one of the big concerns in this method. An effort was made to check the reliability of FRRD data by comparing with the excitation function (EF) data for the same system. In Fig. 5.1.10.1, the incomplete fusion fraction ( $F_{ICF}$ ), obtained from FRRD measurement, shows a good agreement with the same obtained from EF within the experimental uncertainty. The comparison thus exhibits the reliability of presently measured FRRD data.

#### REFERENCES:

- [1] Sushil Kumar, Pankaj K. Giri and R. Kumar, *Ind. J. Pure and App. Phys.* **57**, 562 (2019).  
 [2] R. Kumar, Vijay R. Sharma, Abhishek Yadav, Pushpendra P. Singh *et al.*, *Phys. Rev. C* **96**, 054614 (2017).

### 5.1.11 Angular distribution of evaporation residues populated through complete and incomplete fusion

Pankaj K. Giri<sup>1</sup>, Amritraj Mahato<sup>1</sup>, D. Singh<sup>1</sup>, Sneha B. Linda<sup>1</sup>, Harish Kumar<sup>2</sup>, Suhail A. Tali<sup>2</sup>, M. Afzal Ansari<sup>2</sup>, R. Kumar<sup>3</sup>, S. Muralithar<sup>3</sup> and R. P. Singh<sup>3</sup>

<sup>1</sup>Department of Physics, Central University of Jharkhand, Ranchi 835222, India

<sup>2</sup>Department of Physics, Aligarh Muslim University, Aligarh 202002, India

<sup>3</sup>Nuclear Physics Group, Inter-University Accelerator Centre, New Delhi 110 067, India

The present experiment was performed using the 15UD Pelletron at IUAC. Measurements of angular distributions (ADs) of evaporation residues (ERs) were carried out in the General Purpose Scattering Chamber (GPSC). A typical annular stack of target-catcher assembly, covering the angular zone  $0^\circ - 8^\circ$  to  $42^\circ - 51^\circ$ , employed for the measurement of ADs of ERs is displayed in panel (a) of Fig. 5.1.11.1.

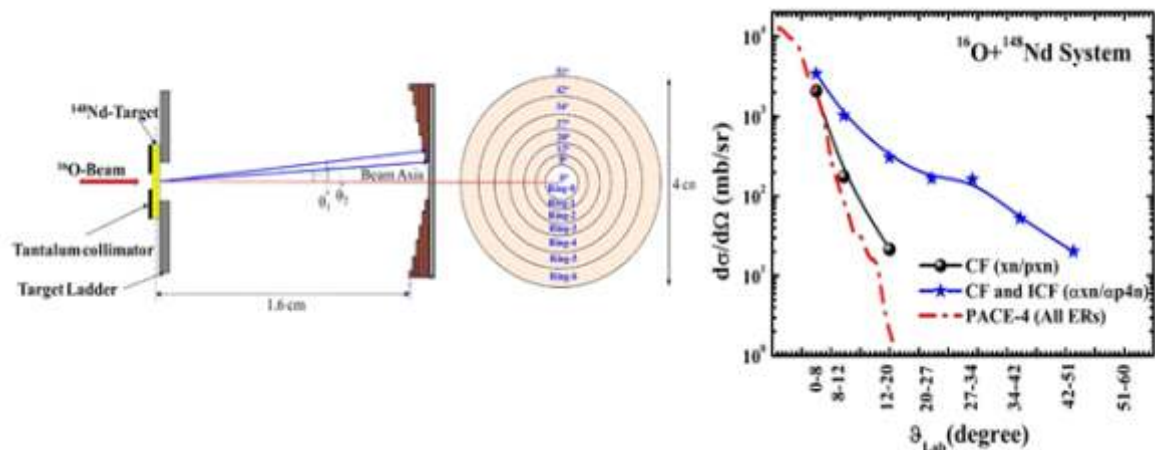


Fig. 5.1.11.1: (a) Experimental setup used for the measurement of angular distributions of ERs. (b) Measured total fusion (CF+ICF) and CF (xn+pxn) angular distributions along with theoretical predictions of PACE4 for the system  $^{16}\text{O} + ^{148}\text{Nd}$  at projectile energy  $\approx 6$  MeV/nucleon.

An attempt was made to understand the heavy-ion reaction dynamics through ADs of ERs at projectile energy above the Coulomb barrier. The ADs of six ERs  $^{159,158}\text{Er}(xn)$ ,  $^{159}\text{Ho}(pxn)$ ,  $^{157,155}\text{Dy}(\alpha xn)$  and  $^{155}\text{Tb}(\alpha pxn)$ , produced in the system  $^{16}\text{O} + ^{148}\text{Nd}$  were measured at projectile energy  $\approx 6$  MeV/nucleon [1]. The measured cross section of each angular ring was divided by its corresponding solid angle to get the differential cross section of ERs. The differential cross sections plotted as a function of different angular zones are called ADs of ERs. Angular distribution of ERs can be calculated using the statistical model code PACE4. The PACE4 calculations for the present system show that the ERs are emitted within a folding angle of  $\pm 14^\circ$ , peaking at around  $5^\circ$  (for complete fusion (CF)). The sum of measured differential cross sections for incomplete fusion (ICF) ( $\alpha$ -emitting) and CF (xn- and pxn-emitting) channels was estimated and compared with the sum of theoretical differential cross sections for all ER channels, as shown in panel (b) of Fig. 5.1.11.1. The present results of ADs reveal that the ERs populated via xn/pxn channels are emitted in the angular zone  $0^\circ - 20^\circ$ . These results were found to be in good agreement with the theoretical predictions made by PACE4. Thus, these ERs are expected to be populated only through complete fusion of  $^{16}\text{O}$  with  $^{148}\text{Nd}$ . However, the ERs populated via  $\alpha xn/\alpha pxn$  channels are found to be trapped at larger angular zone ( $0^\circ - 51^\circ$ ), as compared to PACE4 predictions for CF channels.

#### REFERENCES:

- [1] Pankaj K. Giri, Amritraj Mahato, D. Singh, Sneha B. Linda *et al.*, *Phys. Rev. C* **100**, 054604 (2019).

### 5.1.12 Coulomb excitation of $^{118}\text{Sn}$

I. Ahmed<sup>1</sup>, M. Saxena<sup>2</sup>, R. Kumar<sup>1</sup> and Eagle collaboration<sup>3</sup>

<sup>1</sup>Nuclear Physics Group, Inter-University Accelerator Centre, New Delhi 110067, India

<sup>2</sup>Institute of Nuclear and Particle Physics, Department of Physics and Astronomy, Ohio University, Athens, Ohio 45701, USA

<sup>3</sup>Heavy Ion Laboratory, University of Warsaw, Warsaw 05077, Poland

Sn-isotopes forms the longest chain of semi-magic nuclei enclosed between two doubly magic ( $^{100}\text{Sn}$  and  $^{132}\text{Sn}$ ) nuclei in the Segre-chart. These isotopes are of particular interest as they provide the stringent testing ground for nuclear structure models. The unique feature of these isotopes acts as a benchmark prototype for many theoretical studies. Shape coexistence has been discussed in Sn-isotopes [1-2] for several decades, existence of which was mainly attributed to 2p-2h excitations across the  $Z = 50$  shell closure. Recently Garrett et al., [3] suggested multiple shape coexistence of the low-lying states in the nearby  $^{110,112}\text{Cd}$  ( $Z = 48$ ) isotopes.

A Coulomb excitation experiment was performed at the Heavy Ion Laboratory, Warsaw, Poland to determine the shape of  $^{118}\text{Sn}$  nucleus. The main goal of this experiment was to measure the signs and the magnitudes of the quadrupole moments for the excited  $2^+$  states at 1229.6 keV, 2042 keV and 2403.2 keV, respectively. In addition, the transitional matrix elements between the low-lying states connecting the ground state and the intruder rotational band were supposed to be measured. The determination of the signs and magnitudes of the quadrupole moments in  $^{118}\text{Sn}$ , as well as the transitional matrix elements between the low-lying states (especially for the excited  $2_3^+$  (2403 keV) and  $0_3^+$  (2496 keV) states) are crucial for understanding the structure of  $^{118}\text{Sn}$  along with the interpretation of shape coexistence in this nucleus. This experiment was carried out with a  $^{32}\text{S}$  beam, accelerated from the U-200P Cyclotron, impinging on a highly enriched, 1 mg/cm<sup>2</sup> thick target of  $^{118}\text{Sn}$ . The target was backed by a thin carbon foil (10-20  $\mu\text{g}/\text{cm}^2$ ). The  $^{32}\text{S}$  beam of 90 MeV energy, which fitted well into the 'safe energy' criterion [5], ensured a pure electromagnetic interaction between the projectile and the target nuclei. Sixteen HPGe detectors with a photo-peak efficiency of  $\sim 0.5\%$  were used from the EAGLE array to detect the de-exciting gamma rays from the Coulomb excited  $^{118}\text{Sn}$  nuclei. BGO detectors, provided by the GAMMAPOOL, were used as anti-Compton shields. The ancillary detectors inside the compact Munich chamber, comprising of 48 pin diodes each having an active area of 0.25 cm<sup>2</sup>, were used covering an angular range from 120° to 167° with respect to the beam axis. The PIN diodes measured the back-scattered ions to allow the particle-gamma coincidence, which is required for the necessary background removal and the precise Doppler shift correction of the gamma rays [6].

The precise Doppler shift correction was performed using the particle-gamma scattering angles. A typical Doppler shift corrected spectrum is shown in Fig. 5.1.12.1. The first excited  $2^+$  state at 1229 KeV is clearly visible. Further analysis of data is in progress.

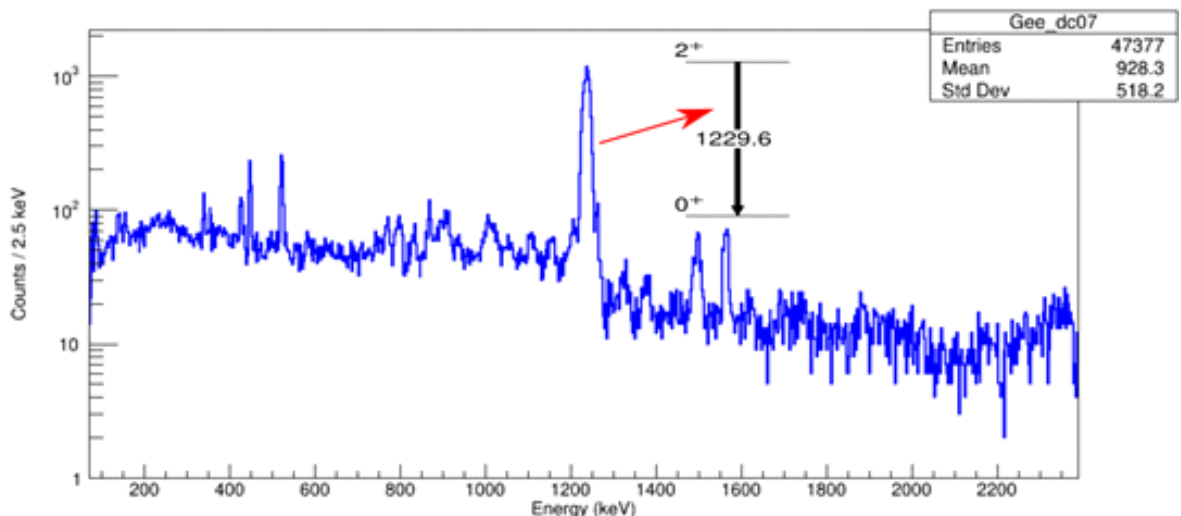


Fig. 5.1.12.1: Doppler shift corrected spectrum for one of the Germanium detectors.

#### REFERENCES:

- [1] J. Wood, K. Heyde, W. Nazarewicz, M. Huyse *et al.*, Phys. Rep. **215**, 101 (1992).
- [2] K. Heyde and J. L. Wood, Rev. Mod. Phys. **83**, 1467 (2011).
- [3] P. E. Garrett *et al.*, Phys. Rev. Lett. **123**, 142502 (2019).
- [4] M. Saxena *et al.*, Acta Phys. Pol. B **417**, 50 (2019).
- [5] D. Cline, Ann. Rev. Nucl. Part. Sci. **36**, 683 (1986).
- [6] A. Gorgen and W. Korten, J. Phys. G: Nucl Part. Phys. **43**, 024002 (2016).

### 5.1.13 Study of anomalous light particle spectra in heavy-ion induced fusion reactions

Honey Arora<sup>1</sup>, K. Rani<sup>1</sup>, Shruti<sup>1</sup>, M. Kumar<sup>2</sup>, S. Yadav<sup>1</sup>, A. Punia<sup>1</sup>, C. Sharma<sup>1</sup>, D. Arora<sup>2</sup>, S. Singh<sup>1</sup>, A. Kaur<sup>1</sup>, N. Saneesh<sup>2</sup>, Varinderjit Singh<sup>3</sup>, A. Jhingan<sup>2</sup>, K. S. Golda<sup>2</sup>, H. Singh<sup>4</sup>, P. Sugathan<sup>2</sup>, A. Kumar<sup>1</sup>, Gulzar Singh<sup>1</sup> and B. R. Behera<sup>1</sup>

<sup>1</sup>Department of Physics, Panjab University, Chandigarh 160014, India

<sup>2</sup>Inter University Accelerator Centre, Aruna Asaf Ali Marg, New Delhi 110067, India

<sup>3</sup>Department of Physics, I. K. G. Punjab Technical University, Kapurthala 144603, India

<sup>4</sup>Department of Physics, Kurukshetra University, Kurukshetra 136119, India

The spectra for light charged particles as well as neutrons emitted from mass symmetric heavy-ion induced fusion reactions are found to be anomalous with respect to the standard statistical model calculations. Various conjunctures have been proposed to explain this anomalous behaviour. Fusion hindrance for mass symmetric systems at high excitation energy is one of the conjunctures for explaining such anomalous spectra. Same compound nuclei  $^{80}\text{Sr}$  was populated by two different entrance channels, mass asymmetric channel  $^{16}\text{O}+^{64}\text{Zn}$  (45 MeV, 59 MeV and 89 MeV) and nearly mass symmetric channel,  $^{32}\text{S}+^{48}\text{Ti}$  (85 MeV, 94 MeV and 125 MeV). Data for light particles (p,  $\alpha$  and n) and evaporation residues (ER) were collected in an experiment at IUAC, using the General Purpose Scattering Chamber (GPSC) facility.

For the demonstration of the above effect, evaporation residue gated neutron and charged particle spectra are to be analysed with respect to the statistical model. For ER gating, two multi-wire proportional counters were placed at extremely forward angles ranging from  $2^\circ - 10^\circ$ . Four neutron detectors were kept at  $30^\circ, 60^\circ, 90^\circ$  and  $120^\circ$  for detection of neutrons. For protons and  $\alpha$  particles, CsI detectors were placed having an angular coverage of  $45^\circ - 115^\circ$ . Analysis was performed to obtain neutron and  $\alpha$  spectra (without gating) at all the energies for both the systems. Some of the measured spectra are shown in Fig. 5.1.13.1.

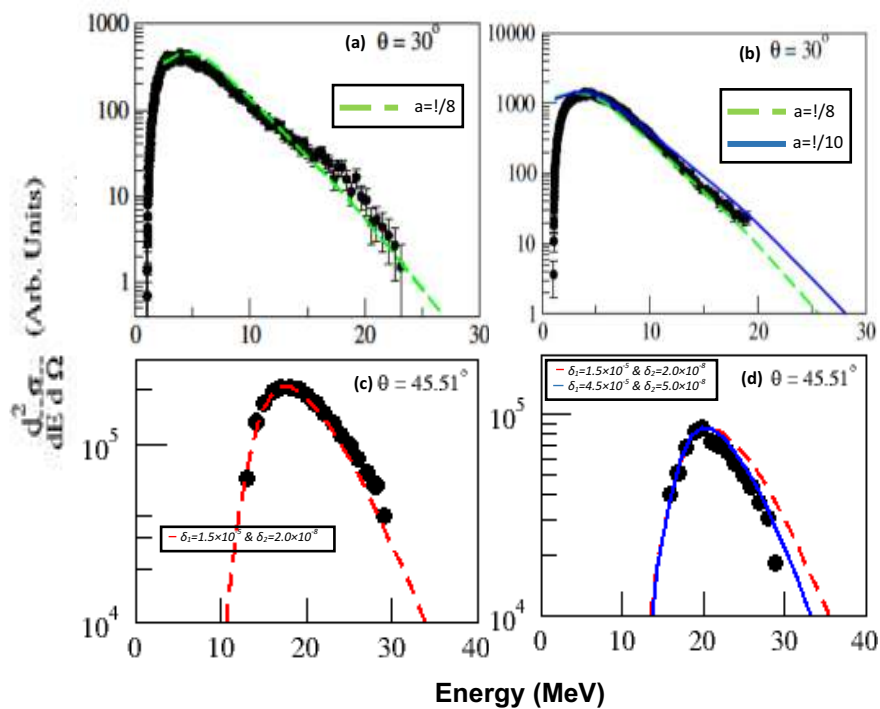


Fig. 5.1.13.1: Black dots represent the experimental spectra. (a) and (b) show neutron spectra for  $^{16}\text{O}+^{64}\text{Zn}$  (89 MeV) and  $^{32}\text{S}+^{48}\text{Ti}$  (125 MeV), respectively. Different level density parameters were used in CASCADE calculations to fit the experimental spectra. (c) and (d) show  $\alpha$ particle energy spectra from CsI detectors for  $^{16}\text{O}+^{64}\text{Zn}$  (89 MeV) and  $^{32}\text{S}+^{48}\text{Ti}$  (125 MeV), respectively. The deformation parameters were varied to fit the experimental spectra.

#### REFERENCES:

- [1] J. Kaur *et al.*, Phys. Rev. C **70**, 017601 (2004).
- [2] A. Kumar *et al.*, Phys. Rev. C **70**, 044607 (2004).
- [3] Maninder Kaur *et al.*, Phys. Rev. C **89**, 034621 (2014).

### 5.1.14 Study of octupole deformation in neutron deficient nuclei ( $A < 120$ ) through lifetime measurements

Anand Pandey<sup>1</sup>, Ravi Bhushan<sup>1</sup>, Aman Rohilla<sup>2</sup>, Bharti Rohila<sup>3</sup>, C. Majumder<sup>4</sup>, Subodh<sup>3</sup>, Kaushik Katre<sup>5</sup>, A. Kumar<sup>3</sup>, I. M. Govil<sup>3</sup>, H. P. Sharma<sup>4</sup>, S. Chakraborty<sup>5</sup>, R.P. Singh<sup>5</sup>, S. Muralithar<sup>5</sup> and S. K. Chamoli<sup>1</sup>

<sup>1</sup>Department of Physics and Astrophysics, University of Delhi, Delhi 110007, India

<sup>2</sup>Institute of Modern Physics, Chinese Academy of Sciences, Lanzhou, China

<sup>3</sup>Department of Physics, Panjab University, Chandigarh 160014, India

<sup>4</sup>Department of Physics, Banaras Hindu University, Varanasi 221005, India

<sup>5</sup>Inter-University Accelerator Centre, Aruna Asaf Ali Marg, New Delhi 110067, India

The nuclei with  $A \sim 120$  ( $50 \leq Z \leq 56$ ) are of considerable interest because of the competing shape driving tendencies of their orbitals occupied by the neutrons and the protons. Due to the presence of both quadrupole and octupole collectivity in the neutron deficient Ba, Cs and Xe nuclei, this mass region has attracted much attention in recent years. For nuclei with  $A < 120$ , due to their closeness to the proton drip line and therefore difficulty in population via fusion evaporation reactions, octupole collectivity has been reported in very few cases e.g. <sup>114,116,117</sup>Xe and <sup>110</sup>Te [1,2]. In these reported cases also, several ambiguities have been observed in the nature of octupole correlations. Like in <sup>110</sup>Te, the measured B(E1) strengths (the most prominent experimental evidence considered for octupole correlations) are found to be in agreement when compared to those in the neutron-rich barium nuclei. However, when compared to <sup>114,116</sup>Xe, the B(E1) values in <sup>110</sup>Te are found to be about an order of magnitude larger, thereby making the  $T_z$  scaling of the dipole moment suggested in Ref. [1] questionable. Also, in case of <sup>114</sup>Xe, the B(E1) value of the  $5^- \rightarrow 6^+$  transition is two orders of magnitude larger than that of  $5^- \rightarrow 4^+$  transition, thus contradicting a simple interpretation based on fixed intrinsic octupole deformation. So, more experiments are needed to systematically investigate whether the octupole phenomenon is common in the  $A \sim 120$  region. With this motivation, recently an experiment was carried out to explore the high spin states in neutron deficient <sup>118</sup>Xe nuclei via lifetime measurement using Doppler shift attenuation method (DSAM) technique at IUAC. High spin states in <sup>118</sup>Xe were populated using the <sup>93</sup>Nb(<sup>28</sup>Si, p2n)<sup>118</sup>Xe fusion evaporation reaction at a beam energy of 115 MeV. The target consisted of uniformly rolled <sup>93</sup>Nb foil of thickness  $\sim 1.28$  mg/cm<sup>2</sup> on an 8 mg/cm<sup>2</sup> thick Pb backing. The de-exciting gamma rays were detected with the Indian National Gamma Array (INGA) [3], consisting of 16 Compton-suppressed Clover detectors, arranged in five rings at angles of 32°, 57°, 90°, 123° and 148° with respect to the beam direction. Data were collected in  $\gamma$ - $\gamma$  coincidence mode for 9 shifts of beam time. The total number of counts acquired in  $\gamma$ - $\gamma$  coincidence were  $6 \times 10^8$ . To optimize yield of <sup>118</sup>Xe, excitation function was measured at 112, 115, 116 and 120 MeV of beam energy. Part of the data is presented in Fig. 5.1.14.1, showing clearly marked gamma energy peaks from various nuclei populated in the reaction. A number of symmetric and asymmetric matrices were constructed by sorting gain matched list mode data. Intensity measurements were done using symmetric matrix in the present work and the results were found to be consistent with previous studies. Spin and parity of the excited states were confirmed using  $R_{\text{DCO}}$  and polarization asymmetry measurements. The anisotropic intensity ratio ( $R_{\text{DCO}}$ ) of two mutually coincident gamma-ray transitions can be measured using the formulae given below:

$$R_{\text{DCO}} = \frac{I_{\gamma_1 \text{ at } 148^\circ \text{ gated with } \gamma_2 \text{ at } 90^\circ}}{I_{\gamma_1 \text{ at } 90^\circ \text{ gated with } \gamma_2 \text{ at } 148^\circ}}$$

To confirm the nature of transition to be electric or magnetic, polarisation asymmetry of the transition is measured using the formulae given below:

$$\Delta_{\text{asymmetry}} = \frac{\alpha(E_\gamma)N_{\perp} - N_{\parallel}}{\alpha(E_\gamma)N_{\perp} + N_{\parallel}}$$

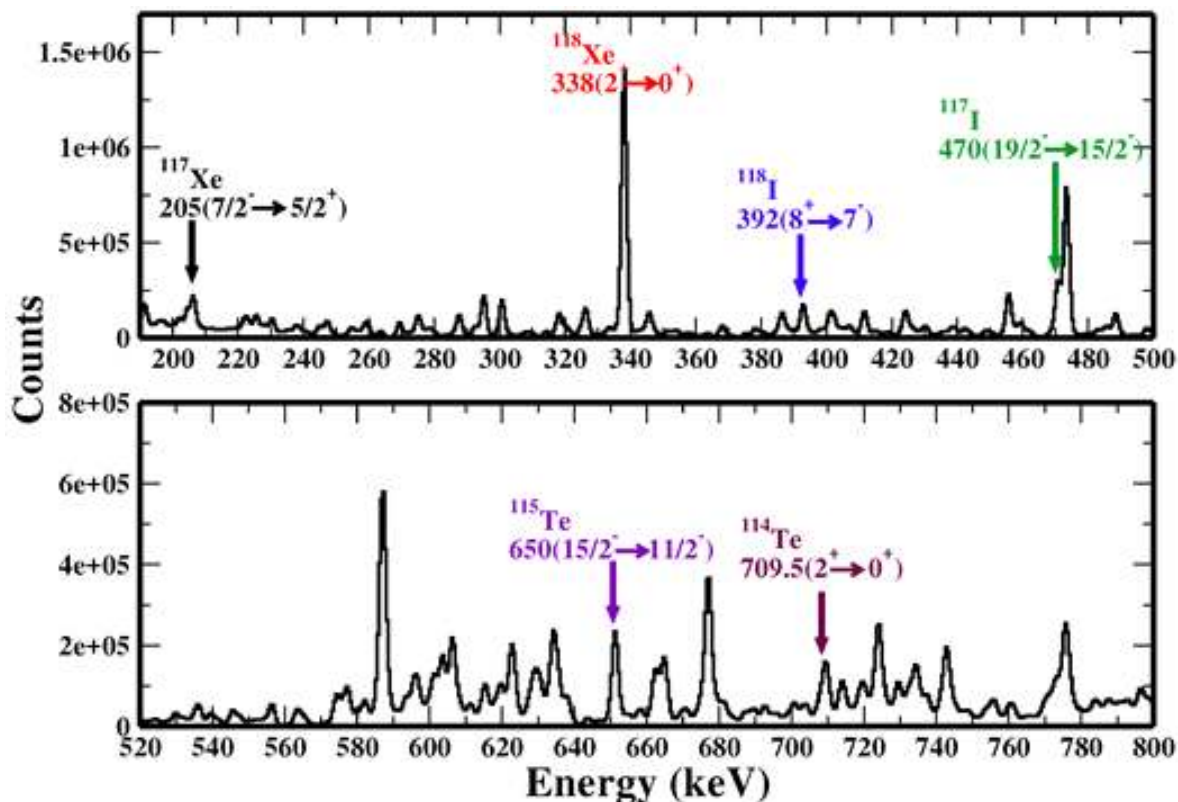


Fig 5.1.14.1: Energy spectrum showing quality of data taken. Most intense gamma peaks from different nuclei populated in the reaction are marked by different colours.

#### REFERENCES:

- [1] S. L. Rugari *et al.*, Phys. Rev. C **48**, 2078 (1993).
- [2] E. S. Paul *et al.*, Phys. Rev. C **50**, R534 (1994).
- [3] S. Muralithar *et al.*, Nucl. Instrum. Methods A **622**, 281 (2010).

#### 5.1.15 Systematic study of fusion-fission dynamics of $^{209}\text{At}$ through fission fragment mass distribution

R. K. Singh<sup>1</sup>, N. L. Singh<sup>1</sup>, S. Mukherjee<sup>1</sup>, Akhil Jhingan<sup>2</sup>, P. Sugathan, K. S. Golda<sup>2</sup>, N. Saneesh<sup>2</sup>, Mohit Kumar<sup>2</sup>, D. Arora<sup>2</sup>, N. K. Joshi<sup>3</sup>, K. Chakraborty<sup>3</sup>, B. K. Nayak<sup>4</sup> and S. Santra<sup>4</sup>

<sup>1</sup>Department of Physic, The M. S. University of Baroda, Vadodara, Gujarat 390002, India

<sup>2</sup>Inter-university Accelerator Centre, Aruna Asaf Ali Marg, New Delhi 110067, India

<sup>3</sup>Department of Physics and Astrophysics, Delhi University, Delhi 110007, India

<sup>4</sup>Nuclear Physics Division, Bhabha Atomic Research Centre, Mumbai 400085, India

Study of fusion-fission dynamics is very important as the formation of heavy or super heavy elements are strongly suppressed not only by equilibrium fission, but also by a non-equilibrium process called quasi-fission (QF) [1]. The entrance channel properties of the reacting systems appear to play a major role in deciding the outcome of the reaction. The role of entrance channel mass asymmetry can be studied by choosing different projectile-target combinations. It is important to understand how deformation and spin of the target/projectile and the charge product ( $Z_p Z_t$ ) affect the reaction dynamics. The variation of mass widths, observed in reactions involving heavy and deformed nuclei, reveals crucial information about the fission dynamics. Admixture of equilibrium fission and quasi-fission is observed which can be explained by the orientation dependent model [2].

Our objective is to study how these factors are affecting the fusion-fission dynamics through the study of fission fragment mass distributions of  $^{209}\text{At}$  populated via two reactions viz.  $^{16}\text{O}+^{193}\text{Ir}$  and  $^{12}\text{C}+^{197}\text{Au}$ . The experiment was carried out at IUAC. Pulsed beams of  $^{16}\text{O}$  and  $^{12}\text{C}$  in the laboratory energy ranges of 75 – 92 MeV and 57 – 77 MeV were bombarded on  $^{193}\text{Ir}$  ( $\approx 80 \mu\text{g}/\text{cm}^2$  on  $22 \mu\text{g}/\text{cm}^2$  carbon backing) and  $^{197}\text{Au}$  ( $\approx 150 \mu\text{g}/\text{cm}^2$  on  $30 \mu\text{g}/\text{cm}^2$  carbon backing) targets, respectively. The coincident fission fragments were detected using two large area ( $16 \times 10 \text{ cm}^2$ ) multi-wire proportional counters (MWPCs), placed at the folding angles on two movable arms inside the General Purpose Scattering Chamber (GPSC). The pressure in the chamber was

$3.4 \times 10^{-6}$  mbar. The detectors were operated with isobutane gas at a pressure of about 3.5 mbar to make them almost transparent to elastic and quasi-elastic events. The time of flight (TOF) of each fragment was recorded with regard to the radio frequency (rf) timing. The target ladder was rotated with respect to the beam direction in order to avoid shadowing either of the two detectors. Data were collected in event mode using FREEDOM [3] acquisition software. Beam monitoring was done by counting the elastically scattered beam particles in two silicon surface barrier detectors placed at  $\pm 10^\circ$  with regard to the beam direction. Analysis of data is in progress.

#### REFERENCES:

- [1] B. B. Back, Phys. Rev. C **31**, 2104 (1985).
- [2] Kavita, K. S. Golda et al., Phys. Rev. C **100**, 024626 (2019).
- [3] B. P. Ajith Kumar, E. T. Subramaniam, K. Singh and R. K. Bhowmik, FREEDOM high-speed DAS, SANAI, Trombay, India (1997).

### 5.1.16 Measurement of transfer cross sections for $^{16}\text{O}+^{144,154}\text{Sm}$ systems

Kavita Rani<sup>1</sup>, B. R. Behera<sup>1</sup>, A. Jhingan<sup>2</sup>, M. Kumar<sup>2</sup>, N. Saneesh<sup>2</sup>, H. Arora<sup>1</sup>, D. Arora<sup>2</sup>, Amit<sup>1</sup>, V. Srivastava<sup>1</sup>, K. S. Golda<sup>2</sup> and P. Sugathan<sup>2</sup>

<sup>1</sup>Department of Physics, Panjab University, Chandigarh 160014, India

<sup>2</sup>Inter-University Accelerator Centre, Aruna Asaf Ali Marg, New Delhi 110067, India

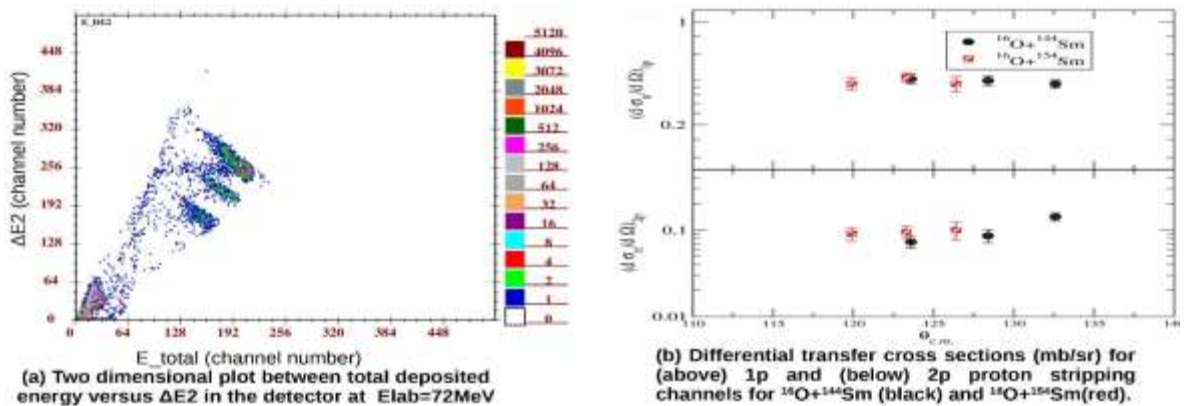


Fig. 5.1.16.1: (a) Two-dimensional plot between total deposited energy versus  $\Delta E2$  at  $E_{\text{lab}} = 72$  MeV.  
(b) Differential transfer cross sections (in mb/sr) for (above) 1p and (below) 2p proton stripping channels for  $^{16}\text{O}+^{144}\text{Sm}$  (black) and  $^{16}\text{O}+^{154}\text{Sm}$  (red).

For measurement of transfer events at two energies i.e.  $E_{\text{lab}} = 72$  MeV (above the barrier) and  $E_{\text{lab}} = 68$  MeV (below the barrier), experiments have been performed in the General Purpose Scattering Chamber (GPSC) at IUAC. Two monitors, placed at  $\pm 10^\circ$  with respect to the beam direction, help beam monitoring and the cross-section normalization. For  $E_{\text{lab}} = 72$  MeV, an MWPC was placed on one of the movable arms for detection of the target-like transfer products whereas on the other arm, an MWPC followed by an Ionization Chamber (IC) [3] was placed for detection of the projectile-like transfer products. Another MWPC (active area  $4 \times 4$  cm<sup>2</sup>), developed at IUAC, was placed at 6 cm from the target as the master start detector to improve the time of flight resolution. Isobutane gas was circulated in the MWPCs at a pressure of 6.5 mbar. For  $E_{\text{lab}} = 68$  MeV, two MWPCs, followed by two hybrid ( $\Delta E$ -E) detectors attached at the back, were placed for detecting the projectile-like particles. Panel (a) of Fig. 5.1.16.1 shows a two-dimensional E- $\Delta E$  spectrum. Transfer cross-sections (in mb/sr) have been obtained for 1p and 2p channels at  $E_{\text{lab}} = 72$  MeV and are shown in panel (b) of Fig. 5.1.16.1. It is observed that measured transfer cross-sections are almost the same for both the systems. This suggests that absence of the expected structure in the QE-BD of  $^{16}\text{O}+^{144}\text{Sm}$  can be attributed to the weakly coupled transfer channels as in case of  $^{16}\text{O}+^{154}\text{Sm}$ . The theoretical analysis for this is under process.

#### REFERENCES:

- [1] H. Timmers *et al.*, Nucl. Phys. A **584**, 190 (1995).
- [2] J. R. Leigh *et al.*, Phys. Rev. C **52**, 3151 (1995).
- [3] A. Jhingan *et al.*, Nucl. Instrum. Methods A **745**, 106 (2014).

### 5.1.17 Fission dynamics and neutron multiplicity measurements populating the compound nucleus $^{234}\text{Cm}$ through $^{28}\text{Si}+^{206}\text{Pb}$

Rakesh Kumar<sup>1</sup>, Vikas<sup>1</sup>, Shruti<sup>2</sup> Amit Kumar<sup>2</sup>, Subodh Yadav<sup>2</sup>, Chetan<sup>2</sup>, A. Kaur<sup>2</sup>, P. Sugathan<sup>3</sup>, K. S. Golda<sup>3</sup>, A. Jhingan<sup>3</sup>, N. Saneesh<sup>3</sup>, Mohit Kumar<sup>3</sup>, Neeraj Kumar<sup>4</sup>, Phurba Sherpa<sup>4</sup>, Shoab Noor<sup>5</sup>, Hardev Singh<sup>1</sup>

<sup>1</sup>Department of Physics, Kurukshetra University, Kurukshetra 136119, India

<sup>2</sup>Department of Physics, Panjab University, Chandigarh 160014, India

<sup>3</sup>Inter-University Accelerator Centre, Aruna Asaf Ali Marg, New Delhi 110067, India

<sup>4</sup>Department of Physics and Astrophysics, University of Delhi, Delhi 110007, India

<sup>5</sup>School of Physics and Materials Science, Thapar Institute of Engineering and Technology, Patiala 147004, India

In recent years, a large number of experimental and theoretical studies have been performed to understand the dynamics of heavy ion induced fusion-fission reactions. Probes like fission fragment mass distribution, multiplicities of neutrons, charged particles, and  $\gamma$ -rays are widely used to understand the fusion-fission (FF) dynamics. [1-3]. The present experiment ( $^{28}\text{Si}+^{206}\text{Pb}$ ) is an effort to study fission dynamics using neutron multiplicity as the probe. The experiment was performed with beam energy in the range of 170 – 210 MeV, provided by the 15UD Pelletron + LINAC of IUAC. The National Array of Neutron Detectors (NAND) facility was used for collecting the neutrons in coincidence with fission fragments. Pulsed beam of  $^{28}\text{Si}$  was bombarded on 400  $\mu\text{g}/\text{cm}^2$  and 800  $\mu\text{g}/\text{cm}^2$  thick  $^{206}\text{Pb}$  target foils to populate the compound nucleus  $^{234}_{96}\text{Cm}$ . Two MWPCs with an active area of  $10 \times 20 \text{ cm}^2$ , placed at folding angles, were used for detection of the fission fragments. The fission detectors were mounted on two movable arms on either side of the beam axis at a distance of 26 cm and 23 cm from the center of the target inside the chamber. Both detectors were operated at 4.0 mbar pressure of iso-butane gas in flow mode. The MWPCs allowed to collect the elastically scattered events, symmetric and asymmetric fragments from the compound system. The fast-timing signals from the anodes of the two MWPCs were used to obtain the fission fragment time of flight (TOF) with respect to the beam pulse. Position information of the fission fragments were obtained from the delay-line readout of the wire-planes. Neutrons emitted during the process of fission were detected in coincidence with the fragments. A fast coincidence between any of the anode signals from MWPCs and the RF pulse was used as the master trigger for list mode data collection. The data were acquired using a VME-based data acquisition system and IUAC-MARS software. Detailed analysis of fragment mass distribution and neutron multiplicity at different excitation energies from the fission of  $^{234}\text{Cm}$  is underway.

#### REFERENCES:

- [1] R. Sandal *et al.*, Phys. Rev. C **87**, 014604 (2013).
- [2] M. Thakur *et al.*, Eur. Phys. J. A **53**, 133 (2017).
- [3] Neeraj Kumar *et al.*, Phys. Lett. B **814**, 136062 (2021).

### 5.1.18 Breakup study of weakly bounded projectile $^7\text{Li}$ with $^{92,100}\text{Mo}$

C. Joshi<sup>1,2</sup>, R. K. Singh<sup>1</sup>, N. L. Singh<sup>1</sup>, H. Kumawat<sup>2</sup>, Kavita Rani<sup>3</sup>, A. Parihari<sup>4</sup>, J. Acharya<sup>1</sup>, G. Kaur<sup>4</sup>, N. Saneesh<sup>4</sup>, Mohit Kumar<sup>4</sup>, K.S. Golda<sup>4</sup>, A. Jhingan<sup>4</sup> and P. Sugathan<sup>4</sup>

<sup>1</sup>Department of Physics, The M.S. University of Baroda, Vadodara 390002, India

<sup>2</sup>Nuclear Physics Division, Bhabha Atomic Research Centre, Mumbai 400085, India

<sup>3</sup>Department of Physics, Panjab University, Chandigarh 160014, India

<sup>4</sup>Inter-University Accelerator Centre, Aruna Asaf Ali Marg, New Delhi 110067, India

The experiment was performed in the General Purpose Scattering Chamber (GPSC) facility of IUAC. We fabricated around 20 target foils of each isotope  $^{92,100}\text{Mo}$  of thickness 217  $\mu\text{g}/\text{cm}^2$  and 305  $\mu\text{g}/\text{cm}^2$ , respectively [1]. Beams of  $^7\text{Li}$  were used ranging in energy from 15 to 35 MeV. The beam current was in the range of 2 to 5 pA. Silicon Surface barrier detectors were mounted on the two rotatable arms to cover angles  $17^\circ$  to  $168^\circ$ . A High Purity Germanium (HPGe) detector was used to record gamma transitions between different levels of the populated nuclei.

The optical model analysis of elastic scattering differential cross section data has been performed. The best fits of angular distribution for the reaction  $^7\text{Li}+^{100}\text{Mo}$  at different energies are shown in Fig. 5.1.18.1. The analysis for elastic scattering is done by two different optical potentials, viz. Wood-Saxon and Sao-Paulo potentials. Similar line of analysis has also been carried out for the other isotope  $^{92}\text{Mo}$ . The systematics of cross sections for different targets along with  $^{92,100}\text{Mo}$  are presented in Fig. 5.1.18.2. The dispersion relation for energy dependence of potential near the Coulomb barrier has also been calculated for both the systems.

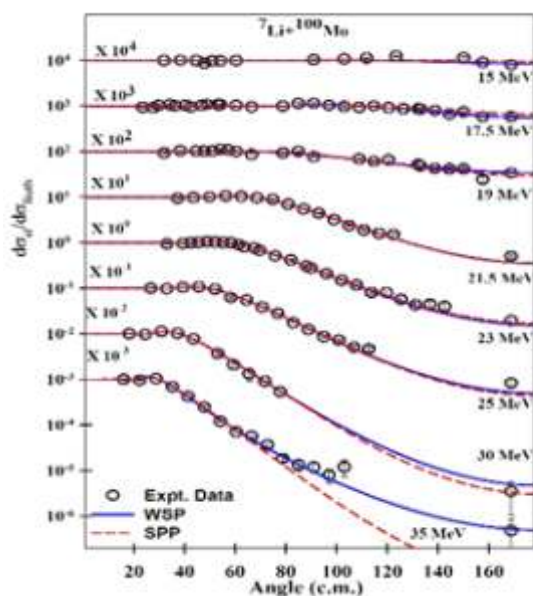
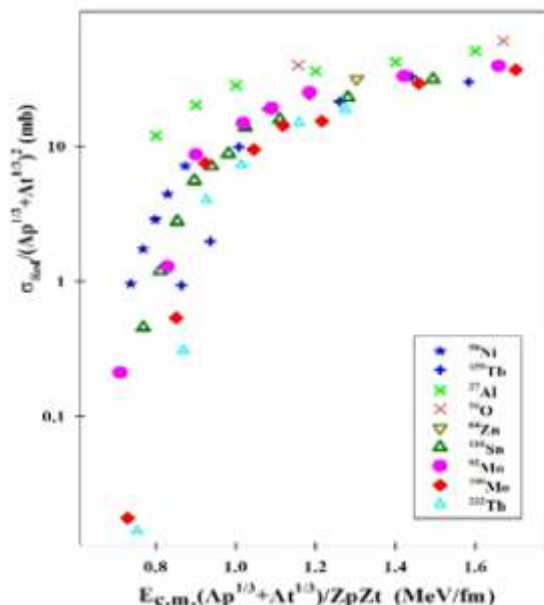
Fig 5.1.18.1: Angular distribution for the reaction  ${}^7\text{Li}+{}^{100}\text{Mo}$ .

Fig 5.1.18.2: Systematics of cross sections for different targets.

Other theoretical calculations for describing breakup details of weakly bound projectile for this system as well as analysis of data for  ${}^6\text{Li}$ -induced reactions are under progress.

#### REFERENCES:

- [1] C. Joshi *et al.*, Proc. DAE-BRNS Symp. Nucl. Phys. **63**, 1210 (2018).

### 5.1.19 Measurement of evaporation residue excitation functions for the reactions ${}^{12}\text{C}+{}^{182,184,186}\text{W}$

S. Sanila<sup>1</sup>, A. M. Vinodkumar<sup>1</sup>, B. R. S. Babu<sup>1</sup>, N. Madhavan<sup>2</sup>, S. Nath<sup>2</sup>, J. Gehlot<sup>2</sup>, Rohan Biswas<sup>2</sup>, Chandra Kumar<sup>2</sup>, Gonika<sup>2</sup>, Anjali Rani<sup>3</sup>, A. Parihari<sup>3</sup>, D. Viswakarma<sup>3</sup>, Shoaib Noor<sup>4</sup> and E. Prasad<sup>5</sup>

<sup>1</sup>Department of Physics, University of Calicut, Calicut 673635, India

<sup>2</sup>Nuclear Physics Group, Inter-University Accelerator Centre, Aruna Asaf Ali Marg, New Delhi 110067, India

<sup>3</sup>Department of Physics and Astrophysics, University of Delhi, Delhi 110007, India

<sup>4</sup>School of Physics and Materials Science, Thapar Institute of Engineering and Technology, Patiala 147004, India

<sup>5</sup>Department of Physics, School of Mathematical and Physical Sciences, Central University of Kerala, Kasaragod 671328, India

The study of heavy ion reactions around the Coulomb barrier continues to be of considerable interest from different aspects [1, 2]. Rajagopalan *et al.* [3] studied twelve reactions that produce the compound system  ${}^{194}\text{Hg}$  at excitation energies of 57-195 MeV. They found that the non-equilibrium mechanisms affect the evaporation residue (ER) production, either incomplete fusion directly feeds the ER or non-equilibrium fission competes with ER formation. Hui *et al.* [4] measured ER excitation function and  $\gamma$ -ray multiplicity in coincidence with ERs for the reaction  ${}^{19}\text{F}+{}^{175}\text{Lu}$  forming  ${}^{194}\text{Hg}$  for studying the spin dependence of dissipation effects in fission. Their studies confirm that there is no onset of dissipation in the pre-saddle region of the fission process.

To study ERs for the reactions forming  ${}^{194}\text{Hg}$ ,  ${}^{196}\text{Hg}$  and  ${}^{198}\text{Hg}$  compound nuclei, we have measured evaporation residue cross sections for  ${}^{12}\text{C}+{}^{182,184,186}\text{W}$  systems at near and above the Coulomb barrier using the Heavy Ion Reaction Analyzer (HIRA) [5]. The experiment was carried out using  ${}^{12}\text{C}$  beam with energy in the range of 52 – 84 MeV, provided by the 15UD Pelletron Accelerator Facility at IUAC. Pulse separation of the beam was 8  $\mu\text{s}$  for 52 – 58 MeV, 4  $\mu\text{s}$  for 60 – 72 MeV and 500 ns for 76 – 84 MeV. Targets of  ${}^{182,184,186}\text{W}$  with thickness 70  $\mu\text{g}/\text{cm}^2$ , 100  $\mu\text{g}/\text{cm}^2$  and 100  $\mu\text{g}/\text{cm}^2$  on carbon backing of 20  $\mu\text{g}/\text{cm}^2$ , 35  $\mu\text{g}/\text{cm}^2$  and 25  $\mu\text{g}/\text{cm}^2$ , respectively were bombarded. At the focal plane of the HIRA, a two-dimensional position-sensitive multi-wire proportional counter (MWPC) with an active area of 15 cm  $\times$  5 cm was used to detect the ERs. A time of flight was set up between the anode pulse of MWPC and the RF signal, to separate the beam-like particles from ERs. The preliminary ER cross-sections for  ${}^{12}\text{C}+{}^{182,184,186}\text{W}$  reactions are shown in Fig. 5.1.19.1. Further analysis is in progress.

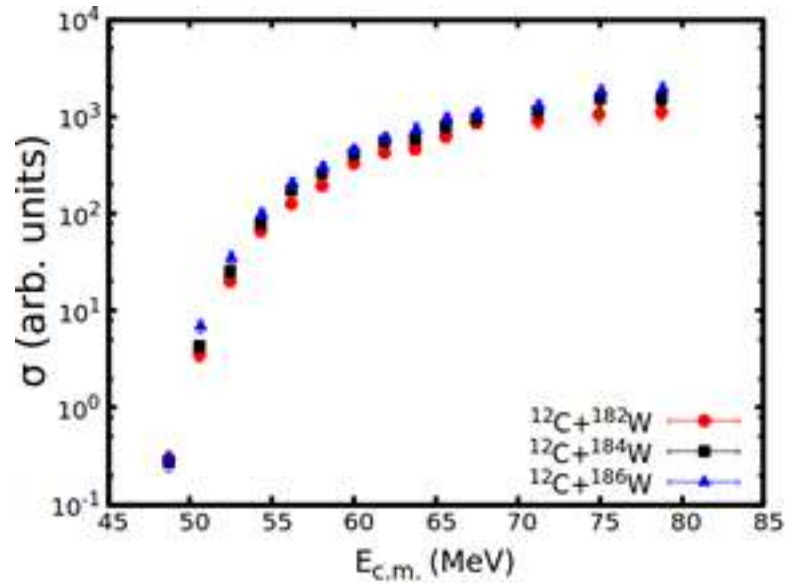


Fig 5.1.19.1: Experimental fusion excitation function for  $^{12}\text{C}+^{182,184,186}\text{W}$  systems.

#### REFERENCES:

- [1] Amit Chauhan, Rinku Prajapat, Gayatri Sarkar, Moumita Maiti *et al.*, Phys. Rev. C **102**, 064606 (2020).
- [2] P. Jisha, A. M. Vinodkumar, B. R. S. Babu, S. Nath *et al.*, Phys. Rev. C **101**, 024611 (2020).
- [3] M. Rajagopalan, D. Logan, Jane. Ball, Morton Kaplan *et al.*, Phys. Rev. C **25**, 2417 (1982).
- [4] S. K. Hui, C. R. Bhuinya, A. K. Ganguly, N. Madhavan *et al.*, Phys. Rev. C **62**, 054604 (2000).
- [5] A. K. Sinha, N. Madhavan, J. J. Das, P. Sugathan *et al.*, Nucl. Instrum. Methods A **339**, 543 (1994).

## 5.2 MATERIALS SCIENCE

Ambuj Tripathi

The materials science facilities continue to support research programmes of a large number of users from different universities and institutions. This year there were a total of 18 user experiments spread over 64 shifts and were performed without any major beam time loss due to facility break down in materials science beamlines. These included 10 BTA runs spread over 34 shifts, associated with students' Ph.D. programmes. Compilation of reports/ SOPs for digitization also continued this year, specially during lockdown period. The data base of users was updated to identify and assist scholars/ users urgently requiring beamtimes. Efforts were made to complete scholar's project during Covid restrictions and 11 such experiments were completed with help of IUAC collaborators, many by getting the samples from users who could not travel due to restrictions. Though the swift heavy ion (SHI) irradiation and related experiments mostly utilize irradiation chamber in the materials science beamlines in beamhall-I, 1 experiments of 3 shifts requiring low fluence irradiation were performed in GPSC beamline. Besides irradiation facilities, materials science group is also providing many materials synthesis and characterization facilities and this year limited off line characterizations were undertaken keeping Covid protocols in place. The materials science research programmes are being carried out in a wide range of energies varying from tens of keV to hundreds of MeV and the complete list of publications is given in section 6. The highlights of the activities are also available in Materials Science group webpage.

This year there were many interesting results in the various areas of research including those on radiation stability, band gap tuning, epitaxial recrystallization, sequential implantation/irradiation, nanostructuring, nanocomposites and applications, novel phase formations, etc. Special emphasis is given to *in-situ*/ on-line measurements and many such experiments were undertaken. The electrical device characteristics of Ni/ $\beta$ -Ga<sub>2</sub>O<sub>3</sub> vertical Schottky barrier diodes (SBDs) were measured *in-situ* during the irradiation of 120 MeV Ag<sup>7+</sup> ions. The devices exhibit SHI irradiation-induced degradation at the ion fluences upto  $1 \times 10^{12}$  ions/cm<sup>2</sup>. Sequential single ion irradiations were performed using 300 keV Ar and 100 MeV Ag in 4H-SiC to invoke swift heavy ion (SHI) beam-induced epitaxial recrystallization with different degrees of pre-damaged conditions and the evolution of the depth distribution of damage was simulated using the Dechanneling In Crystals And Defect Analysis (DICADA) code. It is shown that SHI-induced thermal spike alone is enough to promote evaporation of interstitials and vacancy-interstitial recombination allowing temperature-independent recovery. To study the effects of the swift heavy ion (SHI) irradiation on the structural, physical, and chemical properties of the zirconolite compositions, samples, 90 MeV I<sup>+</sup> ion irradiation induced structural changes in the matrices are studied using XRD measurements and show amorphization. The basic aim of the study being investigation of loading capacity of tri- and tetravalent actinides wastes. Nanochannels were created in poly (vinylidene fluoride) and its nanohybrid with nanodimensional clay using 140 MeV Ag and 80 MeV Li followed by chemical etching and subsequent functionalization. A membrane electrode assembly has been fabricated to construct a complete fuel cell exhibiting superior power generation with power density of 45 mW/cm<sup>2</sup>. Reliable depth profiling for 80 keV Gold ions implanted in silicon substrates studies using combined X-ray reflectivity (XRR)- Grazing incidence X-ray fluorescence (GIXRF) measurements showed inconsistency with Secondary ion mass Spectrometry (SIMS). Manganite based LCMO/LSMO thin films were irradiated with Ag ions at fluences upto  $1 \times 10^{13}$  ions/cm<sup>2</sup> and it was shown that strain between the films and substrates is an important tool to control the anisotropic magnetodielectric and magnetoelectric parameters and properties. Electrospun TiO<sub>2</sub> nanofibres incorporated photoanodes were implanted using 120 keV Ag ions for the fabrication of DSSCs. 100 MeV Ni and Si ion irradiation effects on structural and optical properties of PVA-Ni (NO<sub>3</sub>)<sub>2</sub> Polymeric film were studied and it is shown that the formation of conjugated bonds results in the

decrease of optical band gap. RBS/C studies are performed on Si(100) and Ge(100) pre-bombarded with 100 keV Ar<sup>+</sup> ion beam in the ion fluences upto  $9 \times 10^{17}$  ions/cm<sup>2</sup> incident at  $\theta \sim 60^\circ$ . Defects Assisted Structural and Electrical Properties of Ar Irradiated TiO<sub>2</sub>/SrTiO<sub>3</sub> bilayers are studied and it is proposed that irradiation induced oxygen deficient TiO<sub>2</sub> layer extracts oxygen from STO layer, thus generating a conductive layer near surface layers and subsequently leading to increased conductivity. 26 keV N ions from Tabletop accelerator were implanted to control magnetic and electrical properties of Fe<sub>3</sub>O<sub>4</sub> thin and an increment in carrier concentration and reduction in resistivity suggesting that Fe<sup>2+</sup> ions at octahedral sites increases leading to the improvement in the magnetic properties. The application of 125 MeV Ag ions induced electronic excitations in tuning the bandgap of SrTiO<sub>3</sub> films in the range of 2.93-3.78 eV and their correlation with the synchrotron-based X-ray diffraction pattern and X-ray absorption spectra (XAS) is undertaken. Electrical transport study and band gap estimation of 100 keV Ge ion implanted CoSb<sub>3</sub> Skutterudite thin films was undertaken. The bandgap value of implanted samples is lower than that of pristine one as Ge ion introduces donor level in the bandgap of skutterudite and modifies the band structure. The formation of n-type ultra-nanocrystalline diamond exhibiting high electrical conductivity,  $\sigma_{RT} \sim 10^4 \Omega^{-1} \text{m}^{-1}$  by 100 keV phosphorus ion implantation at fluences upto  $10^{17}$  ions/cm<sup>2</sup> was demonstrated where nonlinear Hall effect reveals the signature of two band conduction mechanisms through impurity and conduction bands. The evolution of optical intense blue-green emission in 100 keV nitrogen (N) ion implanted SrTiO<sub>3</sub> (STO) thin films has been investigated by XRD, PL and XANES and it is shown that N ion implanted STO can be a good photoluminescent material exhibiting a variety of emissions through bound states of O vacancies and implanted N ions. Room temperature ferromagnetism in Cluster free films of vertically aligned Fe-doped ZnO nanorods have been developed by controlled doping of F ion-implantation and subsequent dissolution of metal clusters into the ZnO matrix by 200 MeV silver ion beam. It is shown that the dispersion of implanted Fe and lattice defects such as oxygen vacancies are source of ferromagnetism in nanorods. MoS<sub>2</sub>- PVA nanocomposite films have been irradiated with 80 MeV Carbon, 100 MeV Silicon, and 120 Silver energetic beams to achieve enhanced conductivity and have been exploited as an electrode material for asymmetric supercapacitor. Apart from the studies on swift heavy ion irradiation, a large number users have published their work related to effects of low energy ion implantations and gamma irradiations in various physical properties of materials.

The biennial SHIMEC/IBMEC conference series being organized by IUAC continued in online mode as 6<sup>th</sup> International Conference on Ion Beams in Materials Engineering and Characterization on Dec 8-11, 2021. The conference had 19 invited speakers, (including 11 from Germany, France, Russia, USA, Japan and Australia), 25 Oral presentations (including 3 from Germany, Brazil, Taiwan) and 85 poster presentations. The inaugural talk was given by Dr RK Kotnala. The conference was preceded by an International School on Ion Beams in Materials Science in online mode on Dec 1-5, 2020. The school had 120 participants and 14 resource persons including 7 from Germany, Spain, Singapore, France and Japan.

### 5.2.1 Ion irradiation effects on GaN and TiO<sub>2</sub> substrates for optoelectronic devices applications

Anand Pandey<sup>1</sup>, Fouran Singh<sup>2</sup>, Govind Gupta<sup>3</sup>, D. Kanjilal<sup>2</sup> and Lokendra Kumar<sup>1</sup>

<sup>1</sup>Physics Department, University of Allahabad, Prayagraj, 211002, India.

<sup>2</sup>Inter University Accelerator Center, Aruna Asaf Ali Marg, New Delhi, 110 067, India.

<sup>3</sup>CSIR-National Physical Laboratory (NPL), Dr. K. S. Krishnan Marg, New Delhi, 110012, India.

Gallium Nitride (GaN) and titanium dioxide (TiO<sub>2</sub>) have many applications in the fabrication of optoelectronic devices, sensors, photodetectors, high temperature and power devices –. Extensive research has been carried out for understanding the phenomena of various defects present in GaN and TiO<sub>2</sub> and the role of these defects in

optical and electrical properties of semiconductors. GaN and TiO<sub>2</sub> are well known wide band gap semiconductors. The defects in GaN create additional levels and act as donors and acceptors which plays a crucial role in deciding the optoelectronics features of GaN films. Similarly, TiO<sub>2</sub> films fabricated by simple solution process contains many surface defects, oxygen vacancy which alternatively resultants the poor performance of devices –. Therefore, it is needed to passivate these defects. Ion irradiation is one such method which can passivate the effects by offering crystallization or amorphization depends on the irradiation . In this work, ion irradiation technique is used to passivate these defects and the effects of ion irradiation on GaN and TiO<sub>2</sub> films for possible optoelectronic device applications will be studied.

In order to investigate the ion irradiation effects on GaN films, GaN films were fabricated by MOCVD method on Si (111), Si (110) and Al<sub>2</sub>O<sub>3</sub> substrates at CSIR-National Physical Laboratory (NPL), New Delhi. Whereas, TiO<sub>2</sub> films were synthesized by sol gel method onto fluorine doped tin oxide (FTO) substrates (*for details see,-*). The GaN films fabricated onto Si (110) and Si (111) substrates were further irradiated using 15 UD Pelletron tandem accelerator at Inter University Accelerator Centre (IUAC), New Delhi with 100 MeV Si ions at three different ion fluences i. e.  $1 \times 10^{13}$  ions/cm<sup>2</sup>,  $5 \times 10^{13}$  ions/cm<sup>2</sup> and  $1 \times 10^{14}$  ions/cm<sup>2</sup> with current of 1pA (particle nano-ampere). All the films were fixed to the target ladder placed inside the high vacuum ( $\sim 10^{-6}$  torr) chamber during irradiation. Irradiation was performed in the direction perpendicular to the sample surface. The ion beam was focused to a spot of approximately 1 mm diameter and then scanned over an area of  $1 \times 1$  cm<sup>2</sup> using magnetic scanner to cover the complete sample surface for uniform irradiation. While the GaN substrates fabricated onto Al<sub>2</sub>O<sub>3</sub> substrates and TiO<sub>2</sub> films synthesized via simple sol gel technique were irradiated with 100 MeV Au ions at three different ion fluences i.e.  $1 \times 10^{11}$  ions/cm<sup>2</sup>,  $1 \times 10^{12}$  ions/cm<sup>2</sup> and  $1 \times 10^{13}$  ions/cm<sup>2</sup> using same parameters as above. To investigate the effects on optical changes because of ion irradiation, we have carried out the FTIR measurements on GaN films and UV-Vis transmittance on TiO<sub>2</sub> films at IUAC, New Delhi. To study the effects on structural, optical, electrical and morphological properties of the irradiation on GaN and TiO<sub>2</sub> films other measurements and analysis are under process.

#### REFERENCES:

- [1] Neha Aggarwal and Govind Gupta J. Mater. Chem. C. 8 (2020) 12348–12354.
- [2] C. Singha, S. Sen, A. Das, A. Saha, P. Pramanik, S. Bera, R. Mukhopadhyay, A. Bhattacharyya, Thin Solid Films. (2020) 138216.
- [3] A. Mutlu, M. Can and C. Tozlu, Thin Solid Films. 685 (2019) 88–96.
- [4] V. Kumar, V. Chauhan, J. Ram, R. Gupta, S. Kumar, P. Chaudhary, B.C. Yadav, S. Ojha, I. Sulania and R. Kumar, Surf. Coatings Technol. 392 (2020).
- [5] D.K. Chaudhary, P. Kumar and L. Kumar, Chem. Phys. Lett. 685 (2017) 210–216

### 5.2.2 Structural Response of Ce & Y-doped Zirconolite upon Swift Heavy Ion Irradiation

Rajveer Kaur<sup>1</sup>, M. Gupta<sup>1,2</sup>, P. K. Kulriya<sup>3</sup>, and S. S. Ghumman<sup>1</sup>

<sup>1</sup>Sant Longowal Institute of Engineering & Technology, Longowal 148106 Punjab, India

<sup>2</sup>Department of Physics, Chandigarh University, Mohali, Punjab 140301, India

<sup>3</sup>School of Physical Sciences, Jawaharlal Nehru University, New Delhi 110067, India

In order to minimize the potential long-term effect of HLWs, investigations are in progress through their immobilization in specific host matrices such as ceramics which are more stable and durable than nuclear glasses [1]. Among various ceramics, zirconolite has been proven to be a good candidate due to their complex layered structure, high radiation and thermal stability under the effects of  $\alpha$ -decay events [2-3]. To investigate loading capacity of tri- and tetravalent actinides wastes, the most traditional approach is the doping using non-radioactive lanthanides (Y & Ce) as actinides surrogates. And the swift heavy ion irradiation has been

performed to understand its radiation tolerance and long-term stability under the effect of alpha decay events. For said purpose, samples were prepared by solid state reaction method with 20% doping concentration of dopants. The prepared samples were found to be almost single phase 2M-zirconolite as characterized through XRD and Raman measurements [4]. The surface morphology and chemical environment of the zirconolite composition were elucidated by SEM, EDS and XPS techniques. It was concluded that the zirconolite can easily accommodate tri- and tetravalent wastes with its 20% concentration and retains its structural integrity [4].

To study the effects of the swift heavy ion (SHI) irradiation on the structural, physical, and chemical properties of the zirconolite compositions, samples were irradiated using 15 UD Pelletron tandem accelerator at Inter University Accelerator Centre (IUAC), New Delhi with  $90 \text{ MeV } \text{I}^+$  ion at room temperature. To investigate the structural changes in the matrices, we have carried out the XRD measurements of the irradiated samples at room temperature at IUAC, New Delhi. At room temperature, all the samples have been observed to undergo amorphization which is confirmed through disappearance of characteristic x-ray diffraction peaks and appearance of broad diffuse scattering bands. Other measurements and analysis are under process.

#### REFERENCES:

- [1] Lee, W. E., Ojovan, M. I., Stennett, M. C., & Hyatt, N. C. 'Immobilisation of radioactive waste in glasses, glass composite materials and ceramics', *Adv Appl Ceram*, 105(1), 3-12, 2006
- [2] Vance, E. R., Ball, C. J., Day, R. A., Smith, K. L., Blackford, M. G., Begg, B. D., & Angel, P. J.: 'Actinide and rare earth incorporation into zirconolite', *J Alloys Compd.*, 213, 406-409, 1994
- [3] Ringwood AE, Kesson SE, Ware NG, Hibberson W, Major A.: 'Immobilization of high level nuclear reactor wastes in SYNROC', *Nature*, 278:219, 1979
- [4] Kaur, R., Gupta, M., Kulriya, P. K., & Ghumman, S. S.: 'Phase analysis and reduction behaviour of Ce dopant in zirconolite', *J Radioanal Nucl Chem*, 1-10, 2019.
- [5] M. Nadeem, Wasi Khan, Shakeel Khan, Shahid Husain and Azizurrahman Ansari, *J. Appl. Phys.* 124 (2018) 164105.

### 5.2.3 Swift heavy ion induced damage recovery in pre-damaged 4H-SiC

Anusmita Chakravorty and D. Kabiraj

*Inter-University Accelerator Centre, Aruna Asaf Ali Marg, New Delhi 110067, India.*

An ultrafast thermal spike within a time interval of a few pico-seconds generated by intense ionizing energy deposited using 100 MeV Ag ions is utilized to study the atomistic details of damage recovery in 300 keV damaged 4H-SiC [1]. Sequential single ion irradiations were performed using 300 keV Ar and 100 MeV Ag in 4H-SiC to invoke swift heavy ion (SHI) beam-induced epitaxial recrystallization in samples with different degrees of pre-damaged conditions. Low energy irradiations were performed at various fluences ( $\text{ions}/\text{cm}^2$ ) utilizing the low energy ion beam facility (LEIBF) and high energy irradiations were performed at room temp and  $\sim 80 \text{ K}$  using the 15-UD Pelletron accelerator at the Inter-University Accelerator Centre (IUAC) in New Delhi, India. The evolution of structural and chemical modifications resulting from irradiation with energetic ions was studied as a function of fluence by Channeling-Rutherford backscattering spectrometry (C-RBS), Raman spectroscopy and high-resolution X-ray photoelectron spectroscopy (H-XPS). C-RBS gives non-destructive access to the long-range structural changes in crystallinity whereas Raman spectroscopy helps to probe the modifications in short-range local arrangements of atoms. Further, the material chemistry is probed using H-XPS and Raman analysis. To understand the evolution of the depth distribution of damage (i.e.,  $f_d$  versus depth) the simulation was performed on C-RBS data using the Dechanneling In Crystals And Defect Analysis (DICADA) code [2]. The Multi-Step Damage Accumulation (MSDA) model was used to investigate the disorder build-up kinetics [3]. The MSDA model is based on the supposition that the disorder build-up progresses through successive multi-step structural modifications with each step explained via direct impact mechanism. The mechanism of recovery due to SHI is explained in terms of the inelastic thermal spike model (i-TSM) [4]. The i-TSM is applied for determining the radial and temporal distribution of the lattice temperature resulting from a single ion passing through the target material. Although the ionizing events accompanying SHI irradiation in pre-damaged 4H-SiC single crystals allow initial structural damage reduction, the chemical disordering persists. In partially damaged crystals, defects exist in the form of isolated amorphous pockets surrounded by damaged crystalline zones acting as a seed for recrystallization. The SHI-induced thermal spike alone is enough to promote evaporation of interstitials and vacancy-interstitial recombination allowing the recovery to become temperature-independent. The absence of an amorphous-crystalline interface and inefficient trapping of the continuous amorphous regions within the thermal spike impedes recrystallization for a heavily damaged region. Besides, the damage build-up kinetics

establish 0.3 displacements per atom (dpa) as the threshold for the onset of amorphization in 4H-SiC. This disorder value strongly influences the swift heavy ion (SHI) induced annealing of the crystals by significantly reducing the recovery efficiency for higher damage levels. For crystals with a higher pre-damage, the recovery, and atomic replacements under SHI-induced thermal spike exhibit dependence on the irradiation temperature. This is attributed to the duration of exposure, the inability of a thermal spike to anneal out amorphous layers completely, the lowered value of lattice thermal conductivity, and the insufficiency of the low temperature (80 K) to overcome certain defect recovery barriers. (see Ref. 1 and references therein).

#### REFERENCES:

- [1] Anusmita Chakravorty, Budhi Singh, Hemant Jatav, Sunil Ojha, Jaspreet Singh, D. Kanjilal, and D. Kabiraj, *J. Appl. Phys.* **128**, 165901 (2020).
- [2] K. Gärtner, *Nucl. Instrum. Methods Phys. Res. Sect. B* **227**, 522 (2005).
- [3] Jacek Jagielski, Lionel Thomé, *Appl Phys A* **97**, 147–155 (2009).
- [4] M. Toulemonde, Ch. Dufour, A. Meftah, and E. Paumier, *Nucl. Instrum. Methods Phys. Res. Sect. B* **166**, 903 (2000).

### 5.2.4 Unary doping effect of A<sup>2+</sup> (A = Zn, Co, Ni) on the structural, electrical and magnetic properties of substituted iron oxide nanostructures

Mubashir Qayoom<sup>1</sup>, Ruqiya Bhat<sup>1</sup>, K. Asokan<sup>2</sup>, M.A. Shah<sup>3</sup>, Ghulam Nabi Dar<sup>1\*</sup>

<sup>1</sup>*Nanophysics Laboratory, Department of Physics, University of Kashmir, Srinagar, India*

<sup>2</sup>*Material Science Division, Inter-University Accelerator Centre, New Delhi 110067, India*

<sup>3</sup>*Nanoscience Laboratory, Department of Physics, NIT, Srinagar 190006, India*

Pure and unary doped iron oxide nanostructures (NSs) were synthesized by hexamethylenetetramine (HMTA)-assisted hydrothermal method [for details refer to *J Mater Sci: Mater Electron* **31**, 8268–8282 (2020)]. The presence of micro-strain was well analyzed and estimated by Williamson–Hall (uniform deformation model) and size–strain analysis using X-ray diffraction peak broadening. The analysis confirmed that all prepared samples exhibited a positive slope which enumerated the presence of tensile micro-strain in all samples. The conductivity of the sample depicted an increasing trend with temperature in all samples which indicated their semiconducting behaviour. Further, it was observed that ZnFe<sub>2</sub>O<sub>4</sub> NSs exhibited super-paramagnetic behaviour, while CoFe<sub>2</sub>O<sub>4</sub> NSs exhibited ferromagnetic behaviour with a high coercivity of 1890 Oe and magnetic anisotropy constant approximately  $1.35 \times 10^5$  emu Oe/g. High saturation magnetization, high dielectric constant, low electrical conductivity and low dielectric loss depicted the potential usage of synthesized ferrite nanostructures (FNSs) for microwave devices.

It was noticed that the dielectric constant of the studied systems evidences dielectric dispersion, which signified that the dielectric constant decreased with the increase in frequency. The dc conductivity for pure and unary doped iron oxide samples was noticed low which suggests that the dominant conduction mechanism is conduction by hopping in localized states. Higher saturation magnetization and other magnetic parameters were observed, which makes them useful for recording media and non-reciprocal microwave devices, e.g. circulators, phase shifters and antennas and in the designing of ferromagnetic amplifiers for microwave signals.

In order to investigate the influence of swift heavy ion irradiation on the structural, topographical, optical and magnetic properties of pure and metal doped iron oxide thin films, we have deposited the thin films of pure and cobalt, zinc and nickel doped iron oxide thin films on SiO<sub>2</sub>/Si (100) substrate by using pulsed laser deposition technique at Material science group, IIT Kanpur. The distance between the substrate and target was adjusted at 5 cm and the laser energy during the deposition was 200 mJ with repetition rate of the target as 8 Hz. The oxygen partial pressure and substrate temperature was optimized to 200 mTorr and 450°C respectively for all thin films. After phase analysis the films were irradiated using 15 UD Pelletron tandem accelerator at Inter University Accelerator Centre (IUAC), New Delhi with 100 MeV Ag<sup>9+</sup> ions at three different ion fluences i.e.  $5 \times 10^{11}$  ions/cm<sup>2</sup>,  $5 \times 10^{12}$  ions/cm<sup>2</sup> and  $1 \times 10^{13}$  ions/cm<sup>2</sup>. with current of 1 pA (particle nanoampere). Irradiation was performed in the direction perpendicular to the sample surface. The ion beam was focused to a spot of approximately 1 mm diameter and then scanned over an area of  $1 \times 1$  cm<sup>2</sup> using magnetic scanner to cover the complete sample surface for uniform irradiation. After irradiation we have investigated the thin films by GIXRD, AFM, UV-DRS, VSM and RBS and the analysis are under process.

## REFERENCES:

- [1] Qayoom, M., Bhat, R., Asokan, K. *et al.* Unary doping effect of A<sup>2+</sup> (A = Zn, Co, Ni) on the structural, electrical and magnetic properties of substituted iron oxide nanostructures. *J Mater Sci: Mater Electron* **31**, 8268–8282 (2020). <https://doi.org/10.1007/s10854-020-03362-2>

## 5.2.5 Fabrication of the porous polymeric membrane using Accelerator for fuel cell and radionuclide sensing

Om Prakash<sup>1</sup>, Saif A. Khan<sup>2</sup> and Pralay Maiti<sup>1</sup>

<sup>1</sup>School of Materials Science and Technology, Indian Institute of Technology (BHU), Varanasi 221 005, India

<sup>2</sup>Inter University Accelerator Centre, Aruna Asaf Ali Marg, New Delhi 110 067, India

Nanochannels were created in poly (vinylidene fluoride) and its nanohybrid with nanodimensional clay using swift heavy ions (SHI) (Ag<sup>11</sup> 140 MeV and Li<sup>+</sup> 80 MeV) followed by chemical etching and subsequent functionalization. The latent tracks in pure polymer and nanohybrid were generated by irradiating SHI. Through channels were generated by selective chemical etching of the amorphous latent track created during irradiation of SHI. Pore dimension and other properties of the membrane were characterized by using SEM, AFM and optical microscope, XRD and DSC to determine the nanostructure, morphology and crystalline structure of the samples. The comparison of the pore dimension in pure PVDF and its nanohybrid has been made. The nanochannels were suitably grafted with styrene monomer on the pore walls of the membranes followed by the sulphonation. Spectroscopic experiments have been performed for grafted polymers followed by the sulphonation of the graft. The conductivity of the modified membrane increases up to semi-conducting range (10<sup>-3</sup> S/cm) (around 12 orders of magnitude higher than pure PVDF) from a perfect insulating PVDF matrix. Proton exchange membrane is one of the important areas in fuel cell and conversion of chemical energy to electrical energy. Proton exchange membrane (PEM) is key factor in fuel cell, which is used as electrolyte cum separator in fuel cell. For proton exchange, properties of the membrane are developed by the functionalization of polymer chain by different ionomers which facilitate the chemical reaction and separate electrons. Accelerator is one of the most promising technologies to generate reactive site as well as porosity in polymer membrane. The functionalized membrane removes the radioactive nuclide like <sup>241</sup>Am<sup>+3</sup> ( $\alpha$ -emitting source) efficiently (~80% or 0.35  $\mu\text{g}/\text{cm}^2$ ) from its solution/waste. This membrane acts as a corrosion inhibitor (92% inhibition efficiency) together with its higher proton conduction (0.13 S/m) ability. The higher ion-exchange capacity, water uptake, ion conduction, and high sorption by the nanohybrid membrane are explored with respect to the extent of functionalization and control over nanochannel dimension. A membrane electrode assembly has been fabricated to construct a complete fuel cell, which exhibits superior power generation (power density of 45 mW/cm<sup>2</sup> at a current density of 298 mA/cm<sup>2</sup>) much higher than that of the standard Nafion, measured in a similar condition. Further, a piezoelectric matrix along with its anticorrosive property, high sorption characteristics, and greater power generation makes this class of material a smart membrane that can be used for many different applications.

## REFERENCES:

- [1] Prakash, Om, Amol M. Mhatre, Rahul Tripathi, Ashok K. Pandey, Pravesh K. Yadav, Saif A. Khan, and Pralay Maiti. *ACS Applied Polymer Materials* (2021) : <https://doi.org/10.1021/acsapm.1c00070>.
- [2] Prakash, O., Mhatre, A. M., Tripathi, R., Pandey, A. K., Yadav, P. K., Khan, S. A., & Maiti, P. (2020). *ACS Applied Materials & Interfaces*, 12(15), 17628-17640.

## 5.2.6 Determination of accurate depth distribution of Au ions in silicon substrates

Md. Akhlak Alam<sup>1,2</sup>, M.K Tiwari<sup>1,2\*</sup>, Devarani Devi<sup>4</sup>, Mukul Gupta<sup>3</sup>, D.K Avasthi<sup>4</sup>

<sup>1</sup>Synchrotron Utilization Section, Raja Ramanna Centre for Advanced Technology, Indore 452013, India

<sup>2</sup>Homi Bhabha National Institute, Anushaktinagar, Mumbai 400094, India

\*[mktiwari@rrcat.gov.in](mailto:mktiwari@rrcat.gov.in)

<sup>3</sup>UGC-DAE Consortium for Scientific Research, University Campus, Khandwa Road, Indore 452017, India

<sup>4</sup>Amity Institute of Nanotechnology, Amity University, Noida 201303, India

Gold implanted silicon substrates are rigorously applied for microelectronics including detectors for imaging application, optoelectronic devices and photo-diodes [1-3], etc. The continuous down scaling of physical size of these devices motivates us to develop methodologies for reliable depth profile studies of various implanted ion species using sensitive and nondestructive methods. To study the depth distribution of Gold ions in Silicon substrates using the combined X-ray reflectivity and grazing incidence X-ray fluorescence techniques, Gold ions were implanted with implantation energy of 80 keV and ion fluences of 10<sup>16</sup> and 5×10<sup>16</sup> ions/cm<sup>2</sup>. In the present project, we report the depth profiling studies using simultaneous X-ray reflectivity (XRR) and grazing

incidence X-ray fluorescence (GIXRF) measurements and secondary ion mass Spectrometry (SIMS) for implanted Gold ions in silicon substrates. We found that SIMS depth profile measurements are not always consistent with the electron density profile obtained using the XRR-GIXRF studies (Fig. 1). Channeling effect of Gold ions in crystalline Silicon structure greatly affects the depth distribution of implanted Au atoms. The electric field distribution and the ratio of phase of reflected electric field and transmitted electric field are also obtained from the structural parameters of simultaneous fitting of the combined XRR-GIXRF measurements. For the study of the surface morphology of the implanted Silicon substrate the atomic force microscope (AFM) measurements are also carried out. The AFM images revealed the strong surface modification and enhanced surface roughness. A manuscript related to above studies is under preparation and to be submitted shortly.

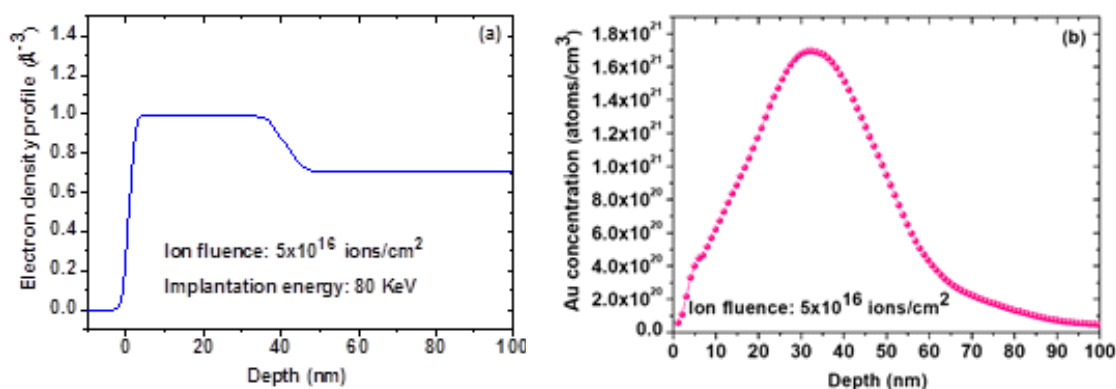


Fig (1). (a) Electron density profile obtained from the analysis of simultaneous XRR-GIXRF measurements (b) SIMS profile.

#### REFERENCES:

- [1] G. Dearnaley, Ion implantation, Nature Vol. 256 August 28, 1975
- [2] Mark T. Winkler, Daniel Recht, Meng-Ju Sher, Aurore J. Said, Eric Mazur, and Michael J. Aziz, PRL 106, 178701 (2011)
- [3] S. Dubois, N. Enjalbert, and J. P. Garandet, Appl. Phys. Lett. 93, 032114 (2008).

### 5.2.7 Anisotropic Magnetoelectric and Magnetotransport Properties of Manganite Based Thin Films

Bhagyashree Udeshi<sup>1</sup>, N.A. Shah<sup>1</sup>

<sup>1</sup>Department of Physics, Saurashtra University, Rajkot-360 005, Gujarat, India.

During this project tenure, polycrystalline targets of  $\text{La}_{0.90}\text{Ca}_{0.10}\text{MnO}_3$  (LCMO) and  $\text{La}_{0.90}\text{Sr}_{0.10}\text{MnO}_3$  (LSMO) were using  $\text{La}_2\text{O}_3$ ,  $\text{MnO}_2$ ,  $\text{CaCO}_3$  and  $\text{SrCO}_3$  powders of 99.999% purity (Sigma Aldrich make) through conventional solid state reaction (SSR) route. Thin films of these targets were fabricated on SNT0 (100) single crystalline substrates using pulsed laser deposition (PLD) technique. Further, these films were irradiated with  $\text{Ag}^{+15}$  ions at an ion fluence of  $1 \times 10^{11}$  ions/cm<sup>2</sup>,  $1 \times 10^{12}$  ions/cm<sup>2</sup> and  $1 \times 10^{13}$  ions/cm<sup>2</sup> using IUAC, New Delhi Pelletron facility.

For all the films, structural studies were carried out using X-ray diffraction (XRD; make: Philips; model: PW 3040/60 X'pert Pro) with Cu K $\alpha$  radiation having  $\lambda = 1.54\text{\AA}$  at room temperature. Frequency dependent electrical properties were performed by high precision LCR meter (make: Agilent; model: E4980A). Dielectric constant with varying frequency was studied in the frequency range of 20 Hz to 2 MHz at room temperature. Moreover, the contribution of the charge carriers and relaxation time can be estimated by two theoretical models, namely, relaxation model and universal dielectric response (UDR) model. The frequency dependent ac conductivity was measured throughout the same frequency range. The hopping mechanism of the charge carriers in the presently studied pristine and irradiated films was evaluated by the theoretical fit of Jonscher's power law. Moreover, impedance behaviour of all the films was performed to recognize the grain and grain boundary contributions, separately, at different frequency ranges between 20 Hz and 2 MHz.

The lattice strain was calculated by the following equation, which was identified as an important parameter to control all these electrical properties of the studied films:

$$\delta = \frac{d_{\text{film}} - d_{\text{substrate}}}{d_{\text{substrate}}} \times 100$$

All the above electrical measurements were also performed in current perpendicular to plane (CPP) geometry, where the direction of applied magnetic field has created a significant alteration in the electrical properties. In

this context, anisotropic magnetodielectric measurements were performed to identify and understand the possible anisotropic magnetodielectric and magnetoelectric nature of the films under study. For the present study, the anisotropic magnetodielectric measurements were carried out in mainly two modes: (i) magnetic field applied perpendicular to the sample plane and (ii) magnetic field applied parallel to the sample plane. Based on the above mentioned characterization method, frequency dependent dielectric, ac conductivity and impedance have been analyzed for all the pristine and irradiated films. However, the morphological study, theoretical fittings and understanding of possible anisotropic magnetodielectric and magnetoelectric properties are under process. According to quantitative studies on the same, it is confirmed that strain between the films and substrates is an important tool to control the anisotropic magnetodielectric and magnetoelectric parameters and properties which will be useful aspect of the present studies.

### 5.2.8 Gamma-ray induced modifications on CdS nanorod mesh: Structural, optical, and electrical properties

Jaya Khatter, R.P. Chauhan

Department of Physics, NIT Kurukshetra, India -136119

Emails: [jaya\\_6180019@nitkkr.ac.in](mailto:jaya_6180019@nitkkr.ac.in), [chauhanrpc@gmail.com](mailto:chauhanrpc@gmail.com)

To study the modifications in the structural, optical and electrical properties, CdS nanorod mesh has been deposited on the glass substrate via chemical bath deposition method. CdS thin film is exposed to high energy gamma radiations at Inter-University Accelerator Center (IUAC), New Delhi. Irradiation is executed from Co-60 gamma source. The irradiation experiment is carried out for different doses from 50 kGy to 200 kGy. The time taken for every dose depends on the activity of source and the activity of source is 2.59 kGy/h. X-ray diffraction exhibits that no structural modifications for the CdS nanorod mesh are observed after gamma irradiation. But variation in the relative intensity can be clearly seen in the diffraction peaks. This is concluded on the account of that gamma photons release energy into the host material which appears in the form of increment in crystallite size and hence, reduction in the lattice imperfection. The optical absorption of CdS nanorod mesh get increased and resulted into reduction in optical band gap as the gamma dose increase. With gamma dose, the number of localized states is increased and therefore, the transition probabilities with the conduction band through the mid gap states also get increased. For this reason, red shift in the energy band gap values of CdS nanorods on irradiation is clearly seen. Electrical conductivity of the CdS nanorod mesh is increased as the gamma dose increases from 50 kGy to 200 kGy. The modifications in the properties of CdS nanorod mesh may be resulted as consequence of ionization and defect production. From this study, it can be summarized that optical band gap and electrical properties can be tuned as a result of gamma irradiation and also suggested the possible applications of CdS nanorod mesh in the advanced nanoscale electronic devices [for details, see *Radiat. Phys. Chem.* 182 (2021) 109353].

#### REFERENCES:

1. J. Khatter, R. P. Chauhan, *Radiat. Phys. Chem.* 182 (2021) 109353.

### 5.2.9 Nitrogen implantation effects on CdS thin films

Jaya Khatter, R.P. Chauhan

Department of Physics, NIT Kurukshetra, India -136119

Emails: [jaya\\_6180019@nitkkr.ac.in](mailto:jaya_6180019@nitkkr.ac.in), [chauhanrpc@gmail.com](mailto:chauhanrpc@gmail.com)

For doping of semiconductors, ion implantation is a promising approach for producing nanoscale crystals or clusters in near surface region which repair the respective optical and electrical properties. In present study, cadmium sulphide (CdS) thin films are grown on microscopic glass substrate via easy and economical chemical bath deposition method. Thereafter, CdS thin films are implanted with 80 keV N<sup>+</sup> beam at different fluences of  $1 \times 10^{15}$ ,  $5 \times 10^{15}$ ,  $1 \times 10^{16}$ , and  $5 \times 10^{16}$  ions/cm<sup>2</sup>. The implantation was performed at Inter University Accelerator Center (IUAC), New Delhi. During implantation, the film samples are fixed on every face of copper ladder which are normal to incident ion beam flux. The ion beam is made incident over an area of  $1 \times 1$  cm<sup>2</sup>. The implantation is performed by employing the chamber pressure of  $10^{-6}$  mbar and current of 1.5  $\mu$ A. The ion beam energy and projected range are estimated by means of SRIM (stopping and range of ions in matter) 2008 simulation program. Table 1 depicts the SRIM calculations for projected range, range straggling, electronic ( $S_e$ ) and nuclear energy losses ( $S_n$ ) values. XRD analysis revealed that consistency of hexagonal phase of CdS thin films after the implantation, and the transferred implanted energy appears in the form of reorientation of planes. SEM analysis revealed the formation of defect clustering due to implantation induced damage. To examine the effects on the optical and electrical; properties, other measurements and analysis are under the way.

**Table 1 SRIM calculations for 80 keV nitrogen implanted CdS films**

Ion species	Nuclear energy loss (eV/ Å)	Electronic energy loss (eV/ Å)	Projected range (Å)	Lateral straggling (Å)	Longitudinal straggling (Å)
80 KeV N <sup>+</sup> ions	52.70	26.41	665	288	393

### 5.2.10 Metal Nanoparticles implanted TiO<sub>2</sub> nanofibers based mesoscopic solar cells

V. Bhullar<sup>1</sup>, N. Kaur<sup>1</sup>, A. Mahajan<sup>1\*</sup>, F. Singh<sup>2</sup>, D. D. Kshetri<sup>2</sup> and S. Chopra<sup>2</sup>

<sup>1</sup>Department of Physics, Guru Nanak Dev University, Amritsar-143005, India

<sup>2</sup>Inter University Accelerator Center, New Delhi-110067, India

Localized surface plasmon resonance (LSPR) is considered to be a unique characteristics property of metal nanoparticles (Mnps), for dye sensitized solar cells, which not only extends the absorption wavelength range of dye into the visible region of solar spectrum but also reduces the recombination reactions occurring at photoanode/electrolyte interface [1-2]. Another way to increase the light harvesting of the DSSCs is to incorporate large sized one dimensional (1-D) nanostructures that provide effective light scattering as well as fast electron transport [3-5]. Simultaneous inclusion of both the nanostructures can possibly lead to substantially large light harvesting with fast electron transport and minimal recombination. Keeping in mind the instability of bare Mnps in the electrolyte, ion implantation technique is opted which solves the corrosion issue of Mnps and provide the optical LSPR for efficient DSSCs [6, 7]. On the basis of our previous reports, thorough proposal has been planned with the objectives: 1) Implantation of Mnps (Ag, Au, C) for enhancing effective absorption cross section of dye in electrospun TiO<sub>2</sub> nanofibers (NFs) incorporated DSSC using low energy ion beam. 2) Fabrication and characterization of high efficient and stable DSSCs using ion beam engineered photoanodes.

In order to complete the proposed work, electrospun TiO<sub>2</sub> NFs incorporated photoanodes were implanted using low energy ion beam facility at IUAC, for the fabrication of DSSCs. Photoanodes were prepared by initial deposition of a compact layer of TiO<sub>2</sub>, prepared from titanium iso-propoxide solution, on pre-cleaned FTO substrates which were then kept for annealing at 450°C for 30 min. TiO<sub>2</sub> NFs (30 wt%) prepared using electrospinning technique were mixed in TiO<sub>2</sub> NPs paste and resulting mixture was doctor bladed with thickness 6µm on compact layer deposited substrates and subsequently calcined for 30 min at 450°C. Ag ions were implanted with energy 120 keV at variable fluence of 10<sup>13</sup>-10<sup>16</sup>. Ag ions penetrate up to 17 nm depth in TiO<sub>2</sub> matrix and was estimated from the stopping and range of ions in matter (SRIM) software. The implanted photoanodes were characterized for structural and optical properties using FESEM, XRD, XPS, UV-Vis, PL, and Raman and kelvin probe spectroscopic techniques. The DSSCs were fabricated using implanted photoanodes and it was observed that Ag implanted photoanodes based DSSCs showed an enhancement of 20% in PCE as compared to unimplanted reference DSSCs.

#### REFERENCES:

- [1] Huili Ran, Jiajie Fan, Xiaoli Zhang, Jing Mao, Applied Surface Science 430 (2018) 415.
- [2] Kouroush Salimi, Abdullah Atilgan, Mustafa Yasir Aydin, HilalYildirim, Nuray Celebi, AbdullahYildiz, Solar Energy 193 (2020) 820.
- [3] Surawut Chuangchote, Takashi Sagawa, and Susumu Yoshikawa, Applied Physics Letters **93** (2008) 033310.
- [4] Maziar Marandi, Elham Rahmani, and Farzaneh Ahangarani Farahani, Journal of Electronic Materials 46 (2017) 6769.
- [5] Wu-Qiang Wu, Fuzhi Huang, Dehong Chen, Yi-Bing Cheng, Rachel A. Caruso, Advanced Energy Materials, 6, 2016, 1502027.
- [6] M.I.Khan, Muhammad Arfan, W.A.Farooq, Aamer Shehzad, Muhammad Saleem, Mahvish Fatima, Ishaq Ahmad, Muhammad Atif, Mona A.
- [7] Almutairi, NafeesahYaqub and MunawarIqbal, Results in Physics 17(2020) 103093.
- [8] Navdeep Kaur, Viplove Bhullar, Davinder Paul Singh and Aman Mahajan, Scientific Reports 10(2020) 7657.

### 5.2.11 Ni<sup>+7</sup> and Si<sup>+9</sup> ion irradiation effect on structural and optical properties of PVA-Ni (NO<sub>3</sub>)<sub>2</sub> Polymeric film

Dipa Singh<sup>1\*</sup>, Shilpa Bhavsar<sup>1</sup>, G. B. Patel<sup>1</sup>, P. K. Mehta<sup>1</sup>, P. K. Khanna<sup>2</sup>, Fouran Singh<sup>3</sup>, N. L. Singh<sup>1</sup>

<sup>1</sup>Department of Physics, The M.S. University of Baroda, Vadodra 390002, India.

<sup>2</sup>Department of Applied Chemistry, Defence Institute of Advanced Technology, Pune, India.

<sup>3</sup>Inter University Accelerator Center, Aruna Asaf Ali Marge, New Delhi 110067, India.

Effect of swift heavy ion irradiation on optical properties of  $\text{Ni}(\text{NO}_3)_2$  salt doped Polyvinyl alcohol (PVA) polymeric films prepared by solution casting technique, was investigated. The optical band gap of pure PVA and PVA/ $\text{Ni}(\text{NO}_3)_2$  composites is calculated using Tauc's expression. The direct band gap is obtained by evaluating the intersection of slope of  $(\alpha h\nu)^2$  vs  $h\nu$  curve on the x-axis. Table-1 gives the variations in optical band gap of Pure PVA and PVA+15%, Nickel Nitrates samples irradiated with 100 MeV  $\text{Ni}^{+7}$  and 100 MeV  $\text{Si}^{+9}$  ions at the fluences of  $1 \times 10^{11}$  and  $1 \times 10^{12}$  ions/cm. Fig.1 shows the UV-Visible spectra of Pure and irradiated polymeric films. It is observed that direct band gap gradually decreases with increase in filler concentrations. After Irradiation the absorption edge become border and shift toward the visible region. The hydrogen and/or other volatile gases are released due to SHI irradiation in polymeric material. This leads to increase in number density of carbon atoms in host material as compared to hydrogen atom, i.e., reduction in H/C atom ratio and formation of conjugated bond resulted in the decrease of optical band gap. The value of (N) in Table 1. indicates that the size of carbon cluster increases with increasing fluence. It is observed that the heavier Nickel ions caused more impact in the optical properties of PVA/ $\text{Ni}(\text{NO}_3)_2$  than lighter Silicon ion due to the more electronic energy loss.

**Table1.**

Sample	Silicon (100 MeV) $E_g$ (eV) N		Nickel (100 MeV) $E_g$ (eV) N	
Pure PVA	5.43	39	5.43	39
Pure PA	5.15	44	5.15	44
PA ( $1 \times 10^{11}$ ions/cm <sup>2</sup> )	4.91	48	3.59	91
PA ( $1 \times 10^{12}$ ions/cm <sup>2</sup> )	3.25	111	2.75	155

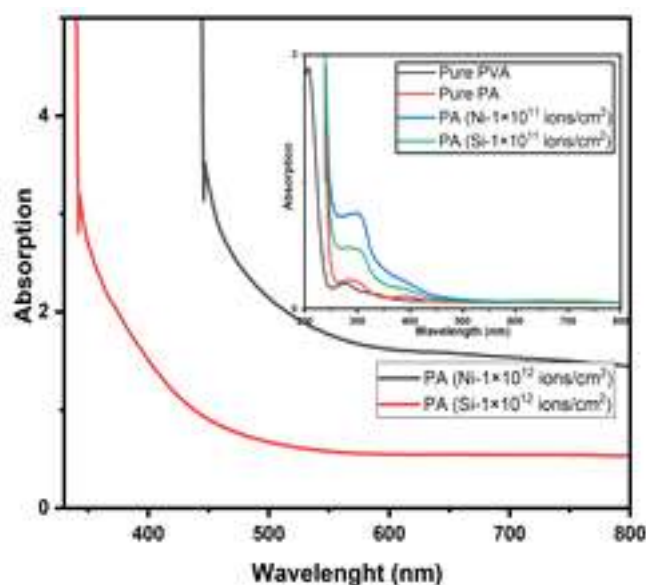


**Fig.1** UV-Visible spectrum of PVA and PA (PVA + 15% Nickel Nitrate) 100 MeV Ni and 100 MeV Si ions at the fluences of  $1 \times 10^{11}$  and  $1 \times 10^{12}$  ions/cm<sup>2</sup>, respectively. (Inset) Variation in optical energy band gap ( $E_g$ ) at different fluences of 100 MeV Ni and 100 MeV Si ion irradiation for Pure PVA and PA (PVA + 15% Nickel Nitrate) samples.

#### REFERENCES:

- [1] Gnansagar B. Patel et al. Modification of chitosan based biodegradable polymer by irradiation with MeV ions for electrolyte applications. *Materials science and Engineering B* 225 (2017) 150 – 159.

#### 5.2.12 RBS Investigations on Si and Ge bombarded with 100KeV Ar Ion Beam

<sup>a</sup>Indra Sulania, <sup>a</sup>Sunil Ojha, <sup>a</sup>G R Umaphathy, <sup>a</sup>Ambuj Tripathi, <sup>b</sup>Richa Krishna and <sup>b</sup>D K Avasthi

<sup>a</sup>Inter University Accelerator Centre, Aruna Asaf Ali Marg, New Delhi 110067, India

<sup>b</sup>Amity Institute of Nanotechnology, Amity University, Noida 201303, India

\*Email: indra.sulania@gmail.com; indra@iuac.res.in

Rutherford back scattering (RBS) studies in channeling mode have been used to study defects in crystals for more than a few decades now [1]. It helps researchers to determine the structure and composition of the materials and the damage fraction of the ion treated crystals by detecting the backscattering of a beam of high energy ions (1-2 MeV He<sup>+</sup>), impinging on the target material as shown in schematic in figure 1.

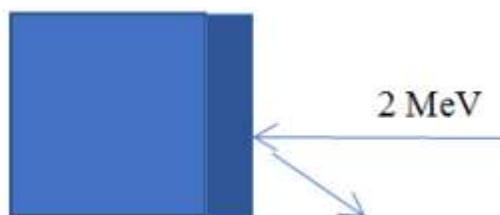


Fig 1: Schematic showing He ions impinging on Pre-damaged Si(100)/ Ge(100) samples.

Single-crystal materials such as Si and Ge have ordered arrays of atoms. If an ion beam arrives in alignment with the atomic planes, most of the ions will pass through the space between the planes of atoms and will penetrate deep within the crystal. Channeling studies used this phenomenon to find the structure of the crystal and to locate the interstitial atoms sitting within the array of target atoms. Typical ion beams used for RBS channeling is 1-2MeV He<sup>+</sup> ions, it provides good mass and depth resolution and small radiation damage [2].

In the present study, RBS/C studies are performed on Si(100) and Ge(100) already bombarded with 100 keV Ar<sup>+</sup> ion beam in the ion fluence range of  $\sim 3 \times 10^{17}$  to  $9 \times 10^{17}$  ions/cm<sup>2</sup> incident at  $\theta \sim 60^\circ$  with respect to surface normal. The RBS/C spectra is shown in figure 2(a) and (b) for Si and Ge single crystal pristine and irradiated samples respectively. The RBS spectrum recorded for the pristine sample in random orientation displays two steps corresponding to the backscattering from the silicon and Ar for channel numbers  $\sim 1100$  and  $\sim 1250$  respectively

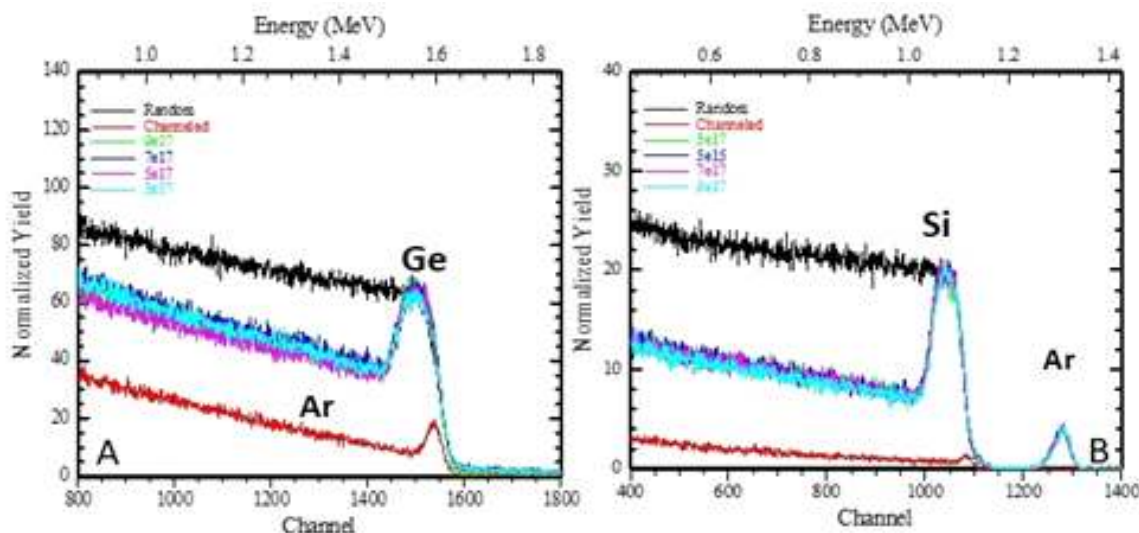


Fig 2 Shows the (100) aligned spectra for (a) Si and (b) Ge target before and after ion irradiation with 100 keV Ar<sup>+</sup> ions at various ion fluence  $3 \times 10^{17}$  to  $9 \times 10^{17}$  ions/cm<sup>2</sup>.

The Ar<sup>+</sup> ions irradiated Si & Ge targets produces clearly visible damage peaks between channels 1000–1100 (figure 2a) & 1500 – 1600 (figure 2b) respectively. Clustering of defects leads to the subsequent increase of the damage peak in irradiated target as compared to pristine targets of Si & Ge samples was extracted by using the simulation code “De-channeling In Crystals And Defect Analysis (DICADA)” [3].

#### REFERENCES:

- [1] E. Bøgh; Defect studies in crystals by means of channeling; Can. J. Phys., 46 (1968), p. 653
- [2] Y. Quéré; Dechanneling Cylinder of Dislocations; Phys. Stat. Sol., 30 (1968), p. 713.
- [3] Modified master equation approach of axial dechanneling in perfect compound crystals; K.Gärtnerbaep-author-id6; Nuclear Instruments and Methods in Physics Research Section B: Beam Interactions with Materials and Atoms; 227(2005) 522.

### 5.2.13 Defects Assisted Structural and Electrical Properties of Ar Irradiated TiO<sub>2</sub>/SrTiO<sub>3</sub> Bilayer

Anuradha Bhogra<sup>1\*</sup>, Anha Masarrat<sup>1,2</sup>, Dilruba Hasina<sup>3</sup>, Ramcharan Meena<sup>1</sup>, Ashish Kumar<sup>1</sup>, Tapobrata Som<sup>3</sup>, Chung-Li Dong<sup>4</sup>, Chi-Liang Chen<sup>5</sup>, and Asokan Kandasami<sup>15</sup>

<sup>1</sup>Inter-University Accelerator Centre, Aruna Asaf Ali Marg, New Delhi-110067, India

<sup>2</sup>Department of Physics, Jamia Millia Islamia University, New Delhi-110025, India

<sup>3</sup>Institute of Physics, Bhubaneswar - 751005, India

<sup>4</sup>Department of Physics, Tamkang University, Tamsui 251, Taiwan

<sup>5</sup>National Synchrotron Radiation Research Centre, Hsinchu, Taiwan

This work presents the effect of Ar irradiation on the TiO<sub>2</sub>/STO bilayer films fabricated by PLD technique on two different substrates: Si and STO. The X-ray diffraction (XRD) spectra show the orientation of TS-Si:Ar from the TiO<sub>2</sub> as well as STO whereas only (200) orientation of STO phase is observed for film deposited at STO substrate. However, the XRD peaks become broad and intensity reduces after 1 MeV Ar irradiation. This irradiation creates defect and disorder in the crystal structure and results in suppression of the XRD peak intensity.

Both the pristine films, TS-Si and TS-STO, show insulating behaviour. After Ar irradiation, TS-Si:Ar exhibit highest conductivity as compared to TS-STO:Ar. This is due to large number of oxygen vacancies created in TS-Si:Ar film. The film TS-Si:Ar shows the Seebeck coefficient (S) of 195  $\mu\text{V/K}$  and power factor ( $S^2/\rho$ ) of 0.13  $\text{mW}\cdot\text{m}^{-1}\text{K}^{-2}$  at 420 K respectively which is comparable to the Nb-STO/STO superlattices. From the X-ray absorption spectroscopy, it is revealed a decrease of valence state of Ti ion due to increase of oxygen vacancies. The splitting of  $e_g$  peak into  $d_z^2$  and  $d_{x^2-y^2}$  components implies lowering of cubic symmetry and change in the bond length of Ti-O. These results are consistent with the XRD and conductivity data. This is supposed to be related with the Ar irradiation which produces defects and structural distortion in the lattice. Each oxygen vacancy frees two electrons and lead to reduction of valence state of Ti 3d orbitals. An increase in oxygen vacancies allows electrons to occupy higher energy levels near conduction band and contributes to decrease in activation energy and thereby increasing electrical conductivity.

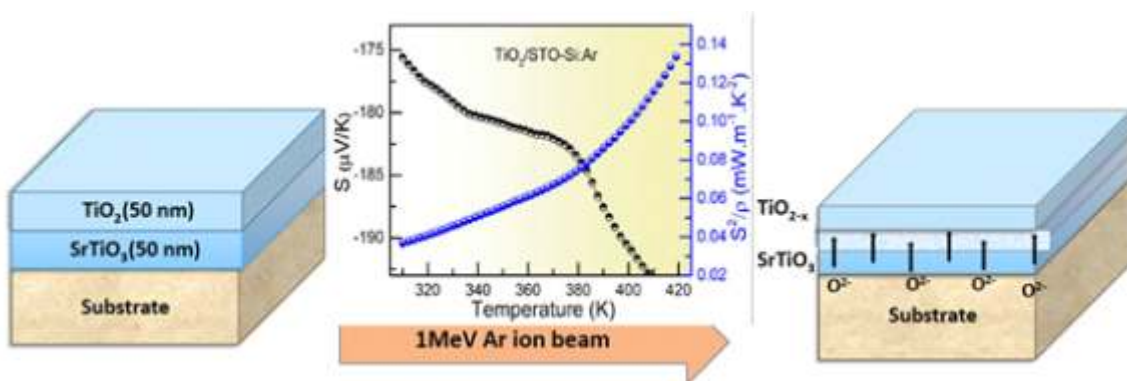


Fig: Schematic of TiO<sub>2</sub>/SrTiO<sub>3</sub> films irradiated with 1 MeV Ar ion beam and variation of Seebeck coefficient (S) and Power factor ( $S^2/\rho$ ) with temperature.

Above results can be understood based on two or more possible approaches: (i) Strain produced due to lattice mismatch; (ii) Interfacial conductivity, formation of two dimensional electron gas layer at interface between TiO<sub>2</sub>/STO and combination of both these. Considering the first factor, this could be correlated to the lattice mismatch which is 1.7% with Si substrate and hence, strain produced favours the formation of oxygen vacancies after Ar irradiation as compared to the film deposited on the STO substrate. Secondly, interface plays an important role in modifying the transport properties. It is assumed that oxygen deficient TiO<sub>2</sub> layer is formed as a result of Ar irradiation that may extract the oxygen from STO layer and thereby generating a conductive layer near surface layers, hence responsible for the increased conductivity. Ar irradiation plays a vital role to modify the transport properties.

#### REFERENCES:

**Bhogra et al.**, "Defect assisted structural and electrical properties of Ar ion beam irradiated TiO<sub>2</sub>/SrTiO<sub>3</sub> bilayer", *Material Letters*, 282, 128880 (2021).

Ohta, H. *et al.* Giant thermoelectric Seebeck coefficient of a two-dimensional electron gas in SrTiO<sub>3</sub>. *Nat Mater* 6, 129-134, (2007).

Zhang, B. *et al.* High thermoelectric performance of Nb-doped SrTiO<sub>3</sub> bulk materials with different doping levels. *Journal of Materials Chemistry C* 3, 11406-11411, (2015).

Kumar, S. R., Barasheed, A. Z. & Alshareef, H. N. High temperature thermoelectric properties of strontium titanate thin films with oxygen vacancy and niobium doping. *ACS applied materials & interfaces* **5**, 7268-7273, (2013).

Kan, D. *et al.* Blue-light emission at room temperature from Ar<sup>+</sup>-irradiated SrTiO<sub>3</sub>. *Nature Materials* **4**, 816-819, (2005).

### 5.2.14 Magnetic and electronic structures of N Implanted Iron Oxide Thin Films

Razia Nongjai<sup>1</sup>, R. Samad<sup>2</sup>, V. R. Singh<sup>3</sup>, V. K. Verma<sup>4</sup>, K. Asokan<sup>11</sup> Materials Science Division, Inter-University Accelerator Center, Aruna Asaf Ali Marg, New Delhi 110067

<sup>1</sup>Department of Physics, University of Kashmir, Hazratbal, Srinagar, Jammu and Kashmir 190006

<sup>3</sup>Department of Physics, Central University of South Bihar, Gaya-824236 (Bihar), India

<sup>4</sup>Department of Physics, Madanapalle Institute of Technology & Science, Angallu, Madanapalle 517325, Andhra Pradesh.

Magnetite (Fe<sub>3</sub>O<sub>4</sub>) has attracted many researchers since last century due to its novel properties such as complex electronic structure, relatively high saturation magnetization with high Curie temperature ~ 860K, half metallicity, and large spin polarization with diverse technological applications. The growth of single-phase Fe<sub>3</sub>O<sub>4</sub> films is a significant challenge to researchers and hence a careful optimization of the growth condition or post-deposition treatment such as annealing in inert or reactive gas is often implemented. Ion implantation is a unique tool that can incorporate inert or reactive gas ions in a controlled manner to a material system. Ion implantation not only introduces the dopant in the materials but also annealed the target locally and creates defects depending upon the ion energy, mass, and fluences. The doping, annealing, and creation of defects can be synergistically achieved with ion implantation. In this report, we present the N ions implantation as a novel way to control magnetic and electrical properties of Fe<sub>3</sub>O<sub>4</sub> thin films.

Fe<sub>3</sub>O<sub>4</sub> thin films of 100 nm were deposited on Si (100) substrate using the electron beam evaporation [1]. After the deposition, 26 keV N ions were implanted on this film at a fluence of 1×10<sup>16</sup> ions/cm<sup>2</sup> using the 30 KV Tabletop accelerator housed in Inter-University Accelerator Centre (IUAC), New Delhi. The changes in structural and magnetic properties of pristine and N ions implanted films were probed by the Raman Spectroscopy, Vibrating Sample Magnetometer (VSM) with field up to 20 kOe at room temperature, X-Ray Absorption Spectroscopy (XAS), X-ray Magnetic Circular Dichroism (XMCD) (Beamline BL-16 of KEK-PF, Japan). All the data of the XAS were taken at room temperature in the total electron yield (TEY) mode which is a surface-sensitive with the probing depth up to ~5 nm. For transport properties, the Hall Effect measurements were carried out using a magnetic field of 0.5 T at room temperature using Ecopia Hall effect measurement system, HMS-3000.

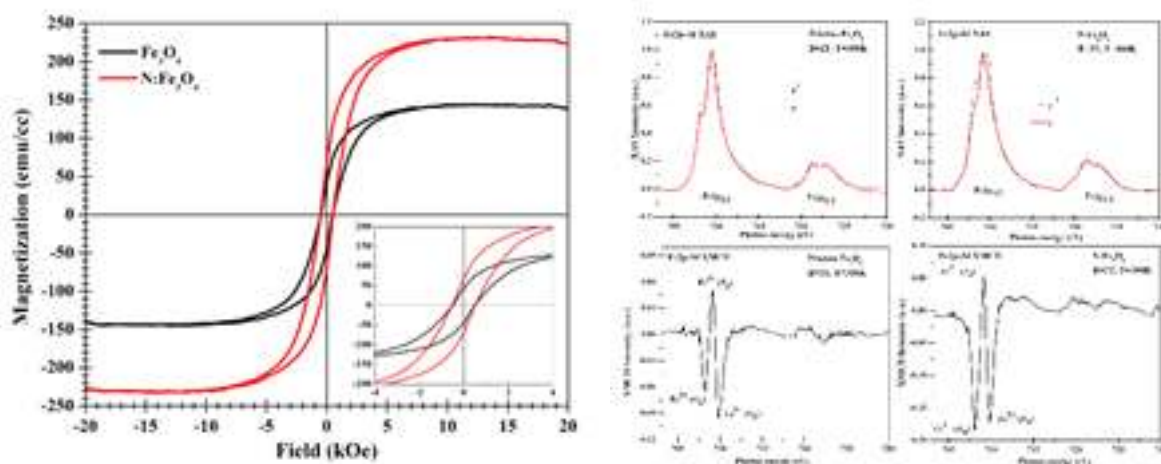


Fig. 1 Hysteresis loops (Left side) of pristine Fe<sub>3</sub>O<sub>4</sub> and N:Fe<sub>3</sub>O<sub>4</sub> films and Fe L-edge XAS and XMCD Spectra (Right Side) at 10° from the surface plane of pristine Fe<sub>3</sub>O<sub>4</sub> and N:Fe<sub>3</sub>O<sub>4</sub> films.

The cubic spinel phase was confirmed both in pristine Fe<sub>3</sub>O<sub>4</sub> and N ions implanted Fe<sub>3</sub>O<sub>4</sub> films by Raman Spectroscopy. Fig. 1 shows the hysteresis loops (left side) and Fe L-edge XAS and XMCD Spectra (right Side) at 10° from the surface plane of pristine Fe<sub>3</sub>O<sub>4</sub> and N:Fe<sub>3</sub>O<sub>4</sub> films. The pristine Fe<sub>3</sub>O<sub>4</sub> thin film is ferrimagnetic at room temperature with a reduced moment attributed to the presence of high density of defects such as amorphous boundary and the local non-stoichiometry. The magnetic parameters  $H_c$ ,  $M_r$ , and  $M_s$  enhance after N ions implantation. The microscopic origin of the changes in the magnetic properties of Fe<sub>3</sub>O<sub>4</sub> thin films is understood to be the variation of Fe<sup>2+</sup> ions at octahedral sites due to Fe vacancy leading to the non-stoichiometric Fe<sub>3- $\delta$</sub> O<sub>4</sub> which stabilizes after N ions implantation. The Hall effect measurements show the

increment in carrier concentration and reduction in resistivity after N ions implantation which further suggests that  $\text{Fe}^{2+}$  ions at octahedral sites increases which led to the improvement in the magnetic properties.

#### REFERENCES:

- [1] Razia Nongjai, R. Samad, V. R. Singh, V. K. Verma, K. Asokan, J. Magn. Magn. Mater., **527**, 167703 (20

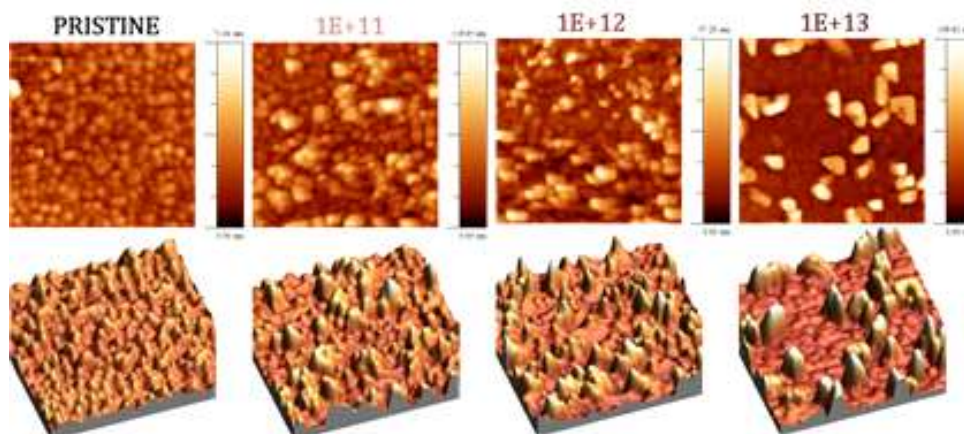
### 5.2.15 Swift Heavy Ion Irradiation Studies on Manganite Based Thin Film Devices

Bhargav Rajyaguru, P.S. Solanki, and N.A. Shah

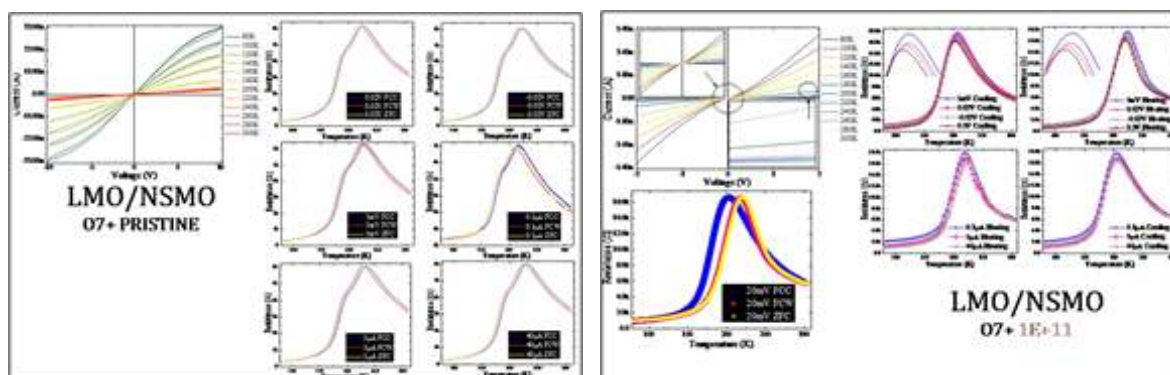
*Department of Physics, Saurashtra University, Rajkot, 360005, India*

$\text{LaMnO}_3 / \text{La}_{0.7}\text{Ca}_{0.3}\text{MnO}_3$  and  $\text{LaMnO}_3 / \text{Nd}_{0.7}\text{Sr}_{0.3}\text{MnO}_3$  manganite based bilayered devices were grown on single crystalline (100)  $\text{SrTiO}_3$  substrates using low cost chemical solution deposition method. These devices were prepared under different heating treatments intentionally to differentiate two manganite layers as well as to prepare possibly p-n junctions. Prior to irradiation, pristine films were characterized by X-ray diffraction (XRD) measurements as well as PHI-scan experiment to identify the structural aspects of the pristine films. Structural analysis has proven good quality structure of all the pristine bilayered devices. Irradiation was performed by using (i) 120MeV  $\text{Ag}^{+9}$  and (ii) 100MeV  $\text{O}^{+7}$  ions with different fluence. After irradiation for all 16 bilayered thin film devices, we have performed the XRD and PHI-scan measurements for all the bilayered devices.

Atomic force microscopy (AFM) measurement was also performed for all the devices to understand the irradiation induced modifications / creation of defects on the surface of the films. Interesting results and observations have been obtained from these measurements. Influence of irradiation on film – substrate lattice strain and surface morphology has been observed for all studied bilayered devices. Following figure shows a typical set of AFM images for pristine and irradiated  $\text{LaMnO}_3 / \text{Nd}_{0.7}\text{Sr}_{0.3}\text{MnO}_3$  manganite based bilayered devices where irradiation was carried out by using 100MeV  $\text{O}^{+7}$  ions.



Few different transport measurements including current–voltage characteristics, resistive switching behavior, electroresistance and field effect configuration (FEC) measurements were performed for different temperatures, electric fields, currents, magnetic fields and measurement geometries for all studied pristine and irradiated thin film devices. Following figures show typical hysteretic  $I - V(T)$  characteristics recorded at different temperatures and FEC based behaviors under different currents and voltages for  $\text{LaMnO}_3 / \text{Nd}_{0.7}\text{Sr}_{0.3}\text{MnO}_3$  bilayered pristine and irradiated (fluence:  $1 \times 10^{11}$  ions/cm<sup>2</sup>) devices.



### 5.2.16 Swift heavy ion irradiation-induced modifications in the electrical and surface properties of $\beta$ -Ga<sub>2</sub>O<sub>3</sub>

N. Manikanthababu<sup>1,4</sup>, B. R. Tak<sup>2</sup>, K. Prajna<sup>3</sup>, S. Sarkar<sup>4</sup>, K. Asokan<sup>5</sup>, D. Kanjilal<sup>5</sup>, S. R. Barman<sup>4</sup>, R. Singh<sup>2</sup> and B. Panigrahi<sup>1,6</sup>

<sup>1</sup>Materials Science Group, Indira Gandhi Center for Atomic Research, Kalpakkam, India 603102.

<sup>2</sup>Department of Physics, Indian Institute of Technology Delhi, New Delhi, India 110016.

<sup>3</sup>Non-Destructive Evaluation Division, MMG, Indira Gandhi Centre for Atomic Research, Kalpakkam, India 603102.

<sup>4</sup>UGC-DAE Consortium for Scientific Research, Indore, Madhya Pradesh, India 452017.

<sup>5</sup>Inter University Accelerator Centre, Aruna Asaf Ali Marg, New Delhi, India 110067.

<sup>6</sup>Electronics and Instrumentation Group, Indira Gandhi Center for Atomic Research, Kalpakkam, India 603102.

The quest for the high performance and high-power semiconductor devices empowered the rapid development of power electronics industry. In recent times Ga<sub>2</sub>O<sub>3</sub> has come into the limelight as a potential electronic material for power semiconductor device applications.  $\beta$ -Ga<sub>2</sub>O<sub>3</sub>-based devices have been tested for their sustainability in intense radiation environments which is a theme of extensive research in recent years. The effects of swift heavy ions (SHIs) on the electrical properties of  $\beta$ -Ga<sub>2</sub>O<sub>3</sub>-based devices are primitive at this stage. In general, these ions are found in nuclear reactions and in cosmic radiation. In cosmic particle radiation containing mostly energetic protons ranging from 500-1000 MeV/u. The present work focuses on the fundamental aspects of ion–solid interaction mechanism in the state-of-the-art  $\beta$ -Ga<sub>2</sub>O<sub>3</sub>-based technology to develop and design radiation-hardened devices.

An orientation of ( $\bar{2}01$ )  $\beta$ -Ga<sub>2</sub>O<sub>3</sub> (M/s Tamura Corp., Japan), n-type and Sn-doped with a doping concentration of  $\sim 1.6 \times 10^{18}$  cm<sup>-3</sup> wafer sliced into 1 cm  $\times$  1 cm were used for the present study. Schottky Ni (20 nm)/Au (80 nm) circular contacts (1 mm dia.) through a metal mask were deposited using e-beam evaporation. In order to make a vertical SBD, the Ohmic Ti (20 nm)/Au (80 nm) contact has been deposited on the backside of  $\beta$ -Ga<sub>2</sub>O<sub>3</sub> by e-beam deposition. These devices were mounted on a specially designed Cu ladder for in situ electrical characterization upon irradiation of 120 MeV Ag<sup>7+</sup> ions at various fluences of  $1 \times 10^{10}$  to  $1 \times 10^{12}$  cm<sup>-2</sup> at room temperature. These experiments were performed by using 15 UD Pelletron Accelerator facility available at Inter University Accelerator Centre (IUAC), New Delhi, India. A constant beam current of 0.5 particle nano-Ampere ( $\sim 0.5$  pA) has been maintained throughout the experiment, and the beam is uniformly scanned over 1 cm  $\times$  1 cm area on the devices. All the in situ measurements were performed on the same device at different ion fluences to evade any incongruity in the devices using Agilent technologies B1500A semiconductor device analyzer within the voltage range of  $-3$  to  $+2$  V. Al-K $\alpha$  X-ray source equipped with Scienta R4000 analyzer was used for the XPS measurements.

The in situ I–V characteristics of  $\beta$ -Ga<sub>2</sub>O<sub>3</sub> SBD at various fluences of 120 MeV Ag<sup>7+</sup> ions are shown in Fig. 1. Inset shows the results from the SRIM-2013 of 120 MeV Ag<sup>7+</sup> ion irradiation in Au (80 nm)/Ni (20 nm)/ $\beta$ -Ga<sub>2</sub>O<sub>3</sub> SBD.

The electrical device characteristics of Ni/ $\beta$ -Ga<sub>2</sub>O<sub>3</sub> vertical Schottky barrier diodes (SBDs) were measured in situ during the irradiation of 120 MeV Ag<sup>7+</sup> swift heavy ions (SHIs). These devices exhibit SHI irradiation-induced degradation with 120 MeV Ag<sup>7+</sup> ions at the ion fluences ranges from  $1 \times 10^{10}$  ions/cm<sup>2</sup> to  $1 \times 10^{12}$  ions/cm<sup>2</sup>. The height of the Schottky barrier is found to decrease from 1.11 to 0.93 eV, and the ideality factor increases from 1.16 to 2.06 (see Fig. 2). These changes indicate the degradation of the device with SHI irradiation. A significant four orders increase is observed in the leakage current density from  $4.04 \times 10^{-8}$  to  $1.98 \times 10^{-4}$  A/cm<sup>2</sup> at  $-1$  V, and the series resistance also increases from  $3.38 \times 10^3$  to  $1.15 \times 10^4$   $\Omega$ . X-ray photoelectron spectroscopy measurements show that the Ga ions are present in divalent and trivalent states with the spectral features having the binding energies centered at 20.2 eV and 19.9 eV (Ga 3d core-levels) before and after ion irradiation (see Fig. 3). The O 2s peak shifts to 23.7 eV, and there is an increase in intensity and peak broadening due to change in trivalent to the divalent state of Ga due to the irradiation. The O(I) peak appears at 530.7 eV in pristine sample assigned the Ga–O bonding with the Ga<sup>3+</sup> state in pure Ga<sub>2</sub>O<sub>3</sub>. Moreover, there is a significant change in the intensity and the peak width of O(II) centered at 533.0 eV after irradiation at the fluence of  $1 \times 10^{12}$  ions/cm<sup>2</sup>. This indicates that there is an increase in the surface adsorbed/lattice oxygen resulting in GaO.

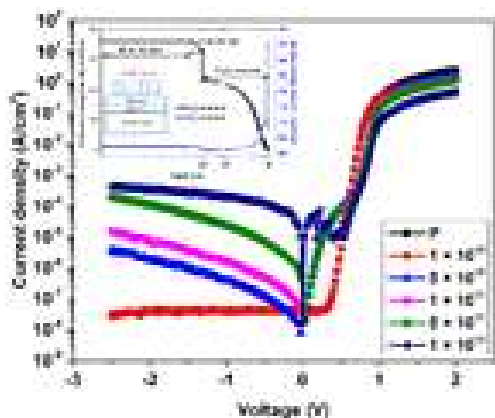


Fig. 1

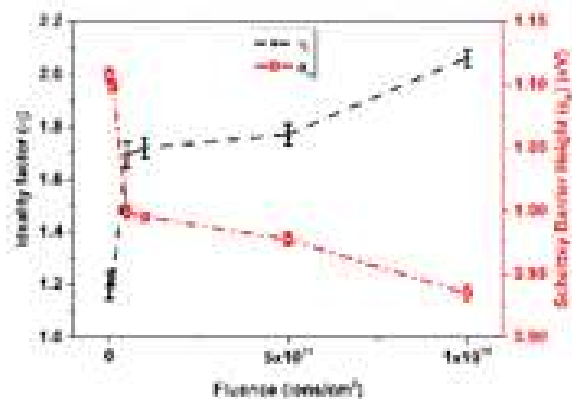


Fig. 2

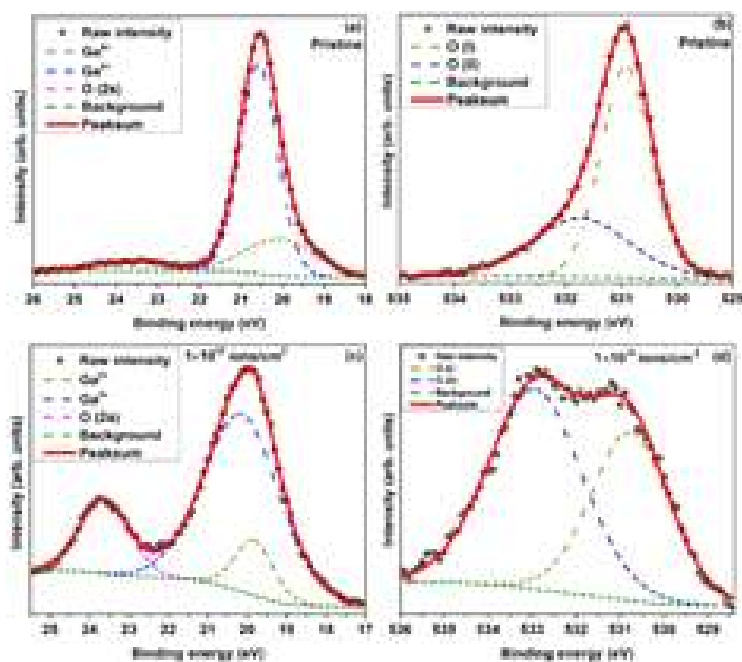


Fig. 3

## REFERENCES:

- <sup>1</sup> M. Higashiwaki, H. Murakami, Y. Kumagai, and A. Kuramata, *Jpn. J. Appl. Phys.* **55**, 1202A1 (2016).
- <sup>2</sup> M. Higashiwaki, K. Sasaki, A. Kuramata, T. Masui, and S. Yamakoshi, *Phys. Status Solidi* **211**, 21 (2014).
- <sup>3</sup> S.J. Pearton, R. Deist, F. Ren, L. Liu, A.Y. Polyakov, and J. Kim, *J. Vac. Sci. Technol. A Vacuum, Surfaces, Film.* **31**, 050801 (2013).
- <sup>4</sup> S. Rafique, L. Han, M.J. Tadjer, J.A. Freitas, N.A. Mahadik, and H. Zhao, *Appl. Phys. Lett.* **108**, 182105 (2016).
- <sup>5</sup> M. Higashiwaki, A. Kuramata, H. Murakami, and Y. Kumagai, *J. Phys. D: Appl. Phys.* **50**, 333002 (2017).
- <sup>6</sup> M. Higashiwaki, K. Sasaki, H. Murakami, Y. Kumagai, A. Koukitu, A. Kuramata, T. Masui, and S. Yamakoshi, *Semicond. Sci. Technol.* **31**, 034001 (2016).
- <sup>7</sup> J. Kim, S.J. Pearton, C. Fares, J. Yang, F. Ren, S. Kim, and A.Y. Polyakov, *J. Mater. Chem. C* **7**, 10 (2019).
- <sup>8</sup> J.F. Ziegler, *Nucl. Instruments Methods Phys. Res. Sect. B Beam Interact. with Mater. Atoms* **219–220**, 1027 (2004).
- <sup>9</sup> J.F. Ziegler, M.D. Ziegler, and J.P. Biersack, *Nucl. Instruments Methods Phys. Res. Sect. B Beam Interact. with Mater. Atoms* **268**, 1818 (2010).

### 5.2.17 Study of Resistive Switching of Ion Beam Irradiated Films with Spectroscopic Correlations

K. N. Rathod<sup>1</sup>, J. P. Singh<sup>2</sup>, K. H. Chae<sup>2</sup>, K. Asokan<sup>3</sup>, N. A. Shah<sup>1</sup>, P. S. Solanki<sup>1</sup>

<sup>1</sup>Department of Physics, Saurashtra University, Rajkot, India

<sup>2</sup>Advanced Analysis Center, Korea Institute of Science and Technology, Seoul, Republic of Korea

<sup>3</sup>Inter University Accelerator Centre, Aruna Asaf Ali Marg, New Delhi, India

Hysteretic resistive switching (RS) based resistive random access memories (RRAMs) in the transition metal oxides have attracted considerable attention because of exceptional scalability, high integration density, fast switching, etc [1]. Many metal oxide materials present a noteworthy part of promising memristive materials due to the presence of RS characteristics [2]. In recent times, it is reported that nanostructures containing manganites can also exhibit RS behaviour [3]. Trivial change in oxygen stoichiometry causes strong deviation in electrical conductivity and magnetic state [4]. Therefore, materials with non-inherent RS may accomplish this feature with new findings. Ion irradiation is the tool which can create controlled structural disorder as well as localized strain [5]. Sensitive nature of manganites towards strain and structural disorder lead to significant modifications in transport and magnetic properties of ion irradiated hole-doped manganites [6]. The ion beam experiments of 100MeV  $O^{7+}$  ions on  $Y_{0.95}Ca_{0.05}MnO_3$  (YCMO) thin films were performed at IUAC, New Delhi to report the effects of ion irradiation on resistive switching.

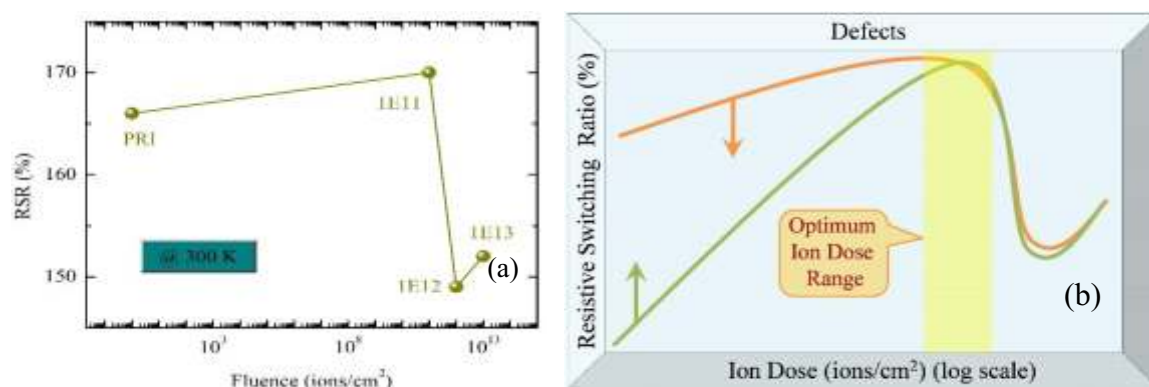


Fig. 1 (a) RSR of YCMO performed at room temperature (b) Model of defects and ion dose with RSR

To demonstrate above effect, the resistive switching ratio (RSR) was performed with model. RSR of YCMO as a function of ion fluence (at room temperature) is shown in fig.1 (a). From PRI to 1E11, the RSR is increased due to more number of oxygen vacancies present in 1E11 film. For higher irradiated films (1E12 and 1E13), RSR is reduced as a result of decrease in oxygen vacancies. Experimental confirmation of this deviation in oxygen vacancies is executed by RBS and NEXAFS measurements. Figure 4 illustrates a model that represents the RSR with defects and ion dose at room temperature (300 K). By keeping in mind that the defects are lowest in PRI film as compared to the irradiated films, the model has been prepared. Lower defects and ion dose point out lower RSR in percentage. With increase in defects and ion dose, the RSR also increases up to certain defects and ion dose level i.e. optimal ion dose range or critical ion dose. After optimal ion dose, the RSR decreases and, then, slightly increases.

#### REFERENCES:

1. X.J. Zhu, J. Shang and R.W. Li, Resistive switching effects in oxide sandwiched structures, *Front. Mater. Sci.* 6 (2012) 183–206.
2. X. Hong, D.J. Loy, P.A. Dananjaya, F. Tan, C. Ng and W. Lew, Oxide-based RRAM materials for neuromorphic computing, *J. Mater. Sci.* 53 (2018) 8720–8746.
3. N. Manca, L. Pellegrino and D. Marré, Reversible oxygen vacancies doping in  $(La_{0.7}, Sr_{0.3})MnO_3$  microbridges by combined self-heating and electromigration, *Appl. Phys. Lett.* 106 (2015) 203502:1–5.
4. A.J. Grutter, D.A. Gilbert, U.S. Alaan, E. Arenholz, B.B. Maranville, J.A. Borchers, Y. Suzuki, K. Liu and B.J. Kirby, Reversible control of magnetism in  $La_{0.67}Sr_{0.33}MnO_3$  through chemically-induced oxygen migration, *Appl. Phys. Lett.* 108 (2016) 082405:1–5.
5. R. Kumar, S.B. Samanta, S.K. Arora, A. Gupta, D. Kanjilal, R. Pinto and A.V. Narlikar, Study of columnar amorphization and structural symmetry changes produced by swift heavy ion irradiation in  $YBa_2Cu_3O_{7-x}$  thin films using STM, *Solid State Commun.* 106 (1998) 805–810.
6. S.B. Ogale, K. Ghosh, J.Y. Gu, R. Shreekala, S.R. Shinde, M. Downes, M. Rajeswari, R.P. Sharma, R.L. Greene, T. Venkatesan, R. Ramesh, R. Bathe, S.I. Patil, R. Ravikumar, S.K. Arora and G.K. Mehta, Influence of 90 MeV oxygen ion induced disorder on the magnetotransport in epitaxial  $La_{0.7}Ca_{0.3}MnO_3$  thin films, *J. Appl. Phys.* 84 (1998) 6255–6261 □

### 5.2.18 Origin of intense blue-green emission and bandgap engineering in SrTiO<sub>3</sub> thin films using ion-beam techniques: An synchrotron-based spectroscopic study

Vishnu Kumar<sup>1</sup>, Anuradha Bhogra<sup>2</sup>, Manju Bala<sup>1</sup>, Hung-Wei Kuo<sup>3</sup>, S. C. Haw<sup>3</sup>, C. L. Chen<sup>3</sup>, C. L. Dong<sup>4</sup>, K. Asokan<sup>2</sup>, and S. Annapoorni<sup>1</sup>

<sup>1</sup>Department of Physics and Astrophysics, University of Delhi, Delhi, 110007, India

<sup>2</sup>Inter-University Accelerator Centre, Aruna Asaf Ali Marg, New Delhi, 110067, India

<sup>3</sup>National Synchrotron Radiation Research Center, Hsinchu, 30076, Taiwan

<sup>4</sup>Department of Physics, Tamkang University, Tamsui 25137, Taiwan

SrTiO<sub>3</sub> (STO) thin films were deposited on quartz substrates using a commercial STO target of 2 mm thickness and 5 cm diameter by radio frequency (RF) magnetron sputtering (HIND HIVAC, Model 12" MSPT) in the presence of oxygen (20%) balanced with argon gas. The cleaned quartz substrates of dimensions 10 mm × 10 mm × 2 mm were used to deposit STO thin films. These films were annealed at 750 °C for 5 h in a horizontal tubular furnace in the ambient of Ar+O<sub>2</sub> (20%) gas. The thickness of the films was determined to be ~220 nm. These pristine films were implanted with 100 keV N ion beam using the low energy ion beam facility (LEIBF) housed in Inter-University Accelerator Centre (IUAC), New Delhi with different fluences viz.  $\sim 5 \times 10^{14}$ ,  $\sim 1 \times 10^{15}$ ,  $\sim 5 \times 10^{15}$ , and  $\sim 1 \times 10^{16}$  ions/cm<sup>2</sup>. For the structural characterization, synchrotron glancing incidence X-ray Diffractometer (GIXRD) operated at 13 keV was used at MCX Beamline, Elettra Sincrotrone Trieste, Italy. Further, the samples were characterized by synchrotron PL spectroscopy at TLS-03A1, and XAS at TLS-20A1 & TLS-17C1 beamlines of National Synchrotron Radiation Research Center (NSRRC), Hsinchu, Taiwan. The XRD pattern shows a shift in reflections at lower N ion fluences and the amorphization of the films at higher fluences. A disordered phase induced by implantation in the STO films leads to an intense blue-green emission due to oxygen (O) vacancies and N (2p) bound states. A schematic diagram of energy levels has been proposed to explain the origin of PL emission. The XANES spectra at Ti K-edge reflect a change in the valency of Ti ions and the local atomic structure of ordered and disordered phases of STO with an increase in N ion fluence. The splitting of peak assigned to e<sub>g</sub> orbitals, and discrepancy in ratio  $d_z^2/d_{x-y}^2$  observed in the Ti L- and O K-edge spectra confirm a distortion in TiO<sub>6</sub> octahedral structure and modifications in O 2p-Ti 3d hybridization states. The synchrotron-based techniques reveal that N ion implanted STO can be a good photoluminescent material exhibiting a variety of emissions through bound states of O vacancies and implanted N ions as shown in the figure 1.

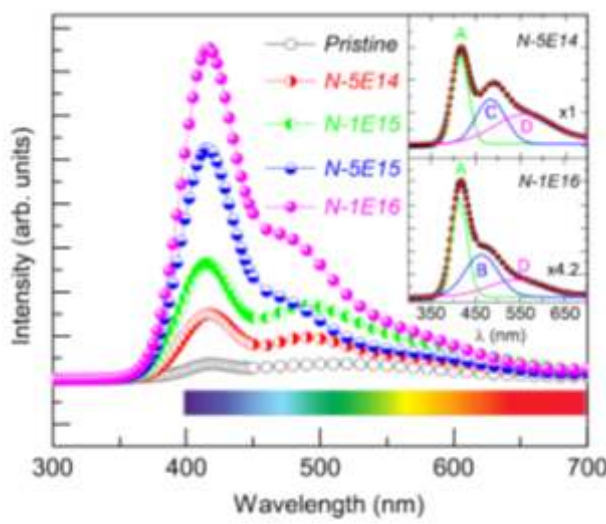


Fig 1 PL spectra of STO films including N ion implanted films with different fluences viz.  $5 \times 10^{14}$ ,  $1 \times 10^{15}$ ,  $5 \times 10^{15}$ , and  $1 \times 10^{16}$  ions/cm<sup>2</sup>.

Another set of STO films were deposited on cleaned quartz substrates using the Radio Frequency (RF) magnetron sputtering technique. The thickness of the films was determined to be ~750 nm. These pristine films were irradiated at IUAC, New Delhi, India with 125 MeV silver (Ag<sup>+9</sup>) beam at different ion fluences of  $1 \times 10^{11}$ ,  $1 \times 10^{12}$ , and  $5 \times 10^{12}$  ions/cm<sup>2</sup>. The structural studies were carried out using the synchrotron Glancing Incidence X-Ray Diffractometer (GIXRD) at the MCX beamline at Elettra Sincrotrone Trieste, Italy. The diffraction measurements were performed using 13 keV energy of the X-ray source. The surface morphology of the films was examined using a Field Emission Scanning Electron Microscope (FESEM - Zeiss GeminiSEM 500)

operated at 30 kV. The UV-visible absorbance spectra were recorded using a UV-Visible spectrophotometer (SHIMADZU UV-2600). The X-ray Absorption Near-Edge Structure (XANES) Spectra at Ti *K*-edge were recorded in fluorescence mode at the TLS-17C1 Wiggler beamline at National Synchrotron Radiation Research Center (NSRRC), Hsinchu, Taiwan. Engineering the optical bandgap of metal oxides is essential for optoelectronic and photocatalytic applications. This study reports the application of electronic excitations, induced by 125 MeV Ag ions, in tuning the bandgap of SrTiO<sub>3</sub> films in the range of 2.93-3.78 eV and their correlation with the synchrotron-based X-ray diffraction pattern and X-ray absorption spectra (XAS). The pre-edge spectral features in the XAS at Ti *K*-edge show significant variation in the valence state implying the role of electronic excitations in modifying the local electronic structures mainly the distortion in the TiO<sub>6</sub> octahedra. This study gives an insight about the role of structural properties and electronic structures in bandgap tuning [2].

#### REFERENCES:

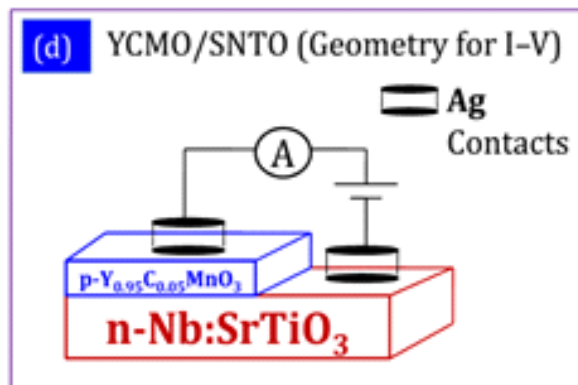
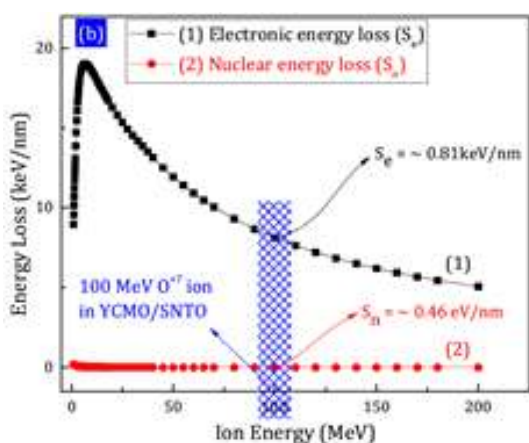
- [1] V. Kumar, et al Origin of intense blue-green emission in SrTiO<sub>3</sub> thin films with implanted nitrogen ions: An investigation by synchrotron-based experimental techniques, Phys. Rev. B. 103 (2021) 024104. doi:10.1103/PhysRevB.103.024104.
- [2] V. Kumar et al., Bandgap engineering in SrTiO<sub>3</sub> thin films by electronic excitations: A synchrotron-based spectroscopic study, Scr. Mater. 195 (2021) 113725. doi:10.1016/j.scriptamat.2021.113725

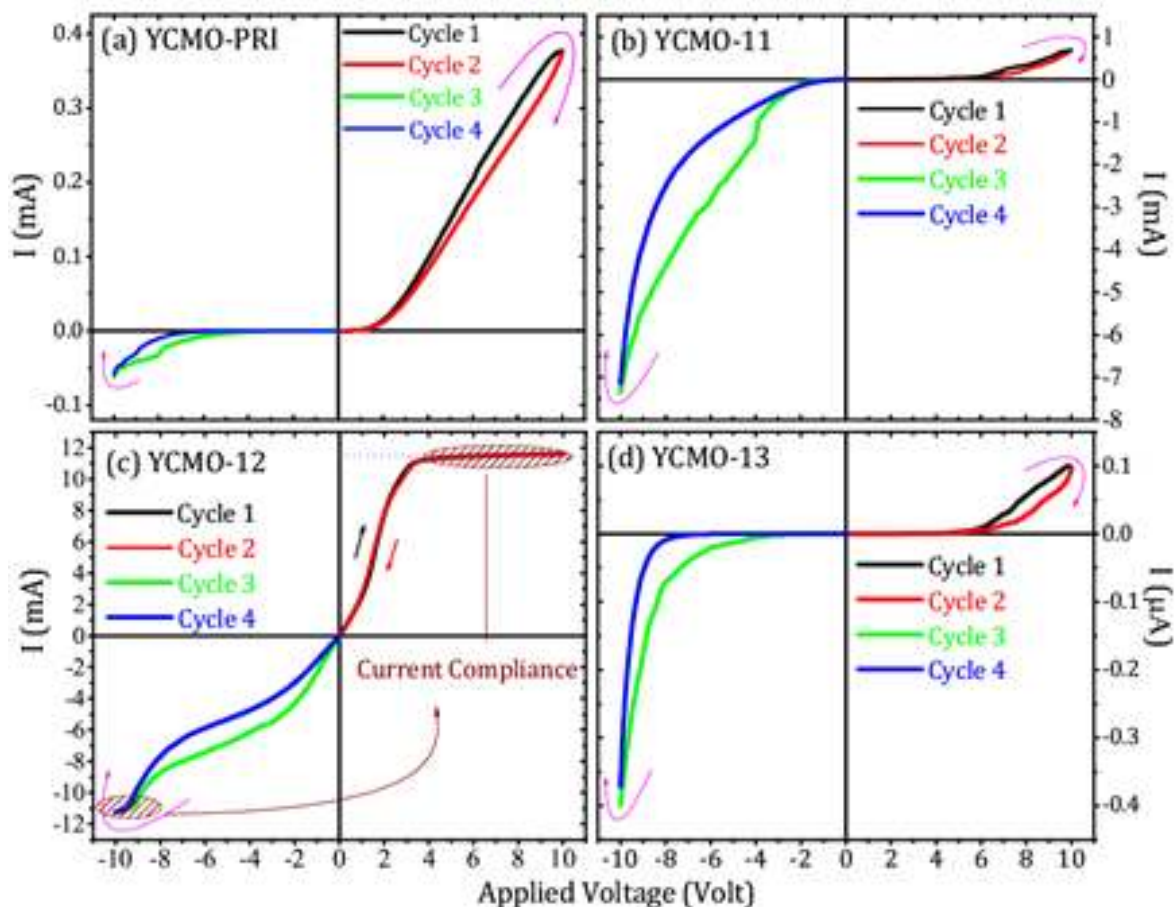
#### 5.2.19 Swift Heavy Ion (SHI) Irradiation Studies on doped YMnO<sub>3</sub> Thin Film Device

Keval Gadani, P.S. Solanki and N.A. Shah

*Department of Physics, Saurashtra University, Rajkot – 360 005 Gujarat, India*

In this research work, the YCMO / SNT0 films of 100nm were irradiated at different ion fluence and studied for their structural, strain state, morphological aspects and the hysteretic I–V measurements for their RS behavior. The XRD and  $\phi$ -scan measurements show the single crystalline nature of all the films with the parallel crystalline orientations of the films with the crystallographic orientations of the (100) substrate. Modifications in the XRD patterns as well as the intensity and the FWHM of the  $\phi$ -scan peaks suggest the modifications in the crystalline nature of the films due to SHI irradiation. The structure gets deteriorated with increase in ion fluence up to  $1 \times 10^{12}$  ions/cm<sup>2</sup> while higher  $1 \times 10^{13}$  ions/cm<sup>2</sup> fluence can improve the structure of the YCMO–13 film. AFM images depict that an average grain size gets suppressed upon irradiation up to the fluence of  $1 \times 10^{12}$  ions/cm<sup>2</sup> while for higher fluence, the film possesses enhanced grain size with suppressed grain boundary density. RS studies show that all the films exhibit distinct hysteretic I–V behaviors which have been discussed in the context of structure – property correlations. Role of strain state at the interface and granular structure of the surface of the films has been discussed in detail to understand the RS behavior of the films. The backward diodes like behavior and absence of leakage current in particular YCMO / SNT0 films have also been investigated in detail. Various theoretical models and mechanisms have been employed to understand the charge conduction across the YCMO / SNT0 interfaces and few models have been identified as valid sources of observed charge conduction across the interfaces of YCMO / SNT0 films. Variations in the fitting parameters have been correlated with the RS device characteristics for their practical spintronic applications. Better reliability, reproducibility and device stability have been confirmed from the endurance and retention behaviors for all pristine and irradiated YCMO / SNT0 thin film devices.





### 5.2.20 Electrical transport study and band gap estimation of Ge implanted CoSb<sub>3</sub> Skutterudite thin films

Anha Masarrat<sup>1,2</sup>, Anuradha Bhogra<sup>1</sup>, R C Meena<sup>1</sup>, A Niazi<sup>2</sup>, Asokan Kandasami<sup>1</sup>.

<sup>1</sup>Inter-University Accelerator Centre, Aruna Asaf Ali Marg, New Delhi 110067, India

<sup>2</sup>Department of Physics, Jamia Millia Islamia, New Delhi 110025, India

CoSb<sub>3</sub> has attracted researches in the field of thermoelectrics owing to its modest thermoelectric properties and low electrical resistivity. CoSb<sub>3</sub> is a low band gap skutterudite compound semiconductor with high carrier mobility. It has a cubic structure. Of all the eight sub cubes in a cubic unit cell, two cubes are voids that can accommodate guest atoms that rattle inside. Various elements can be doped in place of Co or Sb for material modification and to enhance its thermoelectric properties. In the present study, we have utilised ion implantation method to dope Ge in the CoSb<sub>3</sub> lattice. During ion implantation, doping can be done in a controlled way and which enhances the electrical conductivity by increasing the carrier. By ion implantation the void can be filled or can occupy the Co or Sb sites which can act as electron donor or acceptor leading to *p*- and *n*-type semiconductor.

CoSb<sub>3</sub> thin films were deposited on quartz substrate using Pulsed laser deposition (PLD) system from M/S Excel Instruments, Mumbai. The films were then implanted with 100 keV Ge ions using the IUAC (New Delhi) facility for Negative Ion Implantation with the ion fluences:  $5 \times 10^{14}$ ,  $1 \times 10^{15}$  and  $5 \times 10^{15}$  ions/cm<sup>2</sup>. The pristine sample is referred as GCS1 while the implanted films with ion fluences  $5 \times 10^{14}$  ions/cm<sup>2</sup>,  $1 \times 10^{15}$  ions/cm<sup>2</sup> and  $5 \times 10^{15}$  ions/cm<sup>2</sup> as GCS2, GCS3 and GCS4 respectively. The phase of the deposited thin films was determined using the grazing incidence X-Ray Diffraction (GIXRD) of the Philips X'pert PRO (Model PW 3040) diffractometer. The temperature-dependent electrical resistivity ( $\rho$ ) in the range of 80 to 400 K was measured by the four-probe method.

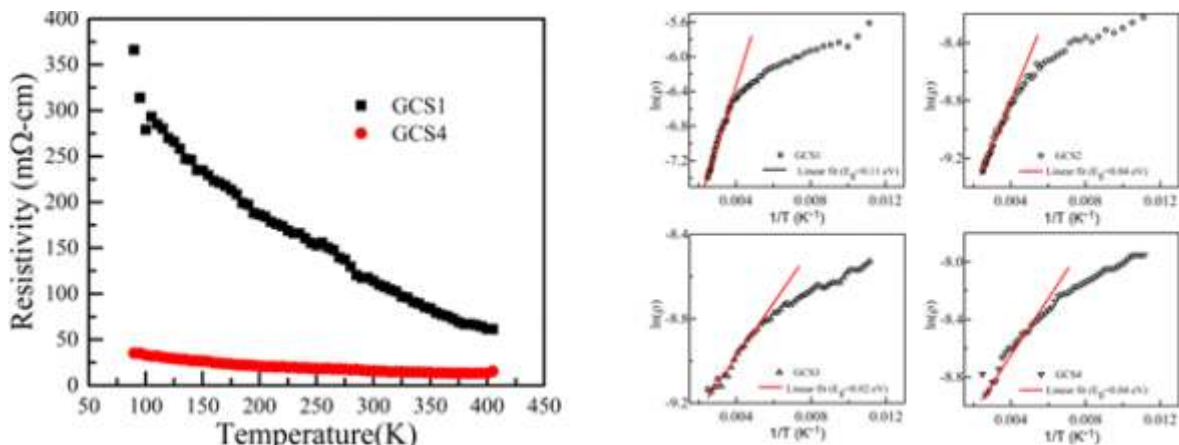


Fig. (a) Temperature dependent resistivity for GCS1 and GCS4. (b). The plot of  $\ln \rho$  vs  $1/T$  fitted using Arrhenius equation for the estimation of bandgap for GCS1, GCS2, GCS3 and GCS4.

The GIXRD data revealed the presence of  $\text{CoSb}_2$  and  $\text{Sb}_2\text{O}_3$  mixed phases along with the  $\text{CoSb}_3$  phase. Electrical resistivity measurement was done for the temperature range of 80 K to 400 K for GCS1, GCS2, GCS3 and GCS4 samples. Fig 1 shows the variation of resistivity for GCS1 and GCS4. The resistivity decreased considerably after Ge implantation because of the considerable increase in charge carrier concentration with increasing ion fluence. We have calculated the band gap of all the films using Arrhenius equation.

$$\rho(T) = \rho_0 \exp \left[ \left( \frac{E_g}{2k_B T} \right) \right]$$

where  $\rho_0$  is constant,  $k_B$  is Boltzmann constant,  $T$  is the absolute temperature and  $E_g$  is bandgap. The straight line fitting of  $\ln \rho$  vs  $1/T$  gives the magnitude of bandgap (Fig 1). The bandgap for GCS1, and GCS4 are 0.11, and 0.04 eV respectively. The bandgap value of implanted samples is lower than that of pristine one. It is due to the fact Ge ion introduces donor level in the bandgap of skutterudite and modifies the band structure.

#### REFERENCES:

<sup>1</sup> J.O. Sofo and G.D. Mahan, Phys. Rev. B **58**, 15620 (1998).

<sup>2</sup> A. Masarrat, A. Bhogra, R. Meena, M. Bala, R. Singh, V. Barwal, C.L. Dong, C.L. Chen, T. Som, A. Kumar, A. Niazi, and K. Asokan, RSC Adv. **9**, 36113 (2019).

## 5.3 RADIATION BIOLOGY

### 5.3.1 Cellular response to high LET radiation exposure in human embryonic kidney (HEK293 T) cells with reference to mitochondria

Sweta Sanguri, AsitikanthaSarma

*Radiation Biology, Inter-University Accelerator Center, New Delhi, Delhi -110067*

Mitochondria may exist in the cell as several individual oval shaped tubules or as a single large, interconnected, membrane bound network, depending on the cell type and the environmental conditions [1][2]. It will be crucial to understand how alteration in mitochondrial structure and function affects cellular function, especially in cells exposed to high LET radiation. Human embryonic kidney cells stably expressing Su9-EGFP were exposed to increasing dose of high LET radiation, and alteration in morphology of the mitochondrial network was studied using fluorescence microscopy and mean fluorescence intensity of GFP protein was measured using ImageJ software for Mac OS X. Results are expressed as mean fluorescence (fold changes) with respect to control  $\pm$ SD. Differences were designated significant at values \*  $p < 0.001$

The energy of carbon ion beam from the Pelletron Accelerator was 85 MeV (equivalent to 7.08 MeV/nucleon). The energy of the beam on the cell surface was 62 MeV (equivalent 5.16 MeV/nucleon). The irradiation dose range used was from 0 to 4 Gy.

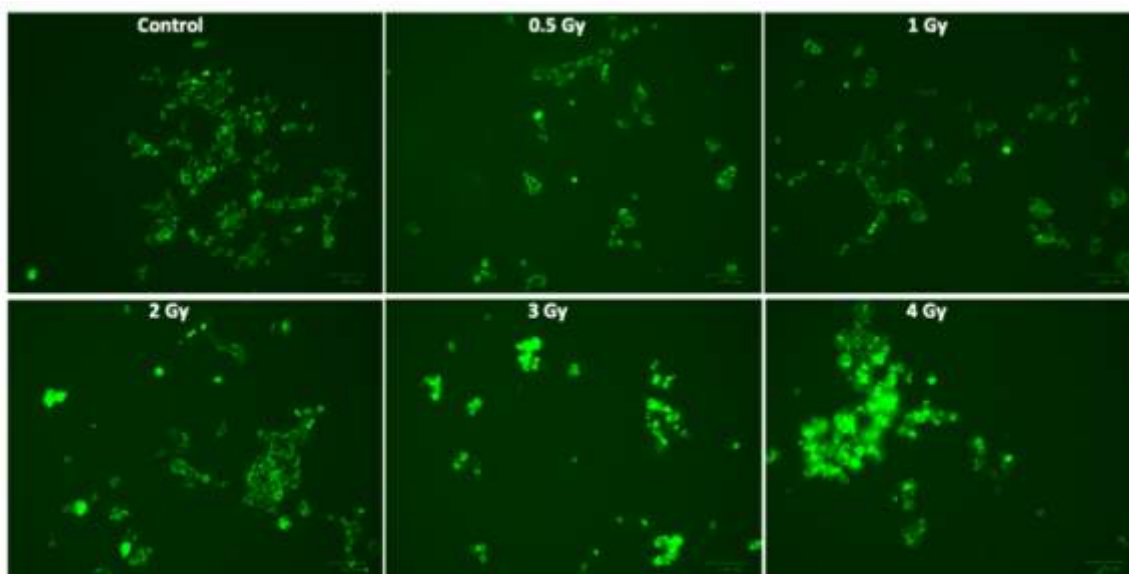


**Figure 1 (a) Reporter cells:** Representative images of HEK 293 T cells expressing Su9-EGFP protein 12 hours post exposure to  $^{12}\text{C}$  beam. Image acquisition was done using ZOE™ Fluorescent Cell Imager (BioRad, USA). Scale bar equals 100  $\mu\text{m}$  (b) Changes in mean fluorescence intensity of HEK 293 T cells expressing Su9-EGFP protein 12 hours post exposure to  $^{12}\text{C}$  beam. Image acquisition was done using ZOE™ Fluorescent Cell Imager (BioRad, USA). Data was analysed using Image J software for mac. Results are expressed as mean fluorescence (fold changes) with respect to control  $\pm$  SD. Differences were designated significant at values \*  $p < 0.001$

Su9 is an important subunit of complex V of electron transport chain [ETC] inside mitochondria. Results demonstrate increase in expression of Su9-GFP expression (as an indirect measure of ETC function) as shown in Figures 1. Significant increase in fluorescence intensity of GFP was observed in dose dependent manner with almost 4.2-fold increase in the highest selected dose 4 Gy with respect to control (*Figure 1b*). Mitochondrial ETC generates potential gradient across the inner mitochondrial membrane along with generation of ATP, a vital energy currency via oxidative phosphorylation process. ETC function increases with the increase in energy demand of the cells. Increase in expression of subunit 9 of ETC complex V reveal increase in ETC function in the cells post radiation exposure, possibly to cope up with the increasing energy demand of the cells to maintain homeostasis after the insult. The images also show change in overall morphology of cells and distribution of mitochondria inside the cells.

Expectedly, alteration in cell morphology increases with increasing radiation dose. Mitochondrial distribution is relatively uniform in control cells and in cells exposed to 0.5 Gy radiation, however the distribution pattern changes in cells exposed radiation in dose dependent manner, with asymmetrical distribution of mitochondria inside the cells (*Figure 1a*). Time kinetics study of the expression of Su9 protein in these cells is currently in progress. Changes in mitochondrial mass, shape size, number and distribution is also being studied and the results will be communicated elsewhere.

1. Chan, D.C., Fusion and fission: interlinked processes critical for mitochondrial health. *Annu Rev Genet*, 2012. 46: p. 265-87.
2. Van der Blik, A.M., M.M. Sedensky, and P.G. Morgan, Cell Biology of the Mitochondrion. *Genetics*, 2017. 207(3): p. 843-871.
3. Farmer, T., N. Naslavsky, and S. Caplan, Tying trafficking to fusion and fission at the mighty mitochondria. *Traffic*, 2018. 19(8): p. 569-577.

### 5.3.2 Studies on effect of chloroquine, LiCl and NH<sub>4</sub>Cl induced autophagy in different cell type

Mitu.Lal, Asitikantha Sarma

*Radiation Biology Laboratory, Inter University Accelerator Centre, New Delhi, 110067*

In mammalian cells the knowledge of the mechanism and the underlying regulation of macroautophagy is currently under investigation. Here, we investigate the role of autophagy in three different types of cells. The well-characterized autophagy inhibitors we have used here, chloroquine, ammonium chloride and Lithium chloride. In this study, we investigated the relative efficacies of CQ and LiCl and NH<sub>4</sub>Cl in cultured human cells HepG<sub>2</sub> [Liver cancer cell], INT407 [Intestine normal cell] and HCT116 [Intestinal cancer cell].

HepG<sub>2</sub> cells were treated with autophagy/lysosome inhibitors. chloroquine (CQ, 1-400 μM), and ammonium chloride (NH<sub>4</sub>Cl, 1-400 mM), and LiCl (1-400mM) for 24 hr. From the result, we observe that:

1. Ammonium chloride can be used for HepG<sub>2</sub> cell line as a positive control as confirmed by MTT assay. It can be used in combination with Radiation as autophagy inhibitor for autophagy studies.
2. Lithium Chloride can be used as autophagy blocker since cells are viable at (1-50mM) at high concentration as confirmed by MTT assay. It can be used in combination with Radiation as an autophagy blocker for autophagy studies.
3. Chloroquine can be used as autophagy inhibitor cell viability decreases (1-400 μM) in dose dependent manner as confirmed by MTT assay. It can be used in combination with Radiation as a autophagy blocker for autophagy studies

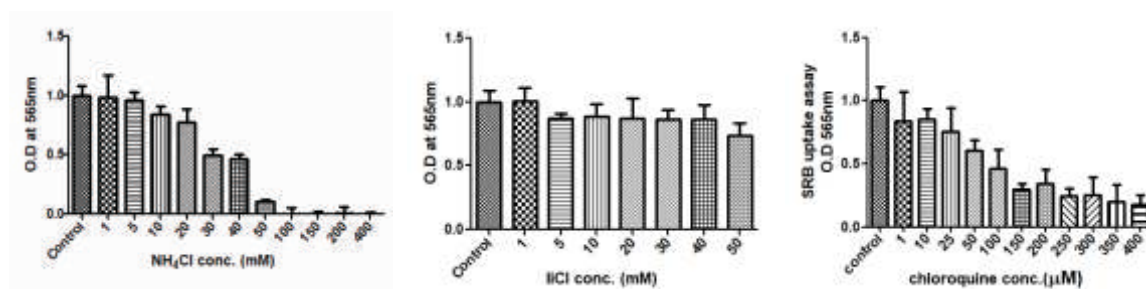


Figure 1. SRB uptake assay [Cytotoxicity study] for cell proliferation in HepG<sub>2</sub> cell line against chloroquine, NH<sub>4</sub>C and LiCl.

HCT116 and INT407 cells were treated similarly with chloroquine (CQ, 1-400 μM). From the result, we observe that Chloroquine cannot be used for both the cell lines since it is toxic and hence cannot be used for radiation study as a positive control.

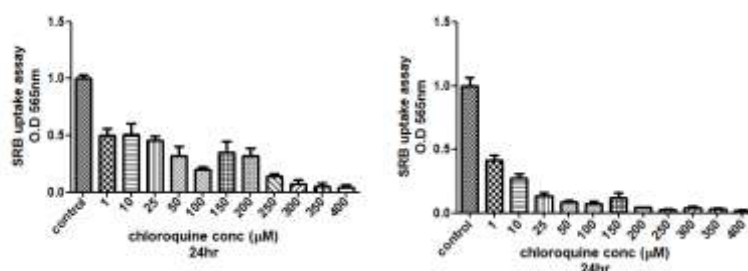


Fig 2. SRB uptake assay [Cytotoxicity study] for cell proliferation in HCT116 and INT407 cell lines against chloroquine.

Further investigations with these cell lines along with above treatments in combination with <sup>12</sup>C beam.

## 5.4 ACCELERATOR MASS SPECTROMETRY AND GEOCHRONOLOGY

### 5.4.1 Role of human environment interaction in tracing the urbanization in different sectors of Ganga Plain: A geochemical and metagenomics approach.

Anupam Sharma<sup>1</sup>, Harsh Kumar<sup>1</sup>, Sandhya Misra<sup>1</sup> and Rajveer Sharma<sup>2</sup>

Birbal Sahni Institute of Palaeosciences, 53 University Road, Lucknow- 226020.

Inter University Accelerator Centre (IUAC), New Delhi-110087

Report: In order to understand the palaeoclimate and palaeovegetation changes and to understand the Anthropogenic impacts in urban areas sediments cores were raised from central Ganga plains viz., Mahabrahman ka purwa pond, Raebareli, U.P., Narahaiya Taal, Bhatpurwa, Raibareli, U.P. Motijheel, Banaras, U.P., Mamapur Village Barabanki, U.P., Bhayara Village, Barabanki, U.P., Jamalpur, Allahabad- Lucknow Highway. In order to attain our objectives multi-proxy including biotic and biotic proxies has been generated and is still under progress. In order to assign the time bracket to the major vegetation and climatic shifts and to demarcate the time zone of increased human intervention in the study region five sediment samples were dated at IUAC, New Delhi covering a time span from 122 years to 7000 years BP.

Preliminary analysis of pollen data from Bhayara (36cm) shows a mix of arboreal and non-arboreal pollens- Chenopodiaceae, Amaranthaceae, Cucurbitaceae, Brassicaceae, Fabaceae, Meliaceae, Asteraceae, Anacardiaceae, Poaceae etc with few non pollen palynomorphs under two broad phases of vegetation and climatic shifts. While from Mampur site, on the basis of lithological variation the 55cm deep core shows three litho units. Palynological investigation shows a mix of arboreal and non-arboreal pollens with a lot of non-pollen palynomorphs especially zoological remains like egg cyst, eggs, body parts etc are observed towards the upper part of profile the non-arboreal dominated along with the algal and fungal spores indicating towards a gradual shift in vegetation and climate of the region.

In Bhayara core the  $\delta^{13}\text{C}$  values show increasing pattern from 180 to 130 cal yrs BP. At 130 cal yrs BP values of  $\delta^{13}\text{C}$  shifted towards more negative. The decrease in values of  $\delta^{13}\text{C}$  clearly indicates the shift towards the dryer conditions. Overall average values of  $\delta^{13}\text{C}$  indicate the abundance of C3 plants in the area.

Trace and major element geochemistry and other proxy study is under progress from these two cores.

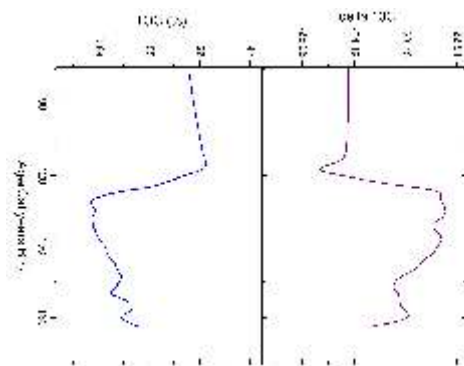


Fig. 1: Trend of Total organic carbon and  $\delta^{13}\text{C}$  with respect to age (cal years BP).

### 5.4.2 AMS radiocarbon dating of core sediment samples from Rann of Kachchh, Gujarat, western India

Fulmati Ram<sup>1</sup>, Anindya Sarkar<sup>2</sup>

<sup>1</sup>Department of Geology & Geophysics, Indian Institute of Technology, Kharagpur-721302, India.

The evolution of Rann of Kachchh through Holocene has always intrigued researchers to dig down its evolutionary history as it may hold clues to the rise and decline of the well-known Harappan Civilization in the Indian Subcontinent. Although the Rann looks apparently monotonous, its landscape is shaped as a combined effect of land, sea and tectonic interactions especially during the Holocene. Decline of such an advanced human settlement has often been alluded to past climate shift. In spite of several geological studies, not much information as yet exists on the spatial and temporal relationship between the continental and marine processes occurring in this region during the Holocene. Contradictory hypothesis exists varying from the Rann being a marine gulf [1] and the decline of the Harappan Civilization occurring due to the withdrawal of the sea [1,2], or

the changing summer monsoon intensities those drove the rise and abandonment of human settlements [3]. The present study attempts to understand the paleo-climatic and paleo-environmental conditions of this region through the Holocene time period.

Four sediment cores were raised from different parts of the Great Rann and Little Rann of Kachchh. Establishing a clear chronology of these cores is essential, since it will allow to anchor the age of the sediments across which the environmental signals and climatic events can be reconstructed through the Holocene. Also, it will provide an idea on the timing of Rann sedimentation. Depending upon the sediment type (mostly clay) and lack of macrophytes or any shell fragments, the sedimentary organic matter (SOM) was primarily chosen for radiocarbon dating.  $^{14}\text{C}$  dating of SOM comes as a challenge because of the range of complex organic molecules present which can have different sources and are also in their different phases of decomposition. The specific ecosystem, its sediment properties, vegetation type and hydrology among other factors controls the age of the sediments. It can contaminate the sediments by either making the age younger or older than its actual age. In such scenarios, often it becomes useful to date the different chemical fractions of the SOM, e.g., bulk, humic and humin fractions, which provides the opportunity to select the fraction yielding a more accurate  $^{14}\text{C}$  date [4,5]. For this study, 14 sediment samples were initially dated following the standard sample pretreatment protocols (Acid-Base-Acid, ABA) of the Graphitization laboratory of Inter University Accelerator Centre (IUAC), New Delhi. 0.5M hydrochloric (HCl) acid and 0.1N sodium hydroxide (NaOH) solution were used for the ABA treatment. The treated samples were then graphitized and  $^{14}\text{C}$  measurements were done using the AMS facility at IUAC. The ABA treatment procedure essentially extracts the humin fractions of organic matter from the sediments for  $^{14}\text{C}$  measurements. Out of the 14 sediment samples dated, only 6 to 7 dates can be used as stratigraphically consistent dates. However, to have better confidence on the age of the sediments, we need to analyze some more samples and if possible, also date different fractions of organic matter like bulk SOM or humic fraction from the same depths where we already have a proper humin date. This will help to have a comparison and select more accurate  $^{14}\text{C}$  dates for all the sediment cores.

The data obtained from the  $^{14}\text{C}$  measurements will be used to establish (1) the chronology and sedimentation rate in the Rann and (2) to study and reconstruct the temporal changes in paleoclimatic and paleoenvironmental conditions by using bulk and compound specific stable carbon isotope ratios. The combined AMS  $^{14}\text{C}$  and carbon isotope data will be used to establish the link or otherwise with the major Indus valley civilization sites of Kachchh.

#### References:

- [1] Gaur, A.S., Vora, K.H., Murali, S.R.M. and Jayakumar, S., 2013. Was the Rann of Kachchh navigable during the Harappan times (Mid-Holocene)? An archaeological perspective. *Current science*, pp.1485-1491.
- [2] Tyagi, A.K., Shukla, A.D., Bhushan, R., Thakker, P.S., Thakkar, M.G. and Juyal, N., 2012. Mid-Holocene sedimentation and landscape evolution in the western Great Rann of Kachchh, India. *Geomorphology*, 151, pp.89-98.
- [3] Ngangom, M., Bhandari, S., Thakkar, M.G., Shukla, A.D. and Juyal, N., 2017. Mid-Holocene extreme hydrological events in the eastern Great Rann of Kachchh, western India. *Quaternary International*, 443, pp.188-199.
- [4] Tonnejck, F.H., van der Plicht, J., Jansen, B., Verstraten, J.M. and Hooghiemstra, H., 2006. Radiocarbon dating of soil organic matter fractions in Andosols in northern Ecuador. *Radiocarbon*, 48(3), pp.337-353.
- [5] Ferro Vázquez, M.C., Kaal, J., Santos, F.J. and Criado-Boado, F., 2019. Molecular fingerprinting of  $^{14}\text{C}$  dated soil organic matter fractions from archaeological settings in NW Spain. *Radiocarbon* 61(1), 101-130

### 5.4.3 Response of Harappan coastal sites in Gujarat to Middle-Late Holocene palaeo-environmental changes: A multiple proxy approach

Prizomwala Siddharth<sup>\*1</sup>, Das Archana<sup>1</sup>, Vedpathak Chintan<sup>1,2</sup>, Sodhi Aashima<sup>1,2</sup>, Sharma Rajveer<sup>3</sup>, Kumar Pankaj<sup>3</sup> and Chopra Sundeep<sup>3</sup>

<sup>1</sup>Institute of Seismological Research, Gandhinagar, Gujarat- 382007, India.

<sup>2</sup>Research Scholars, Gujarat University, Ahmedabad-380009

<sup>3</sup>Inter-University Accelerator Centre, New Delhi-110067, India

Globally, the Holocene period has witnessed large scale climatic and sea level changes which have affected the humans and finally led to their migration due to collapse of the organized societies. The Indian subcontinent in particular, hosted the mighty Harappan civilization during the 9500 yr BP to 3000 yr BP, which has been speculatively collapsed due to the large-scale environmental change. The Holocene Sea level change was transformed by the combination of factors that bothered the land sea configuration. The unique and multifaceted landscape of Gujarat provided ample opportunity to the early human occupants i.e. Harappans, to flourish along banks of rivers and coastal tracts. The landscape of Gujarat has remnants of several abandoned Mature to Late and post Harappan settlements, the causal factors of which are still debated and remains

intrigued. Although some of the most famous Harappan settlements were along the palaeoshoreline viz., Lothal, Dholavira etc; their abandonment during the later period has not been understood. This implies some interesting question which if answered, may lead to new insights on de-urbanization of the organized Harappan societies, viz., did Middle Holocene sea level fluctuations affect and influence the coastal dwelling Harappan settlements leading to their abandonment? Also, several settlements existed on the banks of the river system, were the river dynamics also one of the major factors for the deurbanization? What was the sea level scenario during the Meghalayan period? Did the climate change during Meghalayan period affect the coastal Harappan communities? For the better understanding of Past sea level changes, palaeoshoreline shifting, river morphodynamics and past climate change ~ a higher resolution study of the evolution of the landscape of Gujarat is essential.

The present work was carried out by Institute of Seismological Research, Gandhinagar, Gujarat in collaboration with Inter-University Accelerator Centre, New Delhi. The aim of the present work was to establish a procedure to obtain reliable dates of different foraminifer samples. The samples have been collected from the Mainland Gujarat regions; Navagam (22°51'0.00"N, 72° 23'0.00"E), Kamatalav (22°19'N, 72°16'E), Lothal and from the periphery of the north of Morbi (23°16'40.3"N 71°26'22.8"E). The collected samples were then selected and the selected samples were further used to; pick the, in-situ planktic foraminifers. The establishment of a clear chronology of these sites is of utmost importance, since it will allow us to procure a clear chronological context. Moreover, accurate dating of these sites will also allow a stronger analysis of the environmental and climatic data available, allowing further reconstruction of the Middle-Late Holocene environments; which is a hot topic of debate as it hosted the mighty Harappan civilization and its links with environmental change.

#### 5.4.4. Appraisal of regional and local groundwater-surface water dynamics and residence time using ages determined by carbon-14 dating in parts of North-Western India

Shashank Shekhar<sup>1</sup>, Aditya Sarkar<sup>2</sup>, Akhilesh Kumar Yadav<sup>1</sup>, Shakir Ali<sup>1</sup>, Pankaj Kumar<sup>3</sup>, Rajveer Sharma<sup>3</sup>

<sup>1</sup>Department of Geology, University of Delhi, Delhi-110007, India.

<sup>2</sup>Department of Geology, Presidency University, West Bengal-700073, India.

<sup>3</sup>Inter-University Accelerator Centre, New Delhi-110067, India.

<b>BTR No:</b>	64122/AMS
<b>Principal Investigator:</b>	Dr. Shashank Shekhar
<b>Beam time:</b>	29/08/2019 to 05/09/2019
<b>Coordinator:</b>	Dr. Pankaj Kumar and Dr. Rajveer Sharma (Scientists)
<b>Status of work:</b>	C-14 date received
<b>Ph D scholars currently working:</b>	Mr. Akhilesh Kumar Yadav (DU Research scholar)

This present work entitled “Appraisal of regional and local groundwater-surface water dynamics and residence time using ages determined by carbon-14 dating in parts of North-Western India” is carried by Department of Geology, University of Delhi with collaboration with IUAC, New Delhi. The actual results in terms of dates have been received and a further report is being prepared.

#### Methodology

##### Field Sampling

Thirty groundwater samples collected during field visits in parts of Northern-Western India from various depths were submitted for carbon-14 dating. We collected groundwater sample from 30 different sites.

#### Laboratory Analysis

##### Graphitization process for groundwater

The samples were subjected to pre-treatment in the IUAC Graphitization laboratory. The groundwater samples were pre-treated by flushing each sample for nearly 10 minutes by inert gas He and Ar. For graphitization, samples were kept in graphitization Unit (Carbonate handling system) for acid wash (H<sub>3</sub>PO<sub>4</sub>, 85-90 Celsius for three hours) for removing the carbonates from the sample and iron powder was added as a catalyst. For this

purpose, in total 21 ml of each sample was required (7 ml in three tubes) (Sharma et al. 2019). The graphite collected during this process for each sample was kept in a cathode tube for AMS dating.

## Results

The actual results in terms of dates have been received and a report is being prepared based on these C-14 dates.

- [1]. Sharma, R., Umapathy, G. R., Kumar, P., Ojha, S., Gargari, S., Joshi, R., & Kanjilal, D. (2019). Ams and upcoming geochronology facility at inter university accelerator centre (IUAC), New Delhi, India. Nuclear Instruments and Methods in Physics Research Section B: Beam Interactions with Materials and Atoms, 438, 124-130.

### 5.4.5 Foraminiferal distribution and paleoclimatic reconstruction from the northeastern Indian Ocean

Sudhira R Bhadra<sup>1</sup>, Rajeev Saraswat<sup>1</sup>

<sup>1</sup>Micropaleontology Laboratory, Geological Oceanography Division, CSIR – National Institute of Oceanography

Monsoon governs the economy and livelihood of India. Despite being so important, the monsoon dynamics has not been understood clearly, yet. The limited instrumental data available isn't enough to paint a clear picture of monsoonal changes in the long term. So a good dataset of high-resolution sufficiently long monsoon record beyond the instrumental data is required to understand monsoon evolution and to delineate relative contribution of natural and anthropogenic forcing. Various archives can be used for paleo monsoon studies. We will use planktic foraminifera census count, oxygen isotopic ratio and elemental ratio for the same. The core samples for the proposed study were collected during the IODP 353 expedition. The samples from site U1448 have been used. The samples have been processed following the standard procedure (Naik et al., 2014). Approximately 10mg of *G. ruber* was picked from selected samples from suitable intervals. These specimens were transferred to 0.6ml centrifuge vials and carried to IUAC for dating using the AMS facility. After obtaining the <sup>14</sup>C dates, calibration was done using the online calibration program Calib. The dates of other in between intervals were calculated by interpolating values in dated sample assuming a constant sedimentation rate between those intervals. The sedimentation rate of the dated section varies from 3 cm/kyr to 16 cm/kyr. The foraminiferal work is currently under progress for the same core. For this, a minimum of 300 specimens of planktic foraminifera is being picked using the stereo-zoom microscope for assemblage study.

## 5.5 ATOMIC AND MOLECULAR PHYSICS

### 5.5.1 Addressing three-body dissociation of molecular ions: Extracting lifetimes and dissociation mechanisms

Jyoti Rajput<sup>1</sup>, Herendra Kumar<sup>1</sup>, Pragma Bhatt<sup>2</sup>, C. P. Safvan<sup>2</sup>

<sup>1</sup>Department of Physics and Astrophysics, University of Delhi, Delhi-110007, India.

<sup>2</sup>Inter-University Accelerator Centre, Aruna Asaf Ali Marg, New Delhi-110067, India.

The formation and decay of multiply charged molecules is an interesting field of study since such species were discovered in inter-stellar and laboratory plasmas, because of their presence and active role in atmospheric chemistry and as a test case for *ab-initio* calculations of molecular properties. Our research group has been actively engaged in experimental investigations of the properties of multiply charged molecules. These molecules are generated in an ion-molecule collision experiment in which a slow highly charged ion interacts with a neutral molecule and strips it of one or more electrons. The resultant multiply charged molecule thus formed may be in a stable, metastable or repulsive state and may break apart into atomic or molecular fragments. Such fragments are generally referred to as recoil ions. To study the kinematics and dynamics of this ion-molecule interaction process, the technique of recoil ion momentum spectroscopy is employed. In this technique, the time-of-flight of all recoil ions is measured in coincidence with an electron emitted during the process which acts as a start trigger. In addition, the use of position sensitive detectors allows for measurement of the position of all recoil fragments. From the measured time-of-flight and position information, the momentum vectors of all fragments are determined. These momentum vectors can then be used to reconstruct the complete dissociation process and to study the kinematic and dynamics involved.

In recent years, our focus has been on the three-body dissociation of simple triatomic molecules. The experiments were conducted at Low Energy Ion Beam Facility (LEIBF) of Inter-University Accelerator Centre, New Delhi. Beams of slow highly charged ions were extracted from an electron cyclotron resonance (ECR) ion source and were made to interact with neutral molecules in an evacuated experimental chamber under single collision conditions. A recoil ion momentum spectrometer available at this facility was used to study the ion-molecule interaction.

We have addressed the three-body dissociation of  $\text{OCS}^{3+}$  into  $(\text{C}^+, \text{O}^+, \text{S}^+)$  with reference to the mechanism involved viz. concerted (one step) or sequential (two step) [1]. Using a newly proposed representation [2], we showed that the low lying excited states of the parent molecular ion are responsible for an active sequential mechanism of breakup. In addition, we determined the branching ratio between the two mechanisms for three body dissociation of  $\text{OCS}^{3+}$

(see figure 1 below).

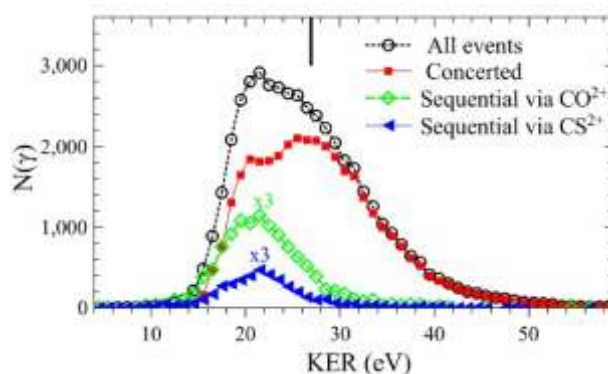
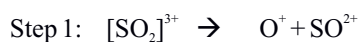


Fig 1: A comparison of kinetic energy release spectra for various modes of dissociation of  $\text{OCS}^{3+}$  leading to the detection of  $(\text{C}^+ + \text{O}^+ + \text{S}^+)$  in triple coincidence [1]. Lines are drawn to guide the eye. The vertical line on top denotes the value obtained using the Coulomb explosion model.

Very recently, we have reported on a new technique for measurement of sub rotational lifetimes of molecular ions [3]. We have looked at the three-body fragmentation of  $[\text{SO}_2]^{3+}$  into  $(\text{O}^+, \text{O}^+, \text{S}^+)$ , separated the events coming from the sequential breakup of this ion via  $\text{SO}^{2+}$  intermediate and measured the sub rotational lifetime of this intermediate molecular ion. The process considered is as follows:



The lifetime of  $\text{SO}^{2+}$  against dissociation is determined to be a fraction of its rotational period and is of the order of few picoseconds. To the best of our knowledge, this is the first report on experimental determination of molecular lifetime of this order. The method that we have proposed is general and is not restricted to triatomic precursors.

### 5.5.2 Investigating inner-shell processes in quasiadiabatic collisions

R Gupta<sup>1,2</sup>, C V Ahmad<sup>1,2</sup>, K Chakraborty<sup>1,2</sup>, A Rani<sup>2</sup>, S Mandal<sup>2</sup>, T Nandi<sup>3</sup>, D Swami<sup>3</sup>, P Barua<sup>3</sup>, D Mitra<sup>4</sup>, G Sharma<sup>5</sup> and P Verma<sup>1\*</sup>

<sup>1</sup>Department of Physics, Kalindi College, University of Delhi, East Patel Nagar, New Delhi 110008.

<sup>2</sup>Department of Physics and Astrophysics, University of Delhi, New Delhi 110007.

<sup>3</sup>Inter University Accelerator Centre, Aruna Asaf Ali Marg, New Delhi 110067.

<sup>4</sup>Department of Physics, University of Kalyani, Kalyani, Nadia, West Bengal 741235.

<sup>5</sup>Department of Physics, Government Engineering College, Ajmer, Rajasthan 305001.

The study of physical phenomena occurring due to strong electronic binding energies, such as observation of charged vacuum, would require synthesis of long-lived superheavy elements which provide possibility of supercritical nuclear charge. Short lived transuranic elements have been synthesized in only picobarn yields by nuclear synthesis methods such as fusion reactions or multi-nucleon transfer processes [1,2]. The heaviest element synthesized till date is  $Z = 118$  by Oganesson and group [3] which is way off the supercritical nuclear charge value. Inevitably, the supercritical nuclei ( $Z > 172$ ) with adequate half-life cannot be produced by nuclear synthesis methods. However, with the aid of scattering experiments performed with high  $Z$  projectile and heavy  $Z$  atoms a supercritical charge can be assembled for a short period of time if the collision is quasi-adiabatic with respect to the orbital motion of electrons [4,5].

Quasiadiabaticity implies a slow-moving incoming ion causing weak perturbation of target electron wave functions. During the course of interaction, the inner shell electrons of the target continuously adjust themselves to the varying two-center nuclear potential of the collision partners leading to a transiently formed collision molecule, with slowly varying inter nuclear distance  $R$ , for the inner-shells. The electron configuration of such a transient collision molecule approaches asymptotically that of a united atomic (UA) system with an effective atomic number  $Z_{\text{UA}} = Z_1 + Z_2$ , thus introducing the concept of intermediate superheavy molecules or superheavy quasimolecules [6]. This forms the foundation of the Molecular Orbital (MO) theory of ion-atom collisions, in which it is assumed that the inner shells of the collision partners form diatomic molecular orbitals around both nuclei. If the collision process is quasiadiabatic, i.e., nearly symmetric systems colliding at slow ion velocities leading to formation of a quasimolecule, then electrons can be promoted from target inner shells to projectile or vice-versa at localized regions of inter nuclear distance where two molecular levels overlap or become nearly degenerate in energy [7,8]. For systems with large asymmetrical attribute, direct ionization remains dominant during collision.

Investigation of inner-shell ionization of superheavy systems with  $120 \leq Z_{\text{UA}} \leq 130$  were performed at IUAC. The experiment was carried out in the Atomic Physics beamline in beam hall II. The systems with  $120 \leq Z_{\text{UA}} \leq 130$  were achieved via adiabatic collisions of  $0.65\text{--}1.2$  MeV/u  $\text{Ag}^{q+}$  ( $5 \leq q \leq 9$ ) with thin films of  $73 \leq Z_2 \leq 83$  of various thicknesses. The collision-induced inner shell processes were studied by measuring the X-rays from both collision partners using KETEK SDD detector. Normalization was performed with scattered particles detected by two Passivated Implanted Planar Silicon (PIPS) detectors acquired from Canberra. Several interesting phenomena have been observed, such as X-ray energy shifts (see Figure 1). The increase in the energy shift with increase in the energy of the projectiles and the altered intensity ratios cause multiple ionization of the targets leading to the formation of higher number of spectator vacancies [9]. A surprisingly high emission of target X-rays indicated a vacancy creation process in addition to the direct coulomb ionisation of the target [10]. The inner shell couplings and vacancy transfer mechanisms can be studied using correlation diagrams [11].

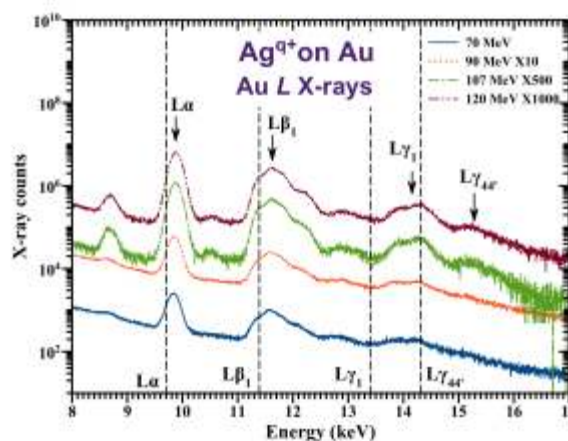


Figure 1. X-ray energy shifts in Bi. The dashed lines represent the standard X-ray energies [12].

## References

- [1] W Greiner et al, *Nucl. Phys. A* 834, 323c (2010)
- [2] V Zagrebaev et al, *Phys. Rev. C* 78, 034610 (2008).
- [3] P Karol et al, *Pure Appl. Chem* 88, 155 (2016).
- [4] J Reinhardt et al, *Rep. Prog. Phys.* 40, 219 (1977).
- [5] J Reinhardt et al, *Z. Phys. A* 303, 3, 173 (1981).
- [6] J Rafelski et al, *Phys. Rev. Lett.* 27, 958 (1971).
- [7] R Anholt, *Rev. Mod. Phys.* 57, 995 (1985).
- [8] P H Mokler et al, (1984) X-Rays from Superheavy Collision Systems. In: H J Beyer, H Kleinpoppen (eds) Progress in Atomic Spectroscopy Part C. Physics of Atoms and Molecules, vol 18. Springer, Boston, MA.
- [9] P Verma et al, *Phys. Scripta* 61, 335 (2000); *J. Phys.: Conf. Ser.* 875, 092029 (2017).
- [10] P Verma et al, *NIM B* 245, 56 (2006); *Rad. Phys. Chem.* 75, 2014 (2006).
- [11] W Lichten, *J. Phys. Chem.* 84, 2102 (1980).
- [12] J A Bearden *Rev. Mod. Phys.* 39, 78 (1967).

### 5.5.3 Formation of quasi-molecules in slow heavy ion-heavy atom collisions

C V Ahmad<sup>1,2</sup>, R Gupta<sup>1,2</sup>, K Chakraborty<sup>1,2</sup>, D Swami<sup>3</sup> and P Verma<sup>1</sup>

<sup>1</sup>Department of Physics, Kalindi College, East Patel Nagar, University of Delhi, New Delhi-110008.

<sup>2</sup>Department of Physics and Astrophysics, University of Delhi, New Delhi-110007.

<sup>3</sup>Inter University Accelerator Centre, Aruna Asaf Ali Marg, New Delhi-110067.

Investigations on the probability of formation of superheavy quasi-molecules during the collision of low energy heavy ions with heavy atoms have been performed using emitted X-rays as a signature. Heavy, highly charged ions because of their high potential and strong coulomb field result in an enhancement of X-Ray production cross sections upon collision with heavy atoms [1,2]. In addition, the probability of formation of a quasi-molecule increases if the target-projectile combination satisfies the adiabatic condition ( $Z_p / Z_T \approx 1$  and  $v_p/v_T \ll 1$ ); here P denotes projectile and T the target) [3].

The 75<sup>0</sup> beam line of Low energy Ion beam facility (LEIBF) with its 10 GHz ion source was used to bombard low energy projectiles viz. 2-5 MeV Xe<sup>q+</sup> ( $10 \leq q \leq 14$ ) and 2-4 MeV Kr<sup>q+</sup> ( $10 \leq q \leq 14$ ) on targets with atomic number varying between  $67 \leq Z_T \leq 83$  and  $47 \leq Z_T \leq 83$  respectively. Different target thicknesses in the range of 90-508  $\mu\text{g}/\text{cm}^2$  were used. These targets were mounted at the center of the vacuum chamber on a target ladder rotated at 45° with respect to the forward beam direction. Specific target projectile combinations as well as projectile energies were chosen to ensure adiabatic collision conditions. The emitted X-rays were recorded by two silicon drift X-ray detectors (KETEK AXAS-A) mounted at 45° and 90° with respect to the incoming beam. The efficiency of these detectors was measured via bombarding thin film targets of Al and Ni by 350 keV H<sup>+</sup> ion. The ion beam current was monitored by two Faraday cups: one, with a collimator of 3mm, placed at the beam-in port of the chamber before the target ladder and the other placed behind the target ladder i.e. at the beam-out port of the chamber. Both the Faraday cups were equipped with electron suppressors to suppress the secondary electrons.

Observation of Molecular Orbital X-Rays (MO) are a definite signature of formation of quasi-molecules. In order to enhance the probability of observation of MO X-Rays, possible noise producing elements such as beamline noise, imperfect grounding issues, electronic noise, pump-related vibrations, stray light, etc. were individually detected and eliminated prior to the experiment. We report the observation of MO X-Rays for such heavy collision systems (the case of 4 MeV Xe<sup>12+</sup> on Au shown in Figure 1 here) at low ion energies (<0.05 MeV/u). The authenticity of the observed MO was verified by keeping a 20  $\mu\text{g}/\text{cm}^2$  Al absorber in front of the detector to suppress the target M X-Rays. Detailed analysis of all the collision systems studied is in progress.

## References:

- [1] M. Czarnota et al 2009, *Phys. Rev. A* 79, 3, 032710 (1–14).
- [2] Verma, P., et al. 2017. *J. Phys. Conf. Ser.* 875(10), 092029, 2011 *Phys. Scr.*, T144, 014032.

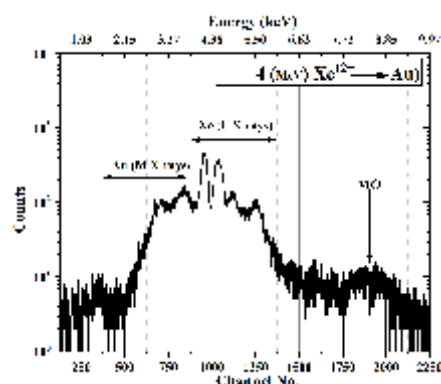


Figure 1. X-Ray spectrum recorded with Al ( $20 \mu\text{g}/\text{cm}^2$ ) absorber in front of detector for 4 MeV Xe<sup>12+</sup> bombarded on Au.